LBL-3351
c.2

STUDIES OF THE DISSOCIATION FRAGMENTS OF N_2 AND THE g_J MEASUREMENT OF METASTABLE $^5S_2$ ATOMIC OXYGEN

Tuncay Incesu
(Ph. D. thesis)

October 1974

Prepared for the U. S. Atomic Energy Commission
under Contract W-7405-ENG-48

TWO-WEEK LOAN COPY

This is a Library Circulating Copy which may be borrowed for two weeks. For a personal retention copy, call Tech. Info. Division, Ext. 5545

LAWRENCE BERKELEY LABORATORY
UNIVERSITY OF CALIFORNIA

LBL-3351
c.2

DISCLAIMER

This document was prepared as an account of work sponsored by the United States Government. While this document is believed to contain correct information, neither the United States Government nor any agency thereof, nor the Regents of the University of California, nor any of their employees, makes any warranty, express or implied, or assumes any legal responsibility for the accuracy, completeness, or usefulness of any information, apparatus, product, or process disclosed, or represents that its use would not infringe privately owned rights. Reference herein to any specific commercial product, process, or service by its trade name, trademark, manufacturer, or otherwise, does not necessarily constitute or imply its endorsement, recommendation, or favoring by the United States Government or any agency thereof, or the Regents of the University of California. The views and opinions of authors expressed herein do not necessarily state or reflect those of the United States Government or any agency thereof or the Regents of the University of California.

LBL 3351

STUDIES OF THE DISSOCIATION FRAGMENTS OF N_2 AND THE g_J MEASUREMENT OF METASTABLE $^5S_2$ ATOMIC OXYGEN

Tuncay İncesu

(Ph. D. thesis)

October 1974

Prepared for the U.S. Atomic Energy Commission
under Contract W-7405-ENG-48

ABSTRACT

The first study described here was intended to produce, identify and investigate the magnetic properties of a recently reported $^6S_{5/2}$ metastable state of atomic nitrogen. However, we were unable to demonstrate its existence among the constituents which we could detect in the beam of the discharge products of the nitrogen molecule.

In the second study, the atomic beam magnetic resonance method was used to compare the g_J factor of $^5S_2$ state in atomic oxygen with the g_J of 2 $^3S_1$ state of helium at H = 4228 and 3209 gauss. The metastable oxygen and helium atoms were produced in a pulsed discharge source. After traversing the beam apparatus these atoms were detected by the Auger process. Helium and oxygen resonances were accumulated successively. By collecting the data only in a certain interval of the time-of-flight distribution, we isolated the ^5S and ^3S states from other discharge products. With 158 pairs of resonances taken at four relative hairpin and field orientations, the final result is

$$g_J = -2.0020910(10).$$

ACKNOWLEDGMENT

My graduate studies started with joining in a newly forming small group with the goal of building an atomic beam apparatus and thus establishing a research laboratory in the Middle East Technical University, Ankara. Such an objective could be achieved only through technical and financial support. The generous offers from the Atomic Beam Group of Berkeley provided the first, and the Ford Foundation the latter. Then, I spent one year in Berkeley learning the atomic beam research technique.

In following years, parts of the beam apparatus in Ankara were machined by the skillful group of technicians in the METU Physics Department. Although the work presented in this report does not cover the research done during my first visit to Berkeley, nor the construction and test work in Ankara, I do want to take this opportunity to express my gratitude to those who contributed both to my work and knowledge. The assistant technician Faik Pekyılmaz, technicians Ali İhsan Küçükekşi and İsmail Doğru, chief technician Hasan Ataizi of METU deserve my appreciation. I give my thanks to my co-workers Atilla Özmen, Ateş Tezer and Erol Aygün who were very eager, cooperative and persistant in our efforts during the assembly and the test phases of the atomic beam apparatus in Ankara. Professor

Adnan Şaplakoğlu, the former supervisor of the group in Ankara, had not only dealt with related scientific and technical problems, he has overcome the difficulties in machining and constructing a precision apparatus with limited facilities. I am also indebted to him for introducing me to the subject and guiding me toward the scientific research.

I want to thank Dr. Paul Vanden Bout and Professor Vernon J. Ehlers who patiently accompanied and lead me through the first research I did in Berkeley. Professor William A. Nierenberg, the then leader of the Berkeley Atomic Beam Group and Assistant Secretary General for Scientific Affairs, NATO, arranged the Ford Foundation grant. His great authority and kindness made my first visit to Berkeley and accomplishments possible. I am grateful to him.

The works which are reported here were done during my second visit to Berkeley. I enjoyed the hospitality of the Atomic Beam Group, the Department of Physics, the University of California and the Lawrence Berkeley Laboratory. I wish to express my thanks to Pat Yarnold who was so helpful in providing the necessary items and services during the experiments. Draftsman Warren Harnden and illustrators Bob Stevens, Mrs. Evelyn Grant did an excellent job in drawing the figures. My thanks go to all of them and the people in the Graphic Arts and Technical Information Divisions of Lawrence Berkeley Laboratory for photographing the drawings and printing this report.

I appreciate the design suggestions of Douglas MacDonald, the

technical coordinator of the Berkeley Atomic Beam Group.
I owe many thanks to Miss Carol Putman who has planned the page and table formats artistically and performed an extraordinary typing and proofreading work on this thesis.

Dr. Michael Prior has been very concerned, helpful and a source of information during both my first and second stays in Berkeley. His illuminating discussions which clarified many questions in my mind are greatly appreciated.

I would like to thank Professor Cengiz Yalçın, my Ph.D. supervisor and the Chairman of the Physics Department, METU, for his encouragement through the hard decisions and support for obtaining the scholarship which made this work possible.

It is a pleasure to acknowledge the constant cooperation, help and friendship of Dr. Ahsanul Huq. His experience and fine spirit have been a major benefit for me from the beginning of the experiments to the completion of this thesis.

Most of all, I present my deepest gratitudes to Professor Howard A. Shugart, who has been far beyond the research advisor for me. His always stimulating interest, invaluable guidance, continuous aid and great kindness have influenced both my work and my beliefs. Without his personal and professional concern and support, I could not even think of doing the present and the previous research. I am also thankful to him for his precious help and important advice for developing and improving the atomic beam laboratory at METU.

My appreciation is due my wife Güllü and my baby daughter Billur for their nice companionship.

The grant from UNESCO, and the financial support of Lawrence Berkeley Laboratory are gratefully acknowledged.

This work was performed under the auspices of the United States Atomic Energy Commission.

TABLE OF CONTENTS

	Page
ABSTRACT	iv
ACKNOWLEDGMENT	v
INTRODUCTION	1
I. STERN-GERLACH TIME-OF-FLIGHT STUDY OF DISSOCIATION FRAGMENTS OF NITROGEN	
A. Theory	7
Dissociation and Predissociation	7
States of Atomic Nitrogen	11
Quenching Effects	16
B. Apparatus	18
C. Experiment	26
D. Results and Discussions	36
II. g_J FACTOR OF $3p^3 3s\ ^5S_2$ METASTABLE STATE ATOMIC OXYGEN	
A. Theory	48
Multipole Moments of an Atom	48
a) Electrostatic Interactions	49
b) Magnetic Interactions	53
Atom in the External Magnetic Field	59
a) Interaction of $\vec{L}$ with the Magnetic Field	60
b) Interaction of $\vec{S}$ with the Magnetic Field	63

Page

c) Interaction of $\vec{I}$ with the Magnetic Field . . . 63

d) Total Interaction of an Atom with the Magnetic Field 64

Theory Pertinent to the Experiment 71

B. Apparatus and Experiment 74

Gas Feed System 74

Source 75

Detector and Geometry 79

Metastable States of Atomic Oxygen and Helium . . . 85

Data Collection System 90

Field Locking and Homogenizing 95

Radio Frequency System 102

Experiment 106

C. Data, Analysis and Results 116

Data Handling 116

Analysis 120

Errors 122

Results 125

Conclusions 127

APPENDICES

A. Time-of-Flight Spectrum Data of the Dissociation Fragments of Nitrogen 131

B. Computer Program to Search Atomic Magnetic Moments 132

Page

C. The Flow Diagram of the Program LFIT 133

D. The Program AVERAGE 134

REFERENCES 135

INTRODUCTION

Being the most abundant gases in the earth's crust and atmosphere and essential constituents of life, oxygen and nitrogen have been the subject of extensive studies since the early days of science. Aristotle defined the physical elements of nature as fire, water, air and earth. After the discovery of oxygen by Priestley in 1774, a list of 33 elements, including oxygen and nitrogen as well as lime and magnesia, was published by Lavoisier. Later, lime was separated into oxygen and calcium; and magnesia was found to be composed of oxygen and magnesium. In the following decades, the physical and chemical properties of nitrogen and oxygen have been continuously investigated by scientists.

In 1865, M. A. Morren[1] reported the nitrogen afterglow. Since the glowing gas was found to be chemically active, it was called "active nitrogen." The literature on active nitrogen which has been published after 1945 is reviewed by Wright and Winkler[2] and the work of Mitra[3] provides a survey of the experimental developments prior to 1945. The luminescent and active behavior of nitrogen may be attributed chiefly to the presence of ground state atoms and excited molecules. However, it is believed that excited nitrogen atoms and nitrogen molecules with higher energy content may be responsible for the

short-duration afterglows. Among these atomic species, Innes and Oldenburg[4] postulated the existance of the ^6S state in the "auroral" afterglow. This sextet state of the nitrogen atoms was considered metastable with an energy of 13 ev above the ground state. Although an evidence of possible existence in the laboratory by electron bombardment of nitrogen was reported,[5] it has not been detected experimentally until the lifetime measurement of Fairchild, Garg and Johnson.[6] Using the time-of-flight technique, they obtained 100 ± 25 usec for the natural lifetime of this species; and, combining their lifetime measurement with their quenching results, they concluded that nitrogen atoms are in the $2s(2p)^3 3s\ ^6S_{5/2}$ metastable autoionizing state. The motivation of the studies presented in the first chapter of this thesis was to identify this species in the Atomic Beam Machine and to explore the state further by using Stern-Gerlach and magnetic resonance techniques. Here we present a summary of the theory of dissociation and dissociation fragments, the features of the apparatus and the experiment. Then we discuss our results and indicate some open questions.

The second chapter concerns itself with the precision measurement of the g_J factor of atomic oxygen in its $^5S_2$ metastable state. This measurement was inspired by the fact that a certain signal had appeared due to a minute oxygen contamination during some stages of the previous nitrogen experiment. Atomic oxygen has two metastable S states, i.e., $2p^4(^1S)$ and $2p^3 3s(^5S)$.[7] The g_J factor of the ^1S state is zero. The first measurement of the g_J factor of ^5S state of oxygen

was published by Kiess and Shortley.[8] They used Zeeman patterns of red and infrared lines of oxygen to derive the g_J factor. Their result is $g_J(^5S_2) = 1.999 \pm 0.002$.

In 1967 Brink observed the $^5S_2$ state of oxygen in a molecular beam apparatus and reported a low precision g_J factor measurement. Besides using the mass spectrometer in the detector he provided further evidence for the presence of ^5S state by observing 3947 Å and 7774 Å atomic oxygen lines in the optical spectrum of the discharge. These lines are due to the electronic transitions terminating in ^5S state. By comparing the resonance frequencies of ^5S and ^3P states he concluded $g_J(^5S) = 1.97 \pm 0.05$ [9] for atomic oxygen in the quintet state. Although the lifetime of this state has been measured and calculated[10] carefully, we could not trace any publication which either confirms and improves the precision of the g_J results. It seems that our measurement with a final result of $g_J(O, {}^5S_2) = -2.002\,091\,0(10)$ establishes good grounds for a theoretical calculation of high precision.

The experimental method used in our measurement is called the Molecular Beam Magnetic Resonance Technique. In the literature, Molecular Beam implies both atomic and molecular rays of particles. The first beam of atoms was made by Dunoyer.[11] He heated Na in one end of an evacuated glass tube and neutral atoms travelled through slits, practically without colliding with each other, and formed a thin layer of Na on the surface of the other end of the tube. Between 1920 and 1933, Stern, Gerlach, Knauer and their associates tested the Kinetic Theory of Gases, spatial quantization, wave hypothesis and

Dirac's Theory by means of molecular beams. Their work is described in detail by Fraser in his book.[12] The next great advance was made by Rabi and his collaborators. They introduced the Molecular Beam Resonance Technique[13] in 1938. Their apparatus consisted of a source called the oven, two inhomogeneous deflecting magnets which were already used by Stern, a homogeneous magnet in which a radio-frequency transition took place, and finally a detector. These are the main parts of a modern molecular beam apparatus. The whole system is in a low pressure vacuum envelope. Molecules emerging from the source are collimated into the inhomogeneous magnetic field of A magnet. The mean free path of the molecules in the apparatus is usually much longer than the length of the apparatus. Therefore, molecules travel in straight lines unless they experience a force. The A magnet, due to its particular design, has a large field gradient. Under the force $\vec{F} = -\vec{\nabla}(-\vec{\mu} \cdot \vec{B})$ the molecules are deflected depending upon their velocity and moment. $\vec{\mu}$ is the magnetic moment of the molecule. In some literature, the A magnet is referred to as the "polarizer." The molecules, deflected by the A magnet then enter into the region of the homogeneous field of C magnet. Here they experience no force, but see a time varying electromagnetic field of the rf loop, the so-called hairpin, in addition to the constant homogeneous field. At this point, they are also collimated further. The B magnet has the same features as A magnet. The magnitude, direction and orientation of the gradient of this field can be adjusted so that if a transition occurs (i.e., a change in the direction of $\vec{\mu}$ takes place) in the oscillating

field of the hairpin, the beam is either deflected into or deflected from the detector. Thus the resonance provides either a maximum (flop-in) or a minimum (flop-out) in the beam intensity. The B magnet is called the "analyzing magnet" or "analyser." Although we make use of the well known principles of molecular beams, the actual geometry used in our experiment is quite particular and explained in detail later in Chapter II.

By observing a resonance at a certain constant homogeneous magnetic field and by measuring the exact resonance frequency of the time varying magnetic field, one is able to study the energy difference between the states connected by that transition. By repeating the experiment at various C field magnitudes, one can obtain the field dependence of the transition frequency, the Zeeman effect, and the energy structure of the states under consideration.

The second chapter of this thesis is separated into three parts. Part A contains an outline of the theory of fine structure, hyperfine structure, and the interaction of atoms with the magnetic field. We then discuss the theory directly related to the experiment. Part B is devoted to the features of the apparatus and experiment. In this part, the gas feed system, discharge source, geometry, detector and related electronics are explained in detail. Then we summarize the information on the metastable states of oxygen and helium. Our data collection system is worth a mention since it enabled us to select certain species and reduce background. This technique was used for the first time in this experiment. The remainder of part B gives the details of the

field locking and homoginizing by shimming, of the radio-frequency system, and of the procedure of the experiment.

Part C deals with the final steps towards the results (i.e., data handling and evaluation, least square fitting of the resonance curves to the Lorenzian line, results, histograms of results and, at last, concluding remarks on the results).

Appendices are added for the sake of completeness. In the flow diagram of the LFIT program, Appendix C, the outlines of the subroutines are contained. Appendix D is the program AVERAGE which was used to obtain the final g_J results.

I. STERN-GERLACH TIME-OF-FLIGHT STUDY OF DISSOCIATION FRAGMENTS OF NITROGEN

A. Theory

Dissociation and Predissociation. The dissociation energy D_0^0 of a diatomic molecule is defined as the work required to dissociate the molecule from the lowest vibrational level of the ground state into the constituent "atoms."[14] If ΔG is the energy difference between the successive vibrational levels of the molecule, dissociation energy can be written as

$$D_0^0 = \sum_v \Delta G_v \qquad \text{(I. 1)}$$

where v is the number of vibrational levels. If one plots the ΔG of the appropriate absorption band of the molecule, versus v, the area under the curve represents the dissociation energy. (Fig. I. 1 and 2.) Such curves are called "Birge-Sponer" plots.[15] For nitrogen, the molecular spectrum of the vibrational levels can not be followed for $v > 27$. In order to obtain a precise value for D_0^0, v up to about 40 would be desired. However, an extrapolation sometimes may give a sufficiently accurate result.

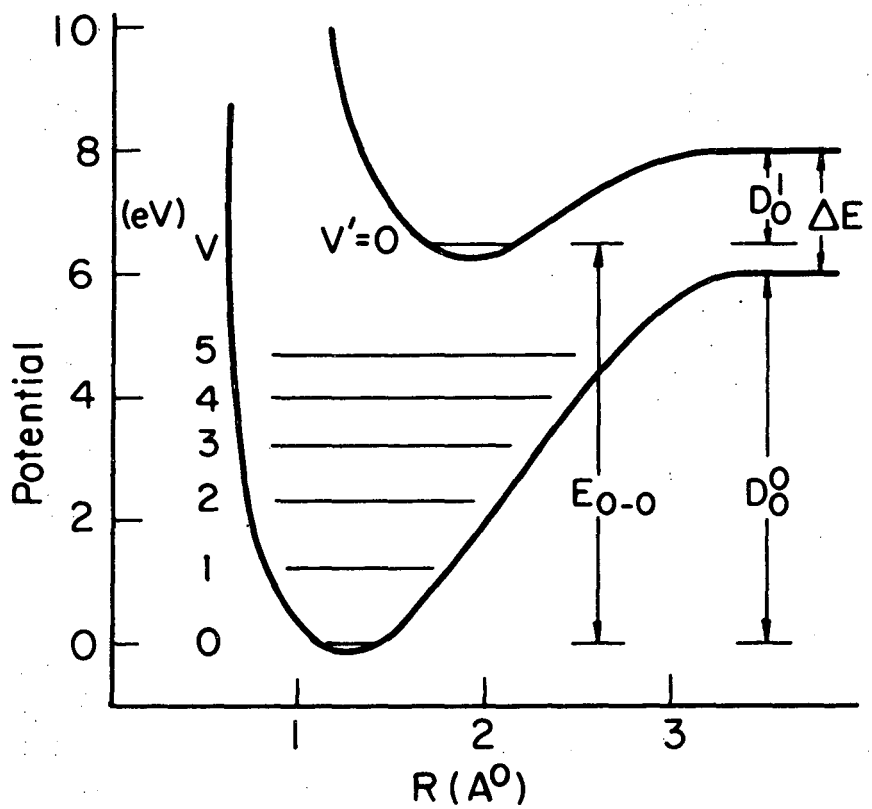

Fig. I. 1. Potential curve for a typical diatomic molecule.

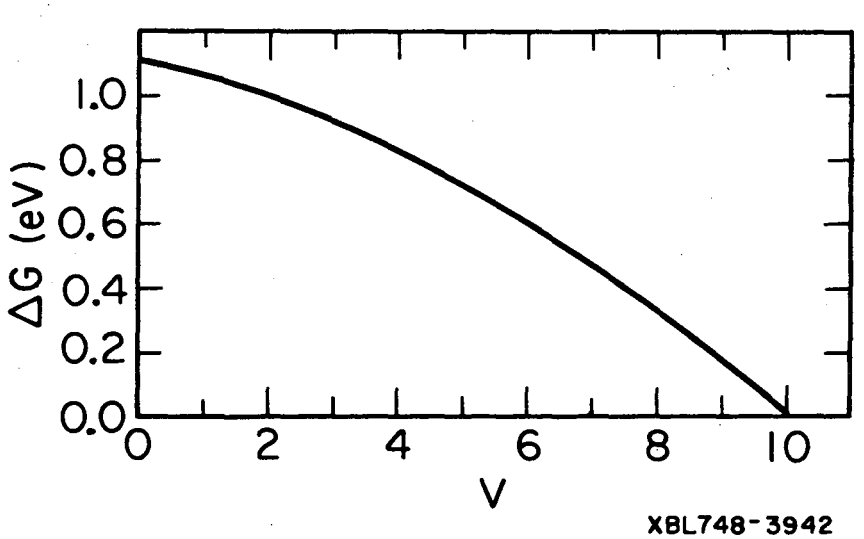

Fig. I. 2. Vibrational intervals versus v. (Birge-Sponer Plot)

Similarly, each of the excited states has a dissociation energy D_o^1 relative to its lowest state. Here the products of the dissociation may also be excited atoms. Therefore, as it is seen from Fig. I. 1, if the atomic energy level differences ΔE of the dissociation products are known, then

$$D_o^o = D_o^1 + E_{o-o} - \Delta E \qquad \text{(I. 2)}$$

where E_{o-o} is the energy differences between the lowest vibrational states.

In case the vibration rotation levels of the two excited electronic states of a molecule have about the same energy, the potential curves of the two states may cross as in Fig. I. 3a. That is, there is a mixing between the wave functions of two states of proper symmetry. This will cause a perturbation on the expected position of the energy levels. But, if one of the states is a repulsive state, a radiationless transition from the discrete state to this continuous state may take place. Since the new state is repulsive, the molecule now dissociates into its fragments. This phenomena is called pre-dissociation. The dissociation energy of nitrogen is accepted as $D_o^o = 9.756(5)$ev although a general agreement on it is still missing.[16]

The excitation of molecules from the ground electronic state with v = o by electron impact may lead also into a bound (see Fig. I. 3b) or a pure repulsive state (see Fig. I. 3c). In the case of a bound state, the molecule dissociates from the repulsive part of the

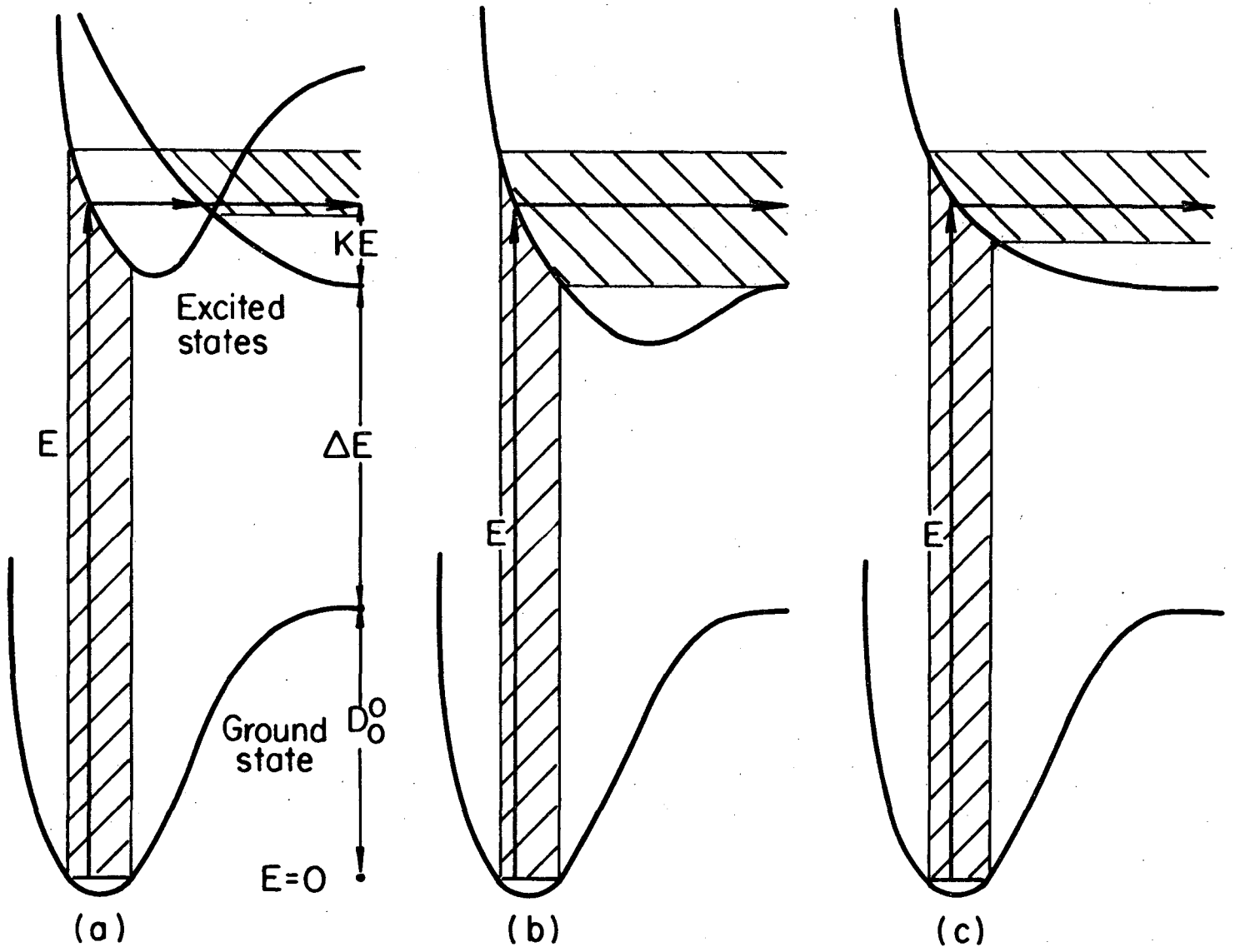

XBL748-3938

Fig. I. 3. Illustration of excitation and a) predissociation, b) dissociation from a bound state, and c) dissociation from a repulsive state of a diatomic molecule.

curve. Then $E - (D_0^\circ + \Delta E)$ gives the kinetic energy of the dissociation fragments, where E is the excitation energy. Therefore, some fragments may have zero kinetic energy. $D_0^\circ + \Delta E$ represents the potential energy of the dissociation fragments. However, it is always greater than zero here. Certainly, after an excitation process, ionization, auto-ionization, and re-radiation are also expected. In this research we are mainly interested in excited or ground state fragments, i.e., neutral atoms. From the conservation of momentum in the center-of-mass system, for the fragments of dissociation having equal mass, we obtain

$$v_1 = v_2 \quad \text{and} \quad E_{k1} = E_{k2} \tag{I. 3}$$

Therefore, a study of the translational velocities of the fragments would lead to information about the shape of the repulsive part of the potential curve provided that the ground state, vibrational wave function is very well known.

States of Atomic Nitrogen.

Among the dissociation fragments $^4S_{3/2}$, ground state atomic nitrogen is the most abundant in a beam produced by an electron impact or a discharge source. The ground electron configuration of atomic nitrogen is $1s^2 2s^2 2p^3$. This configuration gives the three states, ground state and two low-lying metastable states, $^2D_{5/2,\ 3/2}$ and $^2P_{3/2,\ 1/2}$, respectively, 2.4 ev and 3.6 ev above the ground state. ^2D has a long lifetime[17] of 26 hours, while the radiative lifetime of ^2P is only 12 seconds. The concentrations of ^2D and ^2P nitrogen atoms, compared to that of ^4S atoms, are expected to be very low in the

dissociation products.

The short-duration, high-intensity auroral afterglow of nitrogen gives strong emission of $N_2^+(B^2\Sigma_u^+ - X^2\Sigma_g)$ bands.[17] This indicates that highly energetic species must exist during the brief duration afterglow, since about 21.5 ev is required to bring a ground state nitrogen molecule into the excited N_2^+. Neither N atoms nor N_2 molecules have been reported to have energetic enough levels to create N_2^+ bands. Comparing N I spectra with the known O II line spectra, Innes and Oldenburg[4] hypothesized that metastable $(1s^2 2s2p^3 3s)^6S$ nitrogen atoms colliding with normal atoms produce excited N_2^+ molecules.

$$N(^6S) + N(^4S) \rightarrow N_2^+ \text{ exc.} + e^- \qquad \text{(I. 4)}$$

This process provides a total energy of 23 ev which is more than required for the ionization and excitation. The fact that the sextet system is missing in the observation of N I spectrum is explained by very small differences between the ionization energy and its energy level (13 ev). Therefore, intense lines of the system were supposed to lie in the distant infrared. Furthermore, they explained the high energy, short-duration emission of neutral N_2 by the collision.

$$N(^6S) + N_2(^1\Sigma) \rightarrow N(^4S) + N_2(^3\Pi) \qquad \text{(I. 5)}$$

which provides 12.2 ev to excite the N_2 bands. The prediction of the energy of lowest sextet states of N I makes use of the analogy of the

same sextet state of O II relative to its $^2P_{1/2}$ and $^4D_{1/2}$ states. Prag and Clark[18] disagreed with 13 ev because they stated that by changing Z, the various electronic and magnetic interactions might not scale in the same ratios and cause some shifts in the expected value of the energy level of sextet relative to doublets and quartets. By using extrapolation methods, they proposed 17.2 ± 0.2 ev. Since this value is larger than the ionization potential of atomic nitrogen, in the calculation of the lifetime of this state, the probability for auto-ionization and radiative transition must be considered.[19] Prag and Clark proposed alternate excitation reactions to explain the short-duration afterglow. Loosly bound (0.5 ev)N_4 complex, containing an $N(^6S)$ atom, has an internal energy of 17.2 + 9.8 = 27.0 ev. This highly energetic complex, colliding with $N_2(A^3\Sigma_g)$ molecules by exchanging an electron, may create molecular $N_2(C^3\Pi_u)$, $N_2^+(B^2\Sigma_u)$ and atomic $N(3s\ ^2P)$ levels. On the other hand, the same species colliding with $N(^4S)$ atoms may produce $N_2^+(B^2\Sigma_u)$, $N_2(C^3\Pi_u)$ and $N^+(^3P)$ from which the emission was attributed to the electrons which are produced in the proposed reaction, thus depleting the N_4 complex in the medium.

Feldman and Novick[5] observed an excitation threshold of 30 ev, admitting molecular nitrogen and bombarding it by electrons in their apparatus. Allowing 9.8 ev for dissociation, 20 ev is the remaining energy in the c.m. system for allegedly $N(^6S)$ atoms. The next measurement on this state was reported by Fairchild, Garg and Johnson[6] in 1973. They used two detectors along the beam. The first detector was a 60% transparent metallic mesh Auger detector located about

70 cm from the electron gun and the second one was a solid metal plate located about 180 cm from the electron gun. By using the time-of-flight technique, two plots of time of flight versus the number of surviving atoms were obtained from the two detectors. The number of atoms $N_2(t_2)$ detected by the second detector at time t_2 is given as

$$N_2(t_2) = C\, N_1(t_1) e^{-(t_2 - t_1)/\tau} \qquad \text{(I. 6)}$$

$N_1(t_1)$ is the number of species detected by the first detector, C is the constant which depends on the efficiencies of the detector and τ is the lifetime of the species. The above equation can be written in the logarithmic form as

$$\ln(N_2/N_1) = \ln C - (t_2 - t_1)/\tau \qquad \text{(I. 7)}$$

Therefore, the slope of the straight line of $\ln(N_2/N_1)$ versus $(t_2 - t_1)$ gives $- 1/\tau$. Their experimental result was 100 ± 25 μsec. The lifetimes of ^2D and ^2P states are much greater than this value. Since the pressure in their excitation region was relatively high, Rydberg atoms with a lifetime of the order of 1 to 100 μsec were thought to be eliminated before they emerge from the collimating slit into a detection region. On the other hand, species with τ < 1μsec would have very little chance to survive until they reach the first detector. Before continuing the discussion of the $N(^6S)$ atom, we will outline some relevant information about high-Rydberg states.

A high-Rydberg state of an atom or molecule is a state with a large principal quantum number n. Since the average radius of electron orbit is

$$\langle r \rangle = \frac{1}{2Z}[3n^3 - \ell(\ell+1)] \qquad \text{(I. 8)}$$

we expect a large radius for a large n. Then the atom or molecule can be considered to consist of an ion core and a high-Rydberg electron. Similarity between the behaviors of high-Rydberg electron and hydrogen atom electron provides a good understanding of the properties of high-Rydberg states. The ionization energy of hydrogen atoms is given by

$$E = 13.6/n^2 \text{ (ev)} \qquad \text{(I. 9)}$$

For large n, this energy gets extremely small. Therefore, the potential curve of a high-Rydberg molecule differs very slightly from the ion core molecule. This means that dissociation depends on the ion core. After dissociation, the high-Rydberg electron remains bound to ionic dissociation fragment, thus forming a high-Rydberg atom.

The radiative lifetime of a high-Rydberg state with principal quantum number n varies as [20]

$$\tau_{n\ell} \sim n^3 \qquad \text{(I. 10)}$$

for a fixed ℓ. For example, a state with n = 20 would have a

radiative lifetime between 10 and 100 μsec depending on ℓ.

Now we return to the discussion of features of the time-of-flight studies and related theories. We emphasize the theoretical basis of the molecular beam time-of-flight lifetime measurement[6] of the metastable nitrogen atoms for two reasons. First, its conclusion triggered our studies on oxygen. Second, we have employed similar molecular beam time-of-flight methods in conjunction with the Stern-Gerlach technique during our experiment.

Quenching Effects

In terms of electric field quenching, high-Rydberg atoms and metastable atoms have distinct characters. While a Rydberg state remains unaffected by an electric field until a critical point and then quenches completely, the metastable state quenches continuously and linearly with the square of the electric field. If $\gamma_R(E)$ represents the field dependent decay constant of highly excited hydrogen levels, it can be written as

$$\gamma_R(E) \simeq \begin{cases} 0 \text{ when } E < E_c \\ \infty \text{ when } E > E_c \end{cases} \qquad \text{(I. 11)}$$

where E_c is the critical electric field strength. However, the decay constant of ^6S state is given by Johnson[21] approximately as

$$\gamma_s(E) = \gamma_s + (D/L)k_s E^2 \qquad \text{(I. 12)}$$

Here γ_s is the natural decay constant of ^6S state, D is the length of

the quench plates, L is the total length of the flight path and k_s is the constant that represents the mixing of $1s^2 2s\ 2p^3 3s$ and $1s^2 2s 2p^4$ configurations caused by the electric field.

B. Apparatus

The apparatus we have used throughout these studies is the Berkeley Atomic Beam Apparatus (room 86) which has a total length of 2.5 m from the source to the detector. (See Fig. I. 4.) The field gradient of its inhomogeneous magnets is about 10,000 gauss/cm with a field of 10,000 gauss. The A and B magnet poles are 21 inches long. Except during magnetic field quenching tests and the resonance trials, we have not utilized the homogeneous C field. The beam machine is pumped down to $\simeq 5 \times 10^{-7}$ torr by seven diffusion and two mechanical pumps. The collimating slit is 6-10 mils wide and placed in the middle of the C magnet. The source slit varied from 3 to 8 mils and the detector slit from 12 to 25 mils.

A schematic diagram of the gas feed system is shown in Figure I. 5. Noble gases like helium and argon were used for calibration purposes. The flow of the gas was adjusted coarsely by means of two valves on the gas cylinder and finely by the variable leak. Sometimes we cooled the gas either by placing the cooling helix into a liquid nitrogen dewar or filling the source attachment cavity with liquid nitrogen. A mechanical pump, pumped on the system continuously whenever it was not in use. During the flow of gas, the typical pressure on the line was about 100-200 microns of Hg.

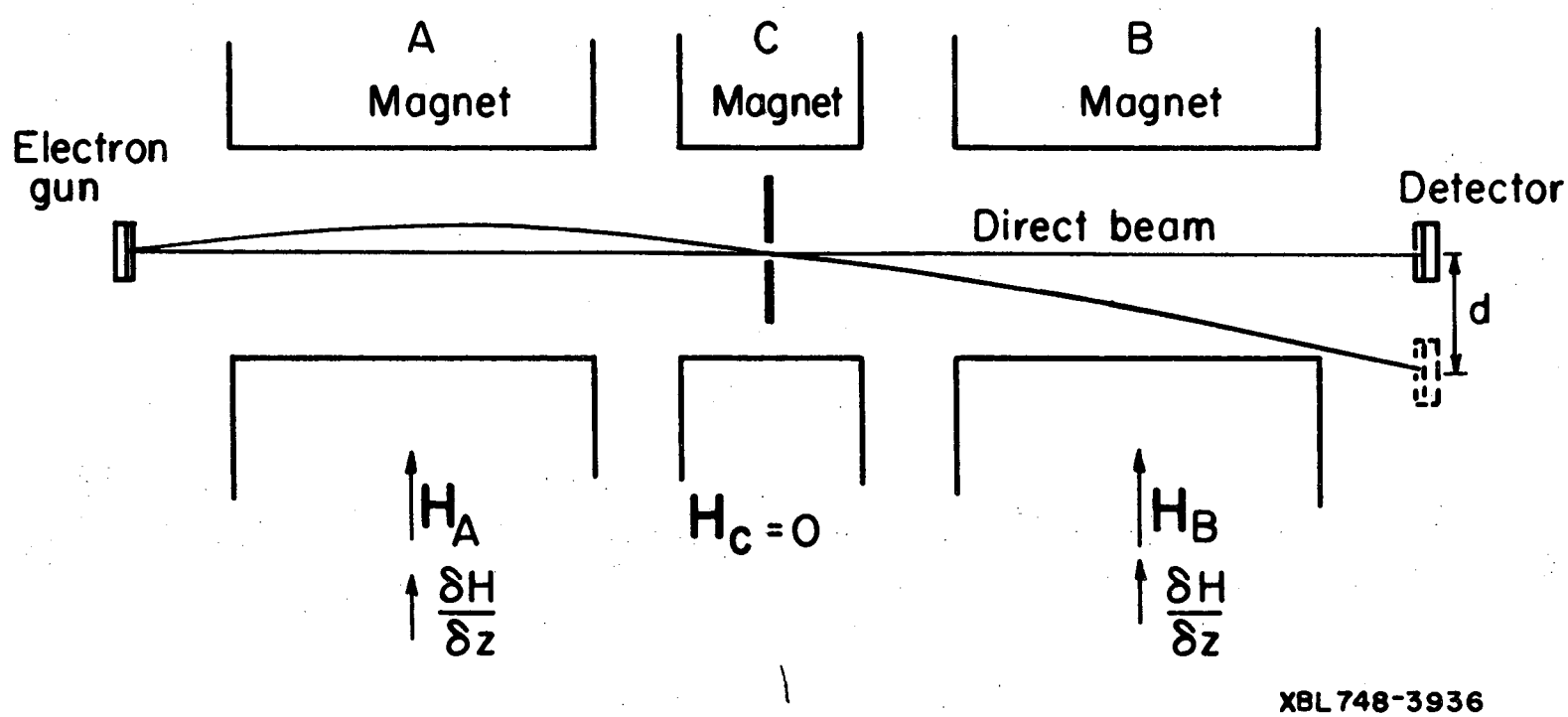

Fig. I. 4. Schematic atomic beam apparatus used as a deflecting time-of-flight analyser.

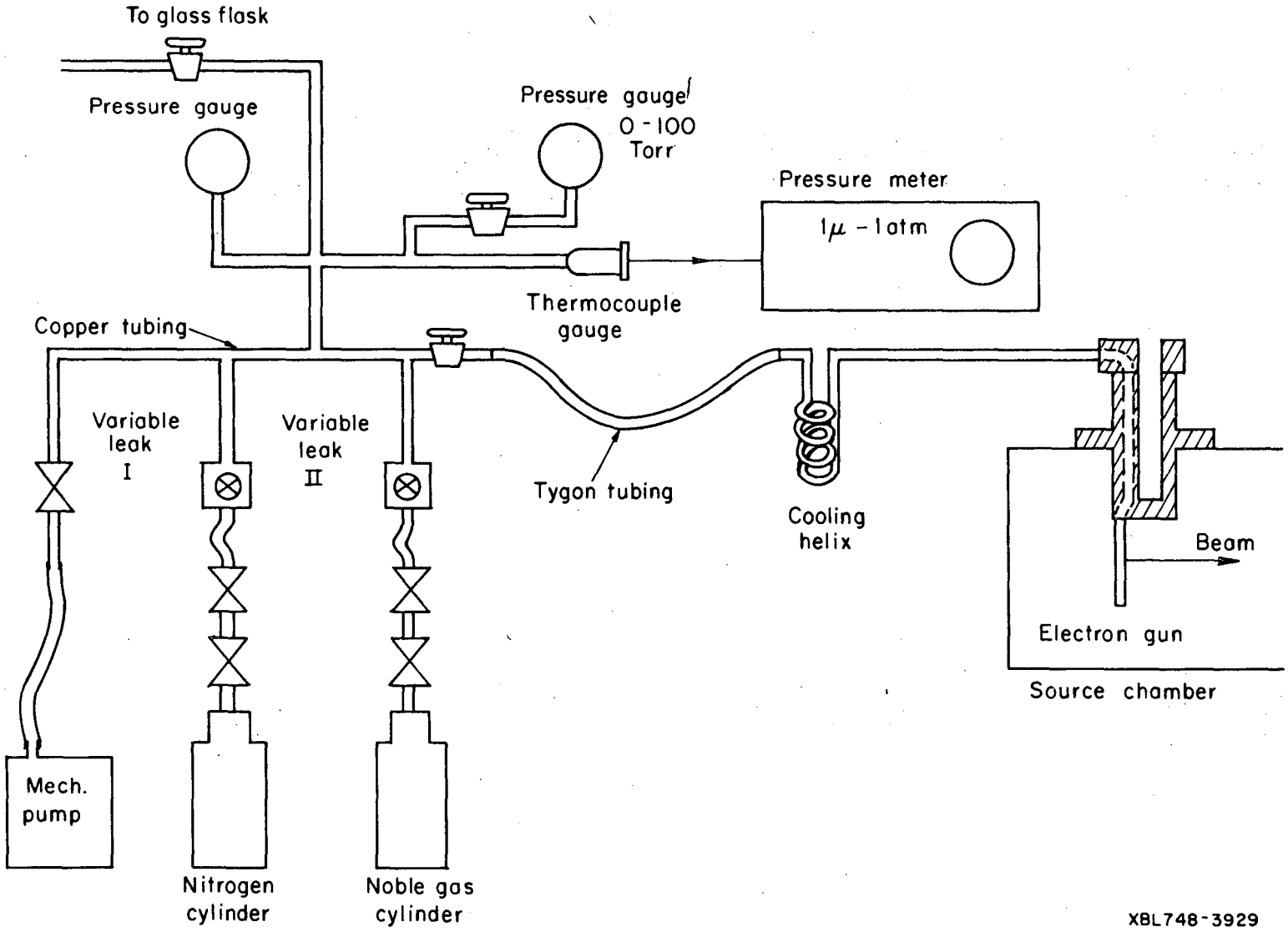

Fig. I. 5. Gas feed system.

The gases in the tank were high-purity grade, supposedly containing less than .0001% oxygen. However, we have built and tried a tungsten filament getter[22] in the hope of removing any remaining oxygen from the nitrogen gas, but this did not improve our results considerably.

Throughout the experiment several types of sources were designed and put into operation. Some surplus sources from the old experiments were also utilized. However, most of the data was taken by using a particular electron gun-type source. It is made of three iron pieces (see Fig. I. 6). The two pieces on the left-hand side hold the tungsten filament in 5 mm deep, 3 mm wide groove and are electrically isolated from each other and from the source attachment arm on which they are mounted by mica spacers. The other piece, on the right-hand side, is the anode. The anode is also separated from the filament holders and attachment arm by mica sheets. Gas is fed through the attachment arm into the filament groove by a small opening between these three pieces. Since these pieces are pushed tightly against each other and there are mica layers between them, we do not expect any leak to the source chamber between the pieces. On top of the main pieces, two slit jaws are attached to form a vertical slit of 6.5 mm height. Being electrically isolated from everything, these slits may be left floating, grounded or at any potential with respect to the anode and filament. The diameter of the tungsten filament was between 4 and 15 mils and, therefore, the filament current varied from 2.5 to 12 amperes. The schematic drawing and the photograph of our electron gun are given in Fig. I. 6 and Fig. I. 7. A disadvantage of this electron gun was

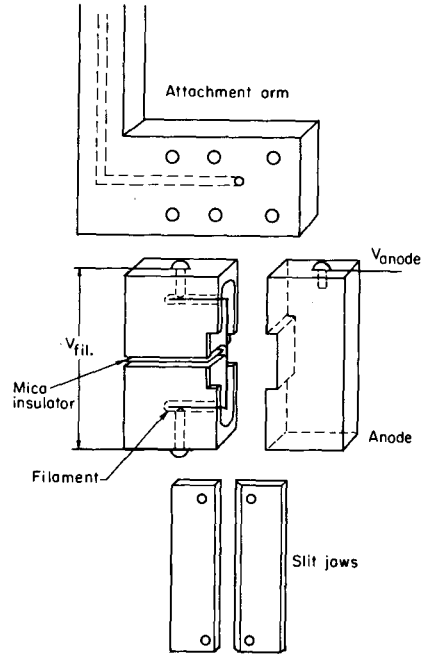

Fig. I. 6. Exploded view of the electron gun. Some mica spacers are not shown for clarity.

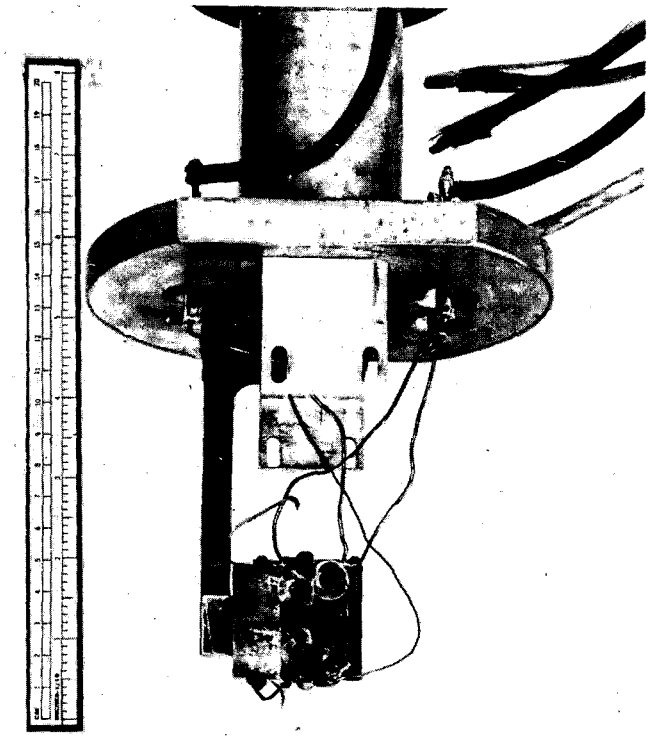

XBB 744-2321A

Fig. I. 7. Source attachment and electron gun.

that the filament lasted only a short time (from 3 to 16 hours of operation, for example.)

Anode voltage was applied in the pulsed mode, each pulse lasting a certain time (such as 13.3 or 40 μseconds) depending upon whether the experimenters wished to study faster or slower species. During this time, electrons which are emitted by the tungsten filament are accelerated toward the anode and bombard the gas molecules, and, dissociate them into different fragments. Maximum anode voltage was about 200 volts. A regular DC power supply output was switched on and off by an electronic switching circuit. This circuit was controlled by a square pulse which also controlled the operation of the data-collecting PDP 11 computer. Immediately after the anode voltage is turned off, data was collected from the detector by the PDP 11 computer in 64 channels, each channel corresponding to, let us say, 13.3 μseconds. The computer then idles in a display mode for about 5.9 milliseconds or, in other words, for about 448 channels until a new pulse turns the anode voltage on and again off. The total time between two successive anode voltage pulses determines the repetition rate. For the above example, it was $2^9 = 512$ channels or 6.75 milliseconds. Fig. I. 8 shows an illustration of the pulsed-mode operation. (A more technical and detailed explanation and block diagram of the data-collection system will be presented in Chapter II.) At the end of each run, the data is printed by means of a teletype printer which is connected to the PDP 11.

This pulsed-mode, data-collection technique thus gives the

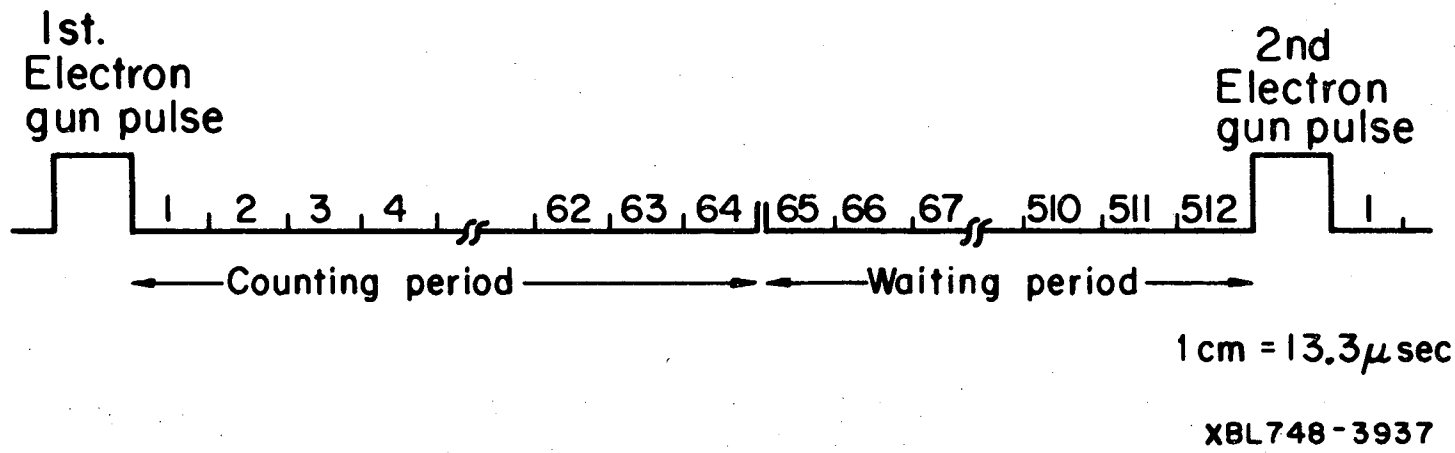

Fig. I. 8. Data collection sequence.

number of particles which are able to reach the detector during their lifetime and sorts them into different channels according to the time the particles spent in traveling from the source to the detector. We therefore obtain a time-of-flight spectrum of the particles. Throughout the experiment two scalers were also in operation. One of them counted the total number of particles in all channels while the other was set to a desired window of channels, counting only those particles which are in the selected interval of channels, i.e., time.

The detector we used was a cold tungsten surface, emitting Auger electrons when struck by energetic metastable atoms. This tungsten surface is followed by a continuous semi-conducting film which serves as a secondary electron emitter and provides the electric field to accelerate them. Electrons are re-directed towards the surface film by the field of a permanent magnet. The windowless, Bendix Magnetic Electron Multipliers (MEM) have a gain of 10^7 and are very stable when exposed to the air. They are not sensitive to visible and long wavelength ultraviolet radiation.

C. Experiment

In researching atomic magnetic moments, the Stern-Gerlach[23] technique has been very effectively used. If some of the dissociation fragments of nitrogen molecules were nitrogen atoms in ^6S metastable state, they could be deflected by inhomogeneous magnetic fields. Therefore, an experiment which combines the time-of-flight and the Stern-Gerlach techniques would give us important information on these species and lead further to more precise measurements.

The deflection of an atom with an effective magnetic moment μ_{eff} and mass M in an inhomogeneous magnetic field is given by

$$d = \frac{1}{2} \frac{\mu_{eff}}{M} \frac{dH}{dz} t^2 \qquad \text{(I. 13)}$$

where t is the time for the atom to traverse the field and $\frac{dH}{dz}$ is the gradient of the field. Using a calibration beam of atoms with known $\mu_{eff.c}$ and M_c, one can measure the unknown magnetic moment of any atom

$$\mu_{eff} = \frac{1}{K_c} M \frac{d}{t^2} \qquad \text{(I. 14)}$$

where $K_c = (d_c/t_c^2) \cdot (M_c/\mu_{eff.c})$. The subscript c stands for calibration. It is apparent that the constant K_c depends also on the

characteristics of the apparatus such as $\frac{dH}{dz}$, geometry and the system of units. However, a plot of deflection versus t_c^2 for the calibration beam would provide us the constant K_c since it can be expressed also as

$$K_c = m_c \times \frac{M_c}{\mu_{eff.c.}} \qquad \text{(I. 15)}$$

where slope, m_c is readily available from the straight lines on the graph.

Although the main scope of the experiment was to identify the ^6S state of atomic nitrogen, meanwhile we studied various parts of the time-of-flight spectrum. Among those parts studied are the so-called fast peaks, high-Rydberg states, molecular excited states, etc. We will mention these studies briefly as we proceed.

Johnson, Fairchild and Garg obtained the time-of-flight spectrum, shown in Fig. I. 9. The distance from the source to the detector was 1.83 meter. According to their conclusions, the peak at 240 μsecond corresponds to the ^6S nitrogen atoms. This information yields a flight time of 327 μsecond for our machine. From quantum mechanics, in a strong magnetic field and omitting the nuclear effects

$$\mu_{eff.} = g_J m_J \mu_B \qquad \text{(I. 16)}$$

where μ_B is the Bohr magneton = 9.27×10^{-27} erg/gauss, m_J is the magnetic quantum number of atom and g_J is the Landé g factor,

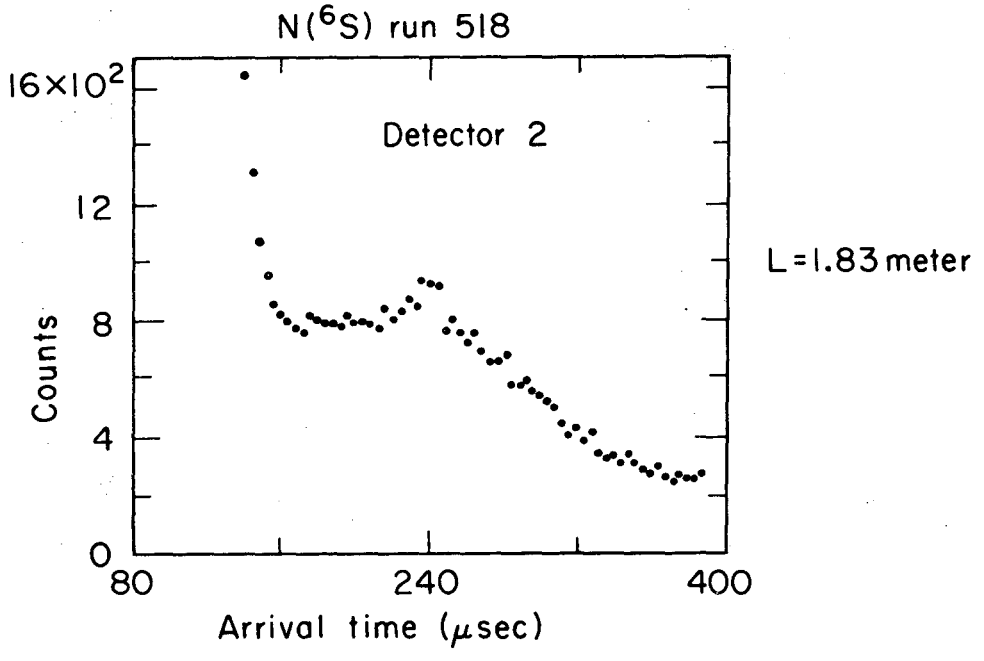

Fig. I. 9. Time-of-flight spectrum of nitrogen fragments at the second detector of a time-of-flight apparatus. (Johnson, Garg and Fairchild)

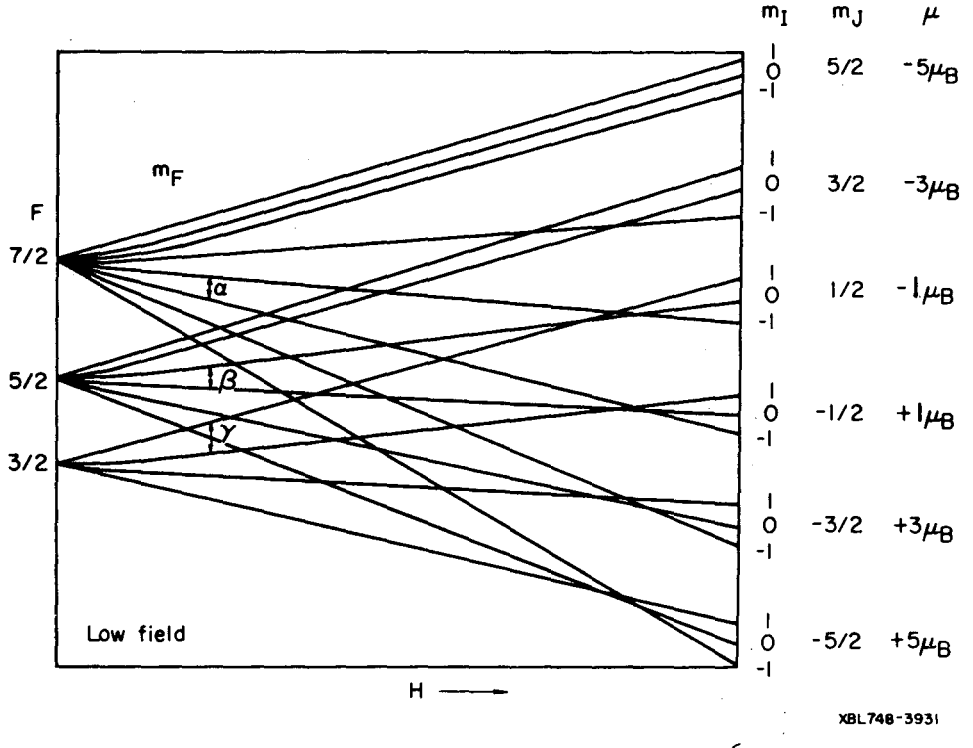

Fig. I. 10. Schematic Breit-Rabi diagram of $^6S_{5/2}$ state of nitrogen atoms with I = 1.

$$g_J = -1 - \frac{J(J+1) + S(S+1) - L(L+1)}{2J(J+1)} \qquad \text{(I. 17)}$$

m_J can take 2J + 1 values between -J and +J. A schematic Breit-Rabi diagram for $N^{14}(^6S_{5/2})$ is drawn in Fig. I.10. Expected atomic magnetic moments are on the right-hand side of the diagram.

The experiments we performed can be treated in three groups:

a) The efforts to obtain a reasonable peak in the metastable ^6S region of the time-of-flight spectrum.

b) Several tests on the other species that appear in the fast and the molecular regions of the time-of-flight spectrum.

c) The studies to distinguish and to prove the identity of those metastable dissociation fragments by deflection and resonance methods.

The first group of experiments are preparatory studies of nitrogen dissociation fragments of which we tried to develop the peak at about 320 μseconds to a workable degree by varying several experimental conditions. Source pressure, source design, cooling and cleaning the gas, source anode voltage, source filament current, electron emission current, the width of the slit and collimator were the variables. Each individual run lasted from two minutes to two hours. The detector having higher work function, would not detect the ground state[24] and the low-lying ^2D and ^2P states of atomic nitrogen. The electron gun pulse-repetition rate was also varied.

In most of these studies, the magnets were turned off to avoid any deflecting effects. However, some of these runs were made to study the throw-out percentages of various parts of the time-of-flight spectrum and the quenching effect of magnetic fields on the atomic and molecular species.

The tests mentioned in part b) were done in the hope of answering some unsolved questions and to regain our confidence in our apparatus by detecting very well known physical phenomena of Majorana transitions and measuring the quantities which are already established in the literature. R.F. and Majorana resonance studies on the $^3S_1$ states of helium,[25] $^3P_2$ states of argon and alkali ground states,[26] deflection studies on the excited nitrogen molecules, and the studies of the translational kinetic energy of very fast peak of nitrogen time-of-flight spectrum versus accelerating voltage of the electron gun can be considered in this group.

The experiments we expected to be most fruitful for our purpose fall into the third group. Our general procedure was the following. With a certain set of conditions, we obtained a time-of-flight spectrum of nitrogen fragments which gives a good peak in the expected metastable region when the A and B magnets were off and the source, collimator and detector slits were aligned properly. The set of conditions were slit and collimator widths, electron gun anode voltage, filament current, time duration per channel, repetition rate, and magnet currents. The next step was to bring the detector

to one side by a few mils, turn on the magnets and obtain a deflected time-of-flight spectrum. This routine was followed until the count rate drops down to a very low value as the detector moves away about 200-300 mils* from the center line. The distance between the two successive detector position depends on the resolution of the apparatus, i.e., the width of the slits, but a typical distance was 20 mils for 8 mils source slit, 10 mils collimator slit and 25 mils detector slit. Data was collected for about 15 minutes at each position. The electron gun accelerating voltage was held at 125-135 volts since it gave the best signal-to-background ratio. Although most of the data were taken with a 13.3 μsec electron gun pulse, (i.e., time per channel) we also had runs with 6 μsec/channel, and 40 μsec/channel. The duty cycle of the electron gun for 13.3 μsec/channel was 0.2% which corresponds to $1/(6.8 \times 10^{-3}) = 147 \ \ sec^{-1}$ repetition rate.

Figure I. 11 shows a schematic plot of the time-of-flight spectrum of fragments of nitrogen similar to the one obtained by Johnson, Fairchild and Garg. The solid line represents the data taken when there is no magnetic effect on the beam. If the species had magnetic moments, inhomogeneous magnetic field would deflect them to various distances from the center, depending on their velocity distribution. For a certain deflecting power of magnets, at various positions of the detector one would obtain the peaks shown by dashed lines. As it is seen from Equation I. 13, the graph of d versus t^2 gives us a straight line passing through the origin, its slope being

* 1 mil = 0.001 inch

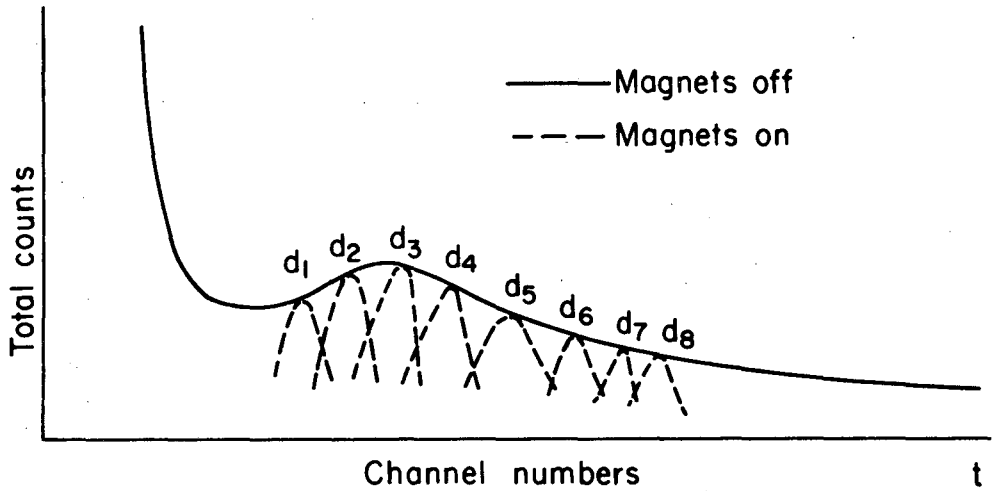

Fig. I. 11. Schematic time-of-flight spectrum of metastable nitrogen atoms.

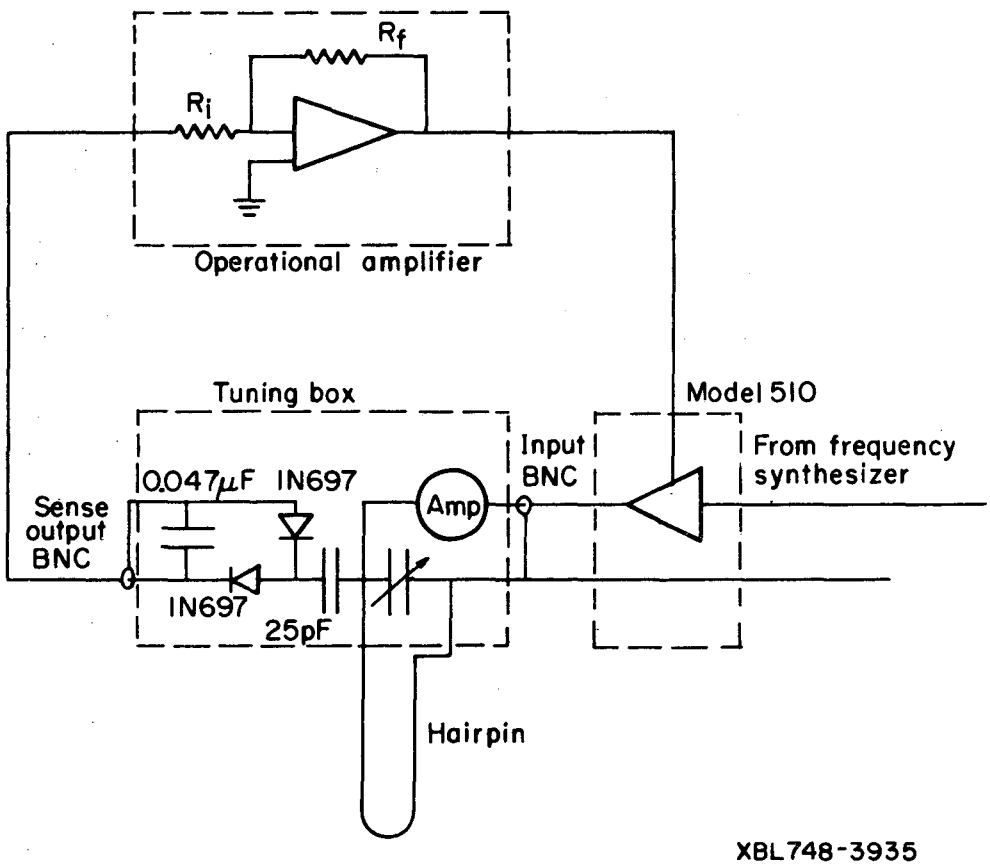

Fig. I. 12. Tuning box and r.f. control circuit.

proportional to the μ_{eff}. However, in order to determine the μ_{eff} in a reasonable precision, one should use calibration plots which were obtained with the same geometry of the apparatus, the same inhomogeneous magnetic fields and the same time per channel. The $^3S_1$ and $^3P_2$ metastable states of helium and argon, respectively, served very well for this purpose. We had eight calibration plots with different arrangements of magnetic fields, geometry and time per channel. They are listed in Table I. 1.

Certainly the best and most precise method to measure the atomic magnetic moments is the atomic beam magnetic resonance method. The theory and the principles of this method will be presented in Chapter II. Here we outline the experimental attempts to induce an r.f. transition between the energy levels of $^6S_{5/2}$ state of the nitrogen atom. A schematic Breit-Rabi diagram (Fig. I. 10) shows the α, β, and γ transitions. This state has 18 magnetic sub-levels which means that only 1/18 of the atoms are available for a particular transition. Another factor comes from the fact that the flight time of the ^6S nitrogen atoms to the detector is approximately 3 times that of the measured lifetime. In other words, only about 5% of the metastable atoms are able to reach the detector without decaying. Thus the total percentage of the atoms available for transition becomes roughly 0.3% of the metastable atoms which are originally directed toward the detector. In order to increase the transition probability, we used a 3" long hairpin. A tuning box, containing a variable condenser, was used to give a good impedance match. Furthermore, this system was

TABLE I. 1. Calibration chart for determining the atomic magnetic moments.

Slit Widths (mils)	Isotope	I_A (amps)	I_B (amps)	Time/ch (μsec)	μ (μ_β)	K_c
Source 8	He^4	1.8	4.5	13.3	2.0	.206
Collimator 10	He^4	5.0	5.0	13.3	2.0	.300
Detector 25	He^4	1.0	1.0	13.3	2.0	.106
	A^{40}	5.0	5.0	40.0	3.0	2.67
Source 3	He^4	1.8	4.5	13.3	2.0	.208
Collimator 6	A^{40}	1.8	4.5	40.0	3.0	2.04
Detector 12	A^{40}	0.9	1.3	80.0	3.0	3.61
					1.5	3.81
Source 8						
Collimator 12	He^4	1.8	4.5	13.3	2.0	.212
Detector 25						

controlled for a constant oscillation level by a servo-system which contained an operational amplifier. A diagram in Fig. I. 12 shows the details of the r.f. frequency and the control system.

D. Results and Discussion

After many different arrangements of experimental conditions, we have on occasion obtained encouraging time-of-flight spectra. A typical good-looking distribution is given in Fig I. 13. The data which belong to this time-of-flight spectrum are presented in Appendix A. The gas line pressure was about 1 torr, electron gun anode voltage was 150 volts; the detector was at the center of the beam line, magnets were off and counting time was two minutes. The source slit, collimator slit and detector slit were respectively 8, 10, and 25 mils. The time per channel was 13.3 μsec and the repetition rate was $1/(6.8 \times 10^{-3})\,\mathrm{sec}^{-1}$. The peak between channel 20 and 35 was expected to represent ^6S metastable state of atomic nitrogen. However, it was not readily reproducable under slightly different conditions. We could not determine a set of optimum conditions which always produce a peak in this interval of channels. Also it must be noted that the signal-to-background ratio could not be improved any further. We cooled down the gas by use of liquid nitrogen before entering into the filament cavity of the electron gun and tried to clean the gas by sending through a getter of hot tungsten. Neither of these precautions yielded a positive effect on the production.

Throw-out experiments with the B magnet off, the A magnet at

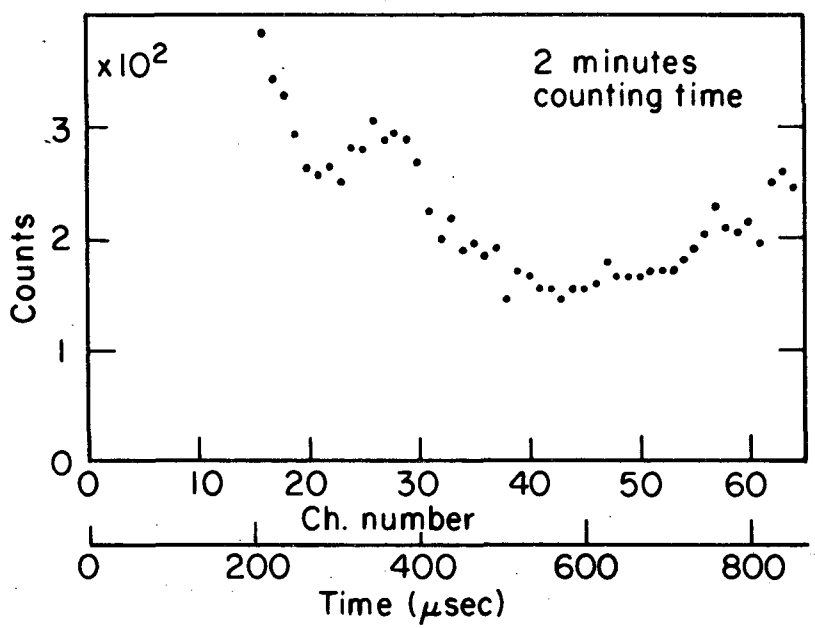

Fig. I. 13. Time-of-flight distribution of dissociation fragments of nitrogen.

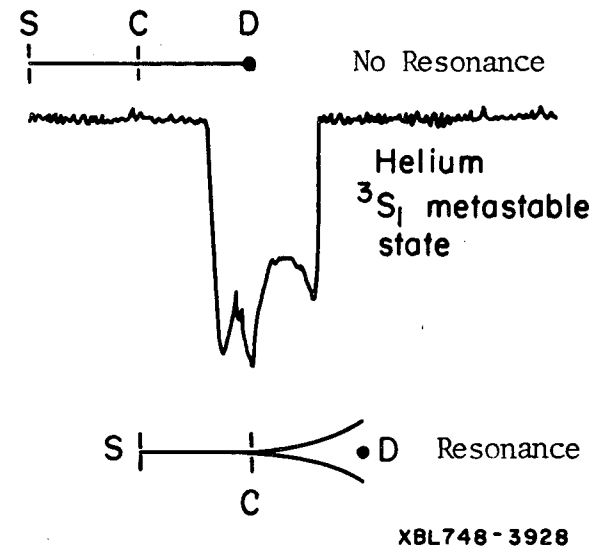

Fig. I. 14. Majorana pattern of $^3S_1$ metastable of helium. Upper and lower diagrams are the beam paths. S, C, and D indicate the source slits, collimator slits and detector, respectively.

maximum deflecting power (i.e., I_A = 5.0 ampere) and the detector sitting at the center showed that the species between the channels 22 and 35, which covers a good portion of the peak, were most effectively deflected toward the sides. The thrown-out percentage varied from 46.3% to 52.6%. The high energy photons, which we believe constitute the first two channels of the time-of-flight spectrum, were also affected as much as 15% when we turned the A magnet on. This fact convinced us that the stray magnetic field of A magnet decreases the productivity of the source. Similarly, the B magnet lowers the counting efficiency of the detector. The C magnet alone did not cause an observable effect on the count rates, indicating that none of the particles that we were interested in are quenched by the magnetic field.

The data given in the Appendix A has another peak with very high counts between channels 4 and 20. This is called "the fast peak" in the literature and still has not been identified properly. Fairchild, Garg and Johnson[6] have speculated that these peaks probably were due to neutral atoms or molecules produced by charge exchange of the fast ions in the electron gun. We have studied the behavior of this fast peak by varying the source pressure and electron gun anode voltage. It is true that we were not equipped to identify whether these particles were atoms or molecules. But, apparently they are not ions since a magnetic field of 5000 gauss would cause them to move in an orbit of a few millimeters radius. We have also noticed that their translational kinetic energy was about half or about the same as

the electron energy of the electron gun assuming, respectively, neutral nitrogen atoms and molecules. While the magnets were on, this fast peak remained at the same position in the time-of-flight distribution even when the detector moved about 200 mils away from the center. Although the counting rate decreased with distance from the centerline, it was the highest peak of all the distribution throughout the experiment, except for the first two photon channels. Therefore, one can also speculate that this fast peak might be due to some photons emitted as a result of some secondary phenomena taking place in the source. Throw-out studies showed that an average of 25% of the particles in this part of the distribution were missing or not reaching the detector while the photon counts were reduced only 8% when A magnet current was turned on to $I_A = 5.0$ ampere. Therefore, we tend to believe that fast peaks are due to neutral nitrogen atoms or molecules, emerged from the source at the end of some collisions with electrons, ions, neutral atoms or molecules. By increasing the source pressure, the width of the fast peak becomes larger and splits into two peaks. The higher anode voltage caused the peak to move toward the faster side (i.e., to the left side of the time-of-flight distribution). We found that the velocity of the particles in this peak is roughly proportional to the square root of the voltage applied to the anode of the electron gun.

In an atomic beam magnetic resonance apparatus, Majorana and low-field r.f. transition provide tests to the experimenter on

the operation of his equipment and system. In various phases of this experiment we utilized beams of noble gases such as helium and argon and alkali metal potassium to induce Majorana and r.f. transitions. We used both flop-in and flop-out geometries, with a terminated hairpin. The source and detector slits were set at various times to 10, 60 and 30 mils wide. The A and B magnet currents were set at various times to 1, 2, 3, 4, and 5 ampere. We observed low field r.f. transitions between the energy levels of $^3S_1$ metastable state of helium and also the Majorana pattern as shown in Fig. I. 14. Since the detector was at the center, a Majorana transition caused a dip (i.e., a flop-out resonance with this geometry which is also shown on the figure). The K^{39} resonance was observed using an oven-type source, hot-wire detector and a three-inch shorted hairpin at a magnetic field of 1.97 gauss. The Majorana resonance was also easily obtained with K^{39}. The details of alkali metal g_J factor measurements are explained in our earlier paper.[26] We have observed several Majorana transitions of argon during the deflection studies for calibration purposes.

In an effort to convince ourselves that the deflection studies yield reasonable results for the magnetic moments, we deflected nitrogen molecules in their metastable A $^3\Sigma_u^+$ state, and, by means of "the deflection versus the square of time-of-flight" plots, we determined very roughly a series of effective magnetic moments. The comparison element was argon with K = 3.61 and K = 3.81. As seen from the Table I. 1, the two molecular nitrogen runs were done with

80 μsec/channel, a 3 mils source, 6 mils collimator and 12 mils detector slit widths. Although the very narrow slit dimensions improved the resolution of the apparatus, one would desire much better resolution for a more careful molecular study. Yet, our results are in fair agreement with those listed by Freund, Miller, De Santis and Lurio.[27] Table I. 2 makes use of the g_J and J's for N = 0 - 4 taken from the above mentioned publication and compares

Table I. 2. A comparison of the theoretical and experimental magnetic moments (Bohr Magnetons) from deflection studies on metastable molecular nitrogen.

$\mu_{eff}=Jg_J$	$\bar{\mu}_{exp}$	$\mu_{eff}=Jg_J$	$\bar{\mu}_{exp}$
--	4.15	0.67	0.65
--	2.64	0.50	0.54
2.00	1.95	0.40	0.38
1.60	1.67	0.34	--
1.50	1.51	0.30	0.31
1.33	1.35	0.20	0.21
1.20	1.15	0.17	0.16
1.00	1.04	0.10	0.12
0.80	0.86		

the calculated effective magnetic moments with the average obtained from our two runs. Here N represents the total angular momentum of

the molecule exclusive of both electronic spin and nuclear spin angular momenta. In such a complicated structure it is impossible to assign the correct quantum numbers to the effective magnetic moments which are obtained by Stern-Gerlach time-of-flight method. Therefore, we have listed our experimental average μ_{eff} values in decreasing order of magnitude. The first two of the experimental values are even not comparable with the values calculated by using their list. The interested reader is referred to the above mentioned publication for the accurate molecular beam magnetic resonance method and a thorough discussion of the theoretical aspects of the spectrum of $N_2(A^3\Sigma_u^+)$.

The discussion in the first paragraph of the experimental part of this thesis, which is about the deflection of an atom with a magnetic moment μ in an inhomogeneous magnetic field, was done assuming a continuous inhomogeneous magnetic field over all the flight path of the atom. In an atomic beam machine, however, this is not the actual case. We have two inhomogeneous magnetic fields separated from each other by a distance of 1.5 times of their length. Since we make comparison measurements, this fact does not play an important role. A measurement of a known magnetic moment showed us the uncertainty due to this assumption is not bigger than 5%. Especially nitrogen $^6S_{5/2}$ metastable states having magnetic moments of $5\mu_B$, $3\mu_B$ and $1\mu_B$ should be observed with no difficulty provided that, of course, they are produced effectively. The vital importance of production caused us to try six different sources and many designs and application

variations on them. We had performed about 70 atomic nitrogen deflection runs to search for these magnetic moments. These runs were evaluated by making use of the calibration chart, Table I·1., which was obtained by calibration runs throughout the experiment. We have selected a sample time-of-flight distribution of metastable nitrogen. It is shown in Fig. I. 15. The distribution, when calibrated by using the first helium run on the calibration chart, nicely indicates the $5\mu_B$, $3\mu_B$ atomic magnetic moments. The magnet currents were $I_A = 1.8$ ampere, $I_B = 4.5$ ampere. The source slit had a width of 8 mils, collimator slit 10 mils, and detector slit 25 mils. The detector was 30 mils away from the alignment center. The time for electron gun pulse and for each channel was 13.3 μ seconds. This data was collected in one hour. As it is seen from the plot, the statistics are not very good, and, besides, the distribution could not be repeated under the same conditions. Among the 70 complete runs, each containing about seven such distributions we have only a few time-of-flight distributions giving us the expected 5, 3, and 1 Bohr Magnetons atomic magnetic moments. We were not able to follow the displacement of these magnetic moments on the Stern-Gerlach time-of-flight distribution as the detector moved away from the alignment center. They were intermittently appearing which could also be attributed to the poor statistics. Even when good statistics were acquired, our efforts to differentiate these magnetic moments by molecular beams magnetic resonance methods have failed. At low magnetic field, the $^6S_{5/2}$ $g_J \simeq -2$ nitrogen atom with nuclear spin I = 1 has F levels with g factors

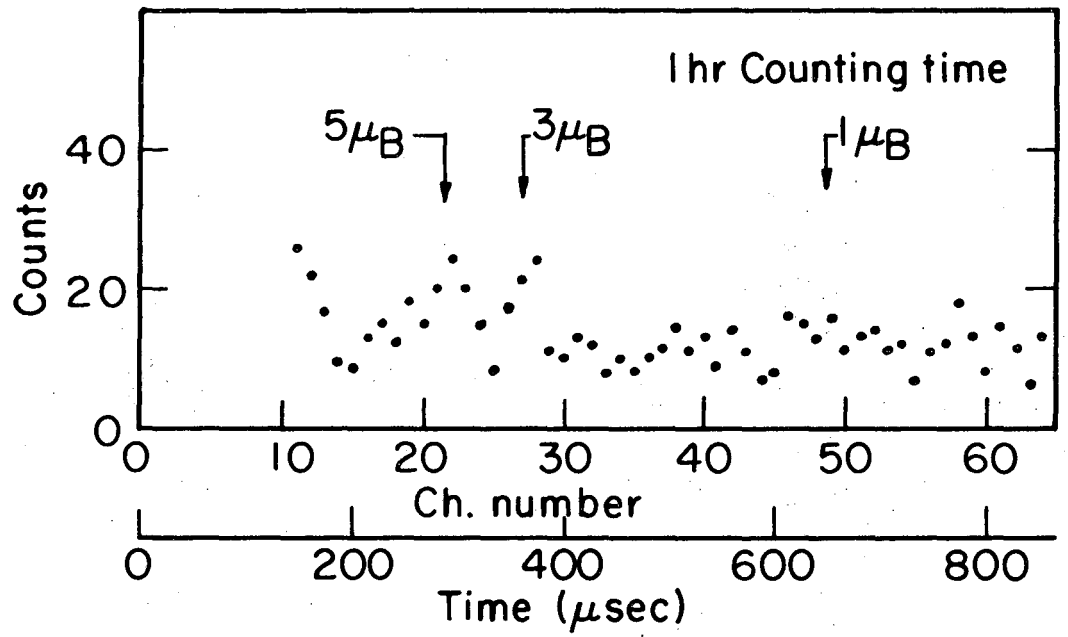

Fig. I. 15. A sample Stern-Gerlach time-of-flight distribution of the dissociation fragments of nitrogen.

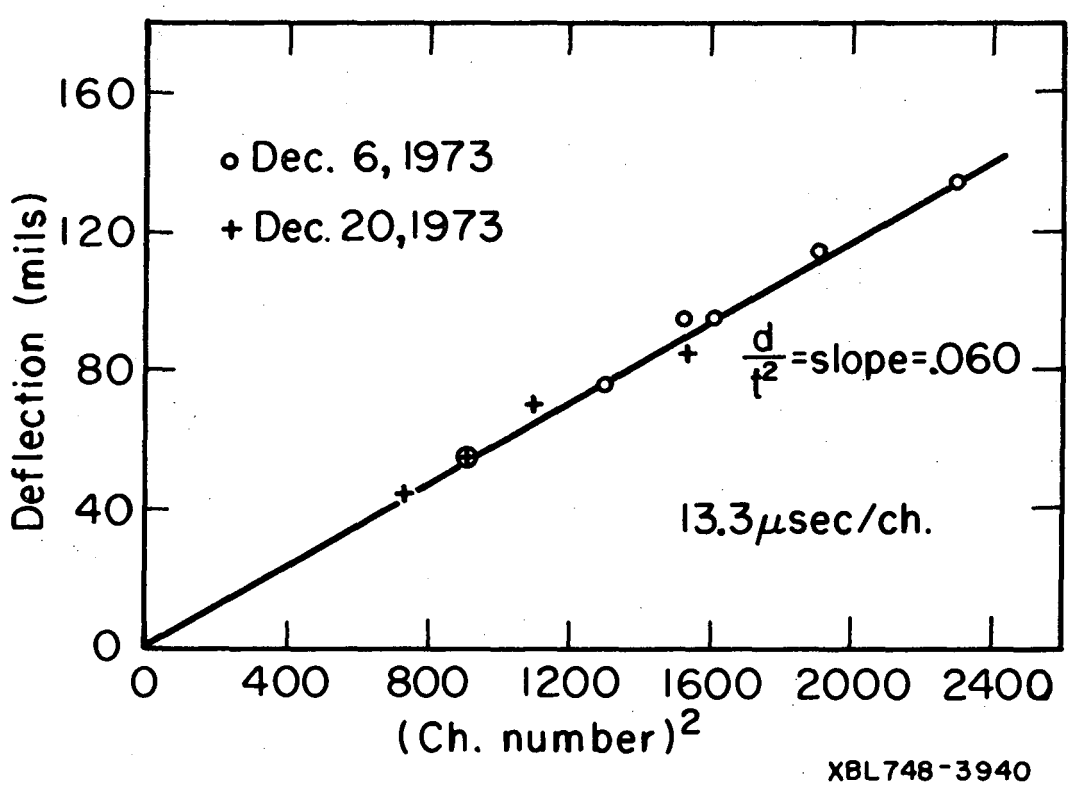

Fig. I. 16. The deflection of the atoms with $\mu = 4\mu_B$ versus time squared.

given by $g_\alpha \simeq -1.43$, $g_\beta \simeq -1.77$ and $g_\gamma \simeq -2.8$. (See Fig. I.10) Using $\nu = g(\mu_B/h)H$ to predict resonance locations, we have swept a large range of r.f. frequency with no success in finding a resonance.

Although a systematic study of the Stern-Gerlach time-of-flight spectrum for the magnetic moments of 5, 3, and 1 Bohr Magnetons was not too successful, we have observed 4 and 2 μ_B in a number of runs. (See Fig. I. 17) A computer program was prepared to search for all possible L and S couplings which yield magnetic moments lying between 4.25 μ_B and 3.75 μ_B. Thus one could have a list of possible states to which a certain atomic moment could be assigned. This program is given in Appendix B. Since atomic nitrogen has an odd number of electrons, this program calculates μ only for S = 1/2, 3/2, 5/2. L goes from 0 to 30. No satisfactory assignment to the $4\mu_B$ peak could be made, so we looked for other possible explanations.

Fig. I. 16 summarizes the result of two different runs giving rise to an atomic magnetic moment of 4 μ_B. Dates of the runs are shown on the graph. Another interesting finding of this experiment was a series of large atomic magnetic moments ranging from 6 μ_B to 22 μ_B. Certainly very large magnetic moments are not easily detected in our apparatus, since they have to move very fast to be deflected in the range of our detector. But, such fast particles would then fall in the shadow of the fast peak in the time-of-flight distribution. A sample distribution in Fig. I. 17 contains both a $13\mu_B$ and $4\mu_B$ peaks. However, $13\mu_B$ peak may be a composite of several peaks since they were expected to be very closely spaced on that part of the distribution.

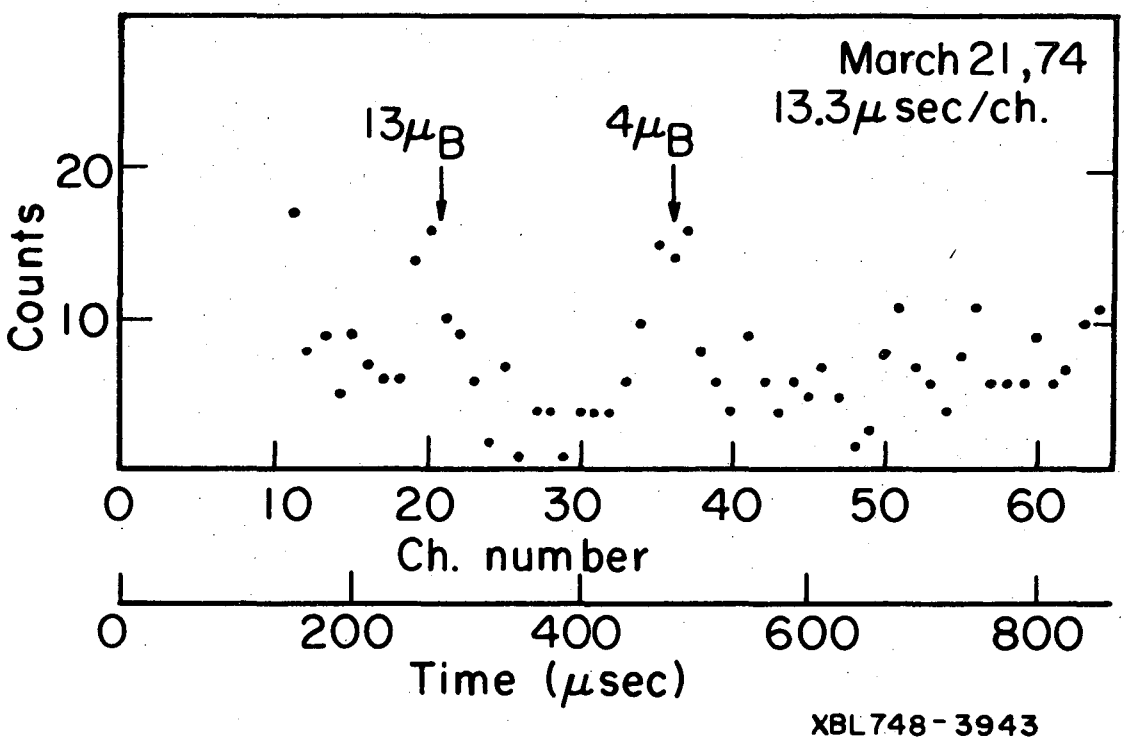

Fig. I. 17. A Stern-Gerlach time-of-flight distribution having two main peaks of $13\mu_B$ and $4\mu_B$.

The deflection from the center of alignment was 80 mils for this particular run. The data collection time was one hour. On various occasions we have observed the peaks corresponding to 8, 9, 10, 15, 16, 20 μ_B etc. We believe that these peaks are due to high-Rydberg nitrogen atoms. On the other hand, the peaks corresponding to 4 μ_B became smaller after we fixed an extremely small vacuum leak in the gas-feeding system indicating that this peak was possibly due to a constituent of air. Feeding some air into the system confirmed this idea, since it produced much bigger peaks at the same location of the distribution. We later proved that this peak is due to the metastable $^5S_2$ state of atomic oxygen. However, even with a reagent mass-spectrometer-grade nitrogen, and a leak-free vacuum system, this peak did not disappear totally until we replaced the two plastic (Tygon) hoses in the gas feed system with copper tubing. From eleven out of thirteen plastic materials tested by Barton and Govier,[28] the main component of the residual outgassing was H_2O. Apparently this remaining small peak owed its existence to the outgassing property of the plastics.

II. g_J FACTOR OF $3p^3 3s\ ^5S_2$ METASTABLE STATE ATOMIC OXYGEN

In the second phase of our experimental studies we measured the g_J factor of $^5S_2$ metastable state of atomic oxygen by the molecular beam magnetic resonance method to a precision of 0.5 ppm. Although the theory on which our experiment was based is relatively simple because of the zero nuclear magnetic moment of O^{16}, here we present the outlines of the general theory involved. We try to indicate the physical reality behind the mathematical calculations. We then go to the specific case of our measurement by substituting particular quantities into the general equations.

A. Theory

Multipole Moments of an Atom. The interaction between the nucleus and electrons of an atom can be considered under two main categories; electrostatic interactions and magnetic interactions. There may be a non-spherical distribution of the charge and the magnetic dipole strength inside the nucleus since the nucleus is composed of neutrons and protons and has a spin I which can have the values of 0, 1/2, 1, 3/2, . . . etc. Therefore, in general a multipole expansion is necessary to describe the interactions between the electrons and the nucleus.

a) Electrostatic interactions.

ρ_e being the charge density of the electrons in the volume element dV_e and ρ_n being the charge density of the nucleus in the volume element of dV_n, the electrostatic interaction energy, W_E, can be written as

$$W_E = \int_{V_e}\int_{V_n} \frac{\rho_e(\vec{r}_e)\ \rho_n(\vec{r}_n)}{|\vec{r}_e - \vec{r}_n|}\ dV_e\ dV_n \qquad \text{II. (1)}$$

where $\vec{r}_e$ is the position vector of the volume element dV_e of the electrons, $\vec{r}_n$ is the position of the volume element dV_n of the nucleus. If we use the cosine law and Legendre polynomials, we can expand $\frac{1}{|\vec{r}_e - \vec{r}_n|}$ into the power series

$$\frac{1}{|\vec{r}_e - \vec{r}_n|} = \left(r_e^{\ 2} + r_n^{\ 2} - 2r_e r_n \cos\Theta_{en}\right)^{-1/2} =$$

$$\sum_{k=0}^{\infty} r_e^{\ -(k+1)}\ r_n^k\ P_k\ (\cos\Theta_{en}) \qquad \text{II. (2)}$$

where

$$P_k = \frac{1}{2^k k!}\ \frac{d^k}{d(\cos\Theta_{en})^k}\ (\cos^2\Theta_{en} - 1)^k. \qquad \text{II. (3)}$$

Using the spherical-harmonic addition theorem[29] the Legendre polynomial

of cos Θ_{en} can be written as

$$P_k = \sum_{q=-k}^{k} (-1)^q \, C^k_{-q} \, (\Theta_n, \phi_n) \, C^k_{+q} \, (\Theta_e, \phi_e) \qquad \text{II. (4)}$$

with the definition

$$C^k_q \, (\Theta,\phi) = \left(\frac{4\pi}{2k+1}\right) Y^k_q \, (\cos\Theta, \phi) \qquad \text{II. (5)}$$

where Y^k_q is the normalized tesseral harmonic which includes the associated Legendre polynomial. Angles Θ_e, ϕ_e, Θ_n, ϕ_n and Θ_{en} are shown in Fig. II. 1.

Now the interaction energy can be written as

$$W_E = \sum_k \int_{V_e} \int_{V_n} \frac{\rho^e_e \, \rho_n}{r_e} \left(\frac{r_n}{r_e}\right)^{-k} P_k \, (\cos\Theta_{en}) \, dV_e \, dV_n \qquad \text{II. (6)}$$

and finally

$$W_E = \sum_k W_{ek} = \sum_k Q^k \cdot F^k \qquad \text{II. (7)}$$

where W_{Ek} is the electrostatic interaction energy from the multipole moment of the order 2^k. Thus the k = 0 term corresponds to an electric monopole, k = 1 to electric dipole, k = 2 to electric quadrupole, k = 3 to electric octupole moment. Q^k and F^k are the irreducible tensors

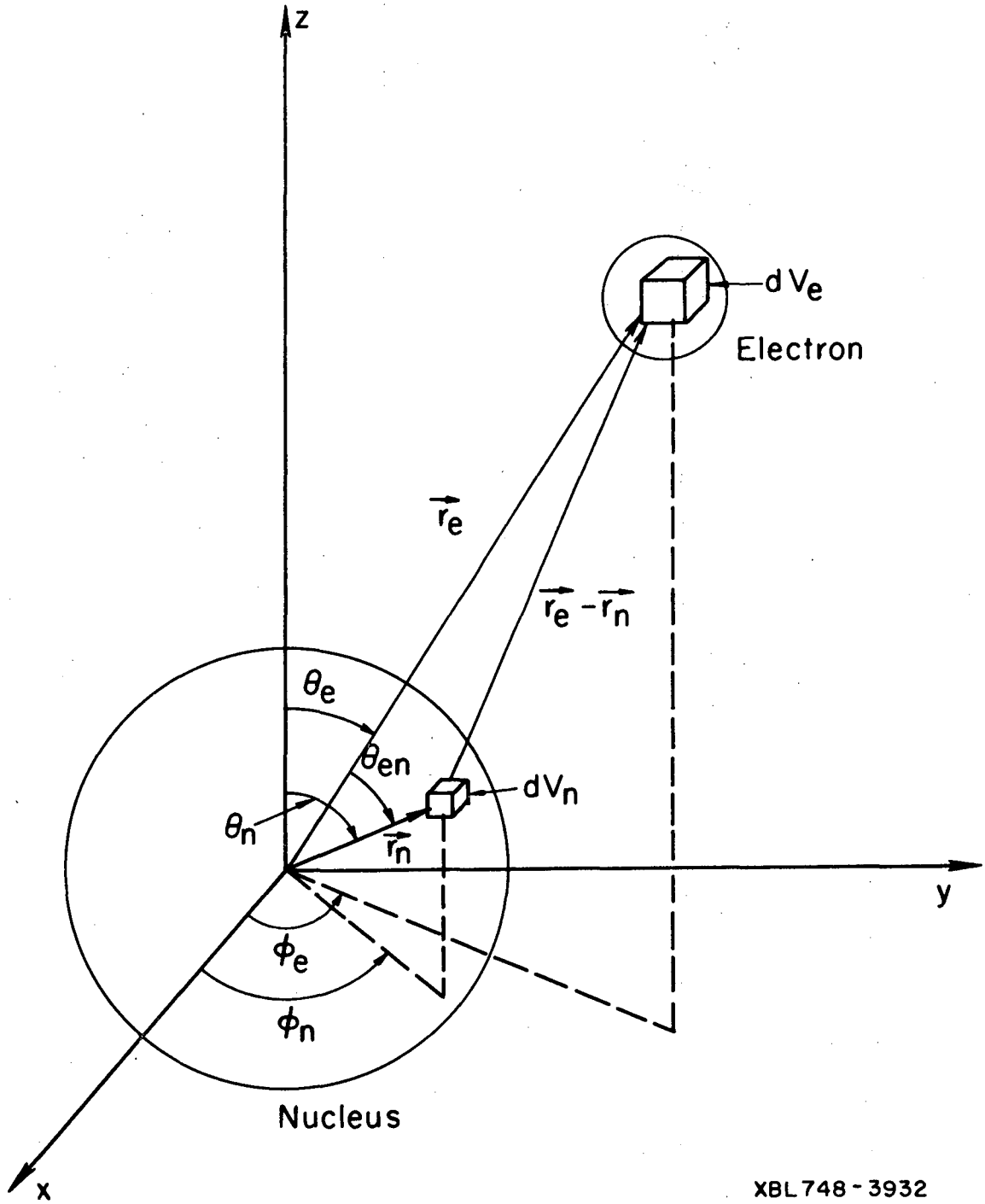

Fig. II. 1. Schematic diagram of the electrostatic interactions in an atom.

given as

$$Q_q^k = \int_{V_n} \rho_n \, r_n^k \, C_q^k \, (\Theta_n, \phi_n) \, dV_n \qquad \text{II. (8)}$$

and

$$F_q^k = \int_{V_e} \rho_e^e \, r_e^{-(k+1)} \, C_q^k \, (\Theta_e, \phi_e) \, dV_e \qquad \text{II. (9)}$$

where ρ_e^e indicates that the electronic charges are outside of the nuclear radius. The interaction energy from the multiple moment of order 2^k is then written as

$$W_{Ek} = \sum_{q=-k}^{k} (-1)^q \, Q_q^k \, F_{-q}^k \qquad \text{II. (10)}$$

which is separated into the two terms containing, respectively, only nuclear and electronic coordinates.

Considering the parity of Y_q^k, it can be shown that $W_{Ek} = 0$ for odd k.[30] In other words, electric dipole and electric octupole moment interactions do not exist. Furthermore, it has been proved that, respectively Q_q^k and F_{-q}^k vanish when $k > 2I$ or $k > 2J$. So the number of multipoles are limited either by I or J, whichever is smaller. For $I = 0$, only the electric monopole is possible. However, in general electric multipoles are

$$W_E = W_{E0} + W_{E2} + W_{E4} + \ldots \qquad \text{II. (11)}$$

where the monopole interaction

$$W_{E0} = Ze\sum_{i}^{Z} \frac{e}{r_i} \qquad \text{II. (12)}$$

which is simply the Coulomb interaction. W_{E2} and W_{E4} represent the electric quadrupole and electric 16-pole interaction terms.

b) Magnetic Interactions.

Magnetic interactions are due to the circulating currents in the region of electrons and nucleons. The mutual magnetic potential energy between the nucleus and electrons can be written in terms of nuclear current density $\vec{J}_n$ and the vector potential $\vec{A}_e$ produced by the electron current density $\vec{J}_e$ at the nucleus or similarly in terms of electron current density at the region of electrons.

$$W_M = -\frac{1}{c} \quad \vec{J}_n \cdot \vec{A}_e \, dV_n = -\frac{1}{c} \int_{V_e} \vec{J}_e \cdot \vec{A}_n \, dV_e \, . \qquad \text{II. (13)}$$

Making use of the continuity equation for the stationary current distribution

$$\vec{\nabla} \cdot \vec{J} = -\frac{d\rho}{dt} = 0 \qquad \text{II. (14)}$$

and deriving the nuclear current density $\vec{J}_n$ from the magnetization vector $\vec{M}_n$ at the nucleus

$$\vec{J}_n = c\vec{\nabla} \times \vec{M}_n \, . \qquad \text{II. (15)}$$

Vector algebra leads to

$$W_M = \int_{V_e} \int_{V_n} \frac{(\vec{\nabla}_n \cdot \vec{M}_n)\ (\vec{\nabla}_e \cdot \vec{M}_e)}{\vec{r}_e - \vec{r}_n}\ dV_n\ dV_e \qquad \text{II. (16)}$$

where $\vec{M}_e$ is the magnetization vector at the region of electrons. Schwartz[31] proved that this interaction energy can be expressed as

$$W_M = \sum_{k=0}^{\infty} W_{Mk} \qquad \text{II. (17)}$$

where

$$W_{Mk} = \sum_{\mu=-k}^{k} \frac{4\pi}{2k+1} \int_{V_n} \psi_n^* \left[\mu_N \left(\frac{2g_{nl}\ \vec{L}_n}{k+1} + g_{ns}\ \vec{S}_n \right) \cdot \left(\nabla_n\ r_n^{\ k}\ Y_{k\mu}^*(n) \right) \right] \psi_n\ dV_n \cdot \int_{V_e} \psi_e^* \left[-2\mu_B \left(\frac{-\vec{L}_e}{k} + \vec{S}_e \right) \cdot \left(\nabla_e\ r_e^{\ -(k+1)}\ Y_{k\mu}(e) \right) \right] \psi_e\ dV_e \qquad \text{II. (18)}$$

As it is seen clearly, nuclear and electronic terms are completely seperated. μ_N and μ_B are the nuclear magneton and Bohr magneton, g_{ne} and g_{ns} are, respectively, the nuclear g factors of orbital angular momentum and spin angular momentum.

From the similarity between Equations II. (17) and II.(10) one can put the following restrictions on k: $k \leqslant 2I$ and $k \leqslant 2J$, whichever is smaller. However, the parity of the operators in the integrals is $(-1)^{k+1}$, indicating that the even order of magnetic multipole

interactions vanish. Therefore, the existing magnetic multipoles are

$$W_M = W_{M1} + W_{M3} + W_{M5} + \ldots \qquad \text{II. (19)}$$

the magnetic dipole, octupole, 32-pole, etc.

Now the Hamiltonian of an atom can be written as the summation of the several terms

$$\mathcal{H} = \mathcal{H}_n + \mathcal{H}_e + \mathcal{H}_{E,m} + \mathcal{H}_r + \mathcal{H}_{s-o} + \mathcal{H}_{hfs} \qquad \text{II. (20)}$$

The first two terms are respectively due to the kinetic energies of the rotating nucleus and orbital motion of the electrons. The third term is the electric monopole interaction Hamiltonian which is given in Equation II. (12). $\mathcal{H}_r$ is the Coulomb repulsion interaction term

$$\mathcal{H}_r = \sum_{i > j}^{z} \frac{e^2}{r_{ij}} \qquad \text{II. (21)}$$

which causes the electronic energy shells to be broken into the sub-shells and a mixing between the neighbor shells due to its shielding effect. The other effect of the Coulomb repulsion interaction is the coupling effect. Since the interaction energy depends on the magnitude of the total orbital angular momentum L of the system and the choice of L is restricted by S, energy of a certain configuration splits into a number of terms labeled by ^{2S+1}L according to the different sets of L and S. Therefore, L and S are "good" quantum numbers and J has

not been determined yet. The spin-orbit interaction Hamiltonian $\mathcal{H}_{s-o}$ can be written as

$$\mathcal{H}_{s-o} = \frac{1}{2m^2c^2} \sum_{i=1}^{z} \frac{1}{r_i} \frac{dU_i(r_i)}{dr_i} \vec{l}_i \cdot \vec{s}_i \qquad \text{II. (22)}$$

It is apparent that the energy of interaction depends on $\vec{j}_i^{\,2}$ for the fixed magnitudes of $\vec{l}_i$ and $\vec{s}_i$ since

$$\vec{l}_i \cdot \vec{s}_i = \frac{1}{2} (\vec{j}_i^{\,2} - \vec{l}_i^{\,2} - \vec{s}_i^{\,2}) \qquad \text{II. (23)}$$

where $\vec{j}_i = \vec{l}_i + \vec{s}_i$. For a non-closed shell, if the Coulomb repulsion interaction is absent, a different energy would correspond to every allowed parameters $(j_1, j_2, \ldots j_k)$ of a configuration. Since there is no orientation correlation between j_i's, the total angular momentum is not unique. Therefore, the degeneracy cannot be removed only by the spin orbit interaction. But the combined effect of spin orbit interaction and repulsion interaction forms a unique $\vec{J}$.

$$\vec{J} = \sum^{k} \vec{j}_i = \vec{L} + \vec{S} \qquad \text{II. (24)}$$

where k is the number of electrons in the non-closed shell. The energy levels depend only on the magnitude of $\vec{J}$. J is the new "good" quantum number. There is still a degeneracy of energy levels due to the orientation of $\vec{J}$ in the space.

There are two approximations which are used to calculate the interaction energy.

i) L-S coupling:

This is also called the Russell-Saunders coupling. It is applied in the cases $\mathcal{H}_r >> \mathcal{H}_{s-o}$ which represents the case in most of the atoms.

$$\left.\begin{array}{l} \sum \vec{l}_i = \vec{L} \\ \sum \vec{s}_i = \vec{S} \end{array}\right\} \longrightarrow \left(\vec{L}, \vec{S}\right) \longrightarrow \vec{J} \qquad \text{II. (25)}$$

ii.) j-j coupling:

This is the case when $\mathcal{H}_r < \mathcal{H}_{s-o}$ which is true for the highly excited states of atoms. Here the scheme is

$$\left.\begin{array}{l} \vec{l}_i + \vec{s}_i = \vec{j}_i \\ \cdot\ \cdot\ \cdot\ \cdot\ \cdot\ \cdot \\ \vec{l}_k + \vec{s}_k = \vec{j}_k \end{array}\right\} \longrightarrow \left(\vec{j}_i\text{'s}\right) \longrightarrow \vec{J} \qquad \text{II. (26)}$$

The last term in Equation II. (20) is the hyperfine structure interaction $\mathcal{H}_{hfs}$ which is due to the nuclear spin dependent terms of the electrostatic and magnetic interactions between the nucleus and electrons. The Hamiltonian of this interaction can be written as

$$\mathcal{H}_{hfs} = \sum_{k=1}^{\substack{2I \\ 2J}} \left[\mathcal{H}_{Ek}\right]^{1/2\left[1 + (-1)^k\right]} \cdot \left[\mathcal{H}_{Mk}\right]^{1/2\left[1 - (-1)^k\right]} \qquad \text{II. (27)}$$

which excludes the electrostatic monopole interaction. The summation is taken up to 2I or 2J, whichever is smaller. $\mathcal{H}_{Ek}$ and $\mathcal{H}_{Mk}$ represent, respectively, the electrostatic interaction Hamiltonian and magnetic interaction Hamiltonian.

It is evident that if J = 1/2, (i.e., k = 1) the only contribution to the hyperfine structure Hamiltonian comes from the magnetic dipole moment. Schwartz[31] derives the magnetic dipole moment from Equation II. (17) by making use of Racah's technique.[32] Using his result, then hyperfine structure Hamiltonian is

$$\mathcal{H}_{hfs} = ha\, \vec{I} \cdot \vec{J} \qquad \text{II. (28)}$$

where a can be called either the magnetic dipole interaction or the hyperfine structure constant. ha is given by

$$ha = -\frac{\mu_I}{I} \frac{\vec{H}_J \cdot \vec{J}}{\vec{J} \cdot \vec{J}} \qquad \text{II. (29)}$$

where $\vec{H}_J$ is the magnetic field at the nucleus due to the orbital motions and spins of the electrons. μ_I is the magnetic moment of the nucleus. In the absence of an external magnetic field or even in a weak magnetic field, according to the conservation of momentum, both $\vec{I}$ and $\vec{J}$ precess about the direction of $\vec{F}$ which is simply obtained by the vector summation of $\vec{I}$ and $\vec{J}$.

$$\vec{F} = \vec{I} + \vec{J} \qquad \text{II. (30)}$$

Therefore one can write

$$\vec{I} \cdot \vec{J} = \frac{1}{2}\left(\vec{F}^2 - \vec{I}^2 - \vec{J}^2\right) \qquad \text{II. (31)}$$

and

$$W_{hfs}\ (F) = \frac{ha}{2}\left[F\ (F + 1) - I\ (I + 1) - J\ (J + 1)\right] \qquad \text{II. (32)}$$

The energy difference between the levels with F = F and F = F -1 is then

$$\Delta W_{hfs} = W_{hfs}(F) - W_{hfs}(F - 1) = haF \qquad \text{II. (33)}$$

or in terms of frequency

$$\Delta\nu = aF \qquad \text{II. (34)}$$

where $\Delta\nu$ is known as the hyperfine structure separation. We do not see any practical need to examine further details of the theory of hyperfine structure. Also higher interaction terms, such as electric quadrupole, magnetic octupole, etc., are beyond our need. Instead, we shall discuss the behavior of an atom in the external magnetic field.

Atom in the External Magnetic Field. When an atom is placed in a uniform external magnetic field, we usually expect three parameters of the atom to interact with the field. These parameters are the

orbital angular momentum of the electrons, $\vec{L}$, total electron intrinsic moment $\vec{\mu}_S$ and the nuclear magnetic moment $\vec{\mu}_I$. The energy of interaction for each of these parameters can be expressed as

$$W = - \vec{\mu} \cdot \vec{H} \qquad \text{II. (35)}$$

a) Interaction of $\vec{L}$ with the Magnetic Field.

If the average current due to the orbital motion of electrons is I and $\vec{a}$ is the average area swept by electrons, the magnetic moment due to this motion is classically given by

$$\vec{\mu}_L = I\vec{a} = \frac{e\hbar}{2mc} \vec{L} \qquad \text{II. (36)}$$

Thus we can directly substitute Equation II. (36) into Equation II. (35) to obtain the interaction Hamiltonian.

$$\mathcal{H}_L = - \frac{e\hbar}{2mc} \vec{L} \cdot \vec{H} \qquad \text{II. (37)}$$

We remember that the Bohr Magneton is given by

$$\mu_B = \frac{e\hbar}{2mc} = 9.27 \times 10^{-21} \text{ erg/gauss} \qquad \text{II. (38)}$$

Therefore

$$\mathcal{H}_L = - \mu_B \vec{L} \cdot \vec{H} \qquad \text{II. (39)}$$

The angular momentum of the orbital electrons will vary in direction because of the torque experienced by orbiting electrons in the external magnetic field:

$$\vec{\tau} = \vec{\mu}_L \times \vec{H} \qquad \text{II. (40)}$$

and according to Newton's Law

$$\frac{d\vec{L}}{dt} = \vec{\tau} = \frac{e\hbar}{2mc} \vec{L} \times \vec{H} \qquad \text{II. (41)}$$

which yields an angular frequency of precession

$$\vec{\omega} = \left(\frac{e}{2mc}\right) \vec{H} \qquad \text{II. (42)}$$

known as the Larmor frequency. The vector diagram in the Fig. II. 2 shows the angular momentum $\hbar\vec{L}$, the magnetic moment due to orbital motions of the electrons

$$\vec{\mu}_L = \mu_B \vec{L} \qquad \text{II. (43)}$$

and the angle Θ between $\vec{L}$ and $\vec{H}_1$. On the other hand, this precession motion of the electron generates a magnetic field at the nucleus causing a modification on the external magnetic field seen by the nucleus. This effect is called the diamagnetic shielding effect. Since the energy contribution due the precession of the electron is

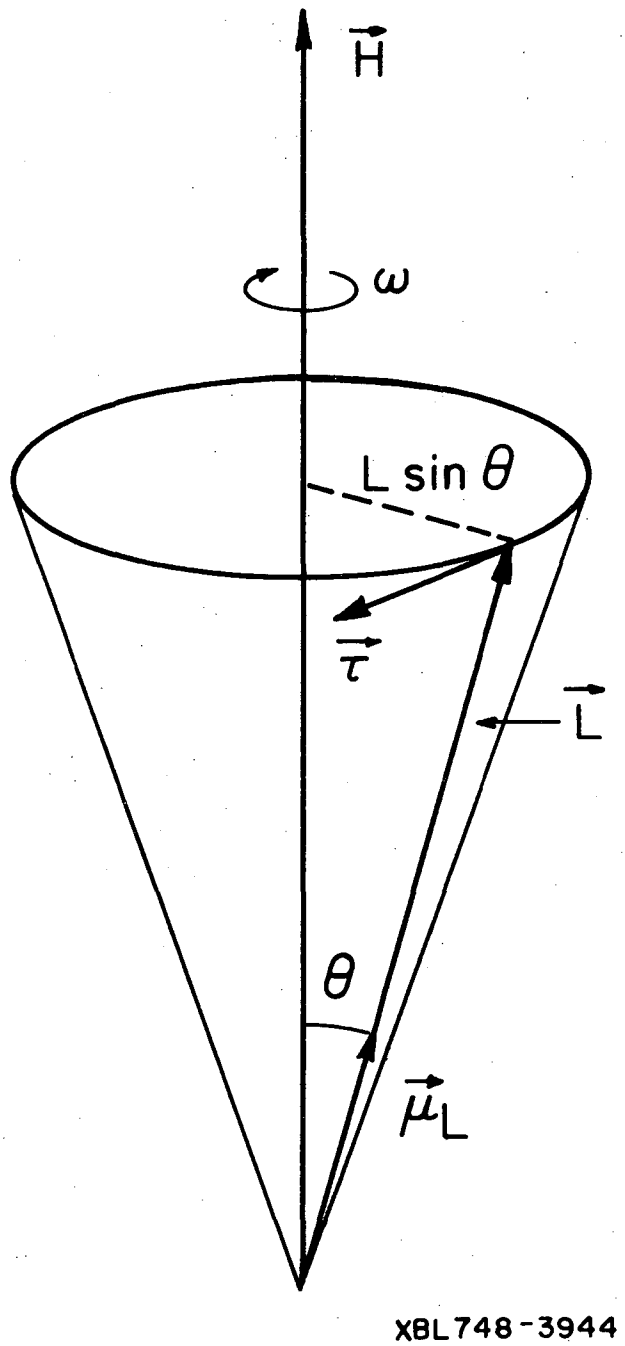

Fig. II. 2. Schematic illustration of the Larmor precession.

very small compared to $\mathcal{H}_L$, we will not discuss it further.

b) Interaction of $\vec{S}$ with the Magnetic Field.

Dirac's relativistic wave mechanics assigns an intrinsic angular momentum to the electron[33] which in turn creates a magnetic dipole moment

$$\vec{\mu}_S = \frac{e\hbar}{mc} \vec{S} \qquad \text{II. (44)}$$

Then the interaction Hamiltonian is given by

$$\mathcal{H}_S = 2\mu_B \vec{S} \cdot \vec{H} \qquad \text{II. (45)}$$

c) Interaction of $\vec{I}$ with the Magnetic Field.

By comparison with the above a) and b) cases we may write the nuclear magnetic dipole moment as

$$\vec{\mu}_I = \mu_B g_I \vec{I} \qquad \text{II. (46)}$$

where g_I is the nuclear g factor and $\vec{I}$ is the nuclear spin. If we consider the nuclear magneton

$$\mu_n = \frac{e\hbar}{2m_p c} = 5.05 \times 10^{-24} \text{ erg/gauss} \qquad \text{II. (47)}$$

we see that g_I must be of the order of 10^{-3} since

$$\vec{\mu}_I = \mu_n \frac{m_p}{m} g_I \vec{I} \qquad \text{II. (48)}$$

where m_p is the mass of the proton. g_I represents the gross structure of the nucleus. Finally, the interaction Hamiltonian of the nuclear magnetic moment with the external magnetic field can be expressed as

$$\mathcal{H}_I = \mu_B g_I \vec{I} \cdot \vec{H} \qquad \text{II. (49)}$$

d) Total Interaction of the Atoms with the Magnetic Field.

Certainly one can assign corresponding g factors to the orbital magnetic moments and intrinsic magnetic moment of the electrons. Using these g factors, the total magnetic field interaction Hamiltonian of the atom will be written as a perturbation added to the total Hamiltonian of the atom given by the Equation II. (20). It should be noted, however, that $\mathcal{H}_{hfs}$ term in the Equation II. (20) is now considered as a part of the perturbation Hamiltonian.

$$\mathcal{H}_{per.} = \mathcal{H}_{hfs} + \mathcal{H}_H \qquad \text{II. (50)}$$

or

$$\mathcal{H}_{per.} = ha \vec{I} \cdot \vec{J} + \mu_B g_L \vec{L} \cdot \vec{H} - \mu_B g_S \vec{S} \cdot \vec{H} + \mu_B g_I \vec{I} \cdot \vec{H} \qquad \text{II. (51)}$$

The $\mathcal{H}_H$ term is of the order of 10^{-4} ev even at a reasonably high field

such as about 10^4 gauss. The presence of g_L and g_S generalizes the equation for the cases in which g_L and g_S, respectively, differ from - 1 and - 2 due to the small correction terms. The above equation can be written in a more compact form if we take the coupling between $\vec{L}$ and $\vec{S}$ into account

$$\vec{\mu}_J = \vec{\mu}_L + \vec{\mu}_S \ . \qquad \text{II. (52)}$$

Then

$$g_J\vec{J} = g_L\vec{L} + g_S\vec{S} \qquad \text{II. (53)}$$

or

$$g_J\vec{J} \cdot \vec{J} = g_L\vec{L} \cdot \vec{J} + g_S\vec{S} \cdot \vec{J} \qquad \text{II. (54)}$$

which is obtained by multiplying both sides by $\vec{J}$ on the right. Therefore, similar types of equations, as Equation II.(31), would give

$$g_J\vec{J}^2 = \frac{g_L}{2}\left(\vec{J}^2 + \vec{L}^2 - \vec{S}^2\right) + \frac{g_S}{2}\left(\vec{J}^2 + \vec{S}^2 - \vec{L}^2\right) \qquad \text{II. (55)}$$

Dividing both sides by $\vec{J}^2$ and writing the equation in terms of quantum numbers we obtain

$$g_J = g_L\frac{J(J+1) + L(L+1) - S(S+1)}{2J(J+1)} + g_S\frac{J(J+1) + S(S+1) - L(L+1)}{2J(J+1)} \qquad \text{II. (56)}$$

g_J is called either as the electronic g factor or Landé g factor. For $g_L - 1$ and $g_S \approx -2$

$$g_J = -1 - \frac{J(J+1) + S(S+1) - L(L+1)}{2J(J+1)} \qquad \text{II. (57)}$$

which was already given in the Equation I.(17). Now the total Hamiltonian of an atom in the external magnetic field can be written as

$$\mathcal{H}_{per} = ha\,\vec{I} \cdot \vec{J} - \mu_B\, g_J\, \vec{J} \cdot \vec{H} - \mu_B\, g_I\, \vec{I} \cdot \vec{H} \qquad \text{II. (58)}$$

since the relative coupling energy between $\vec{I}$ and $\vec{J}$ is very small, the last two terms of Equation II. (58) may be regarded as

$$\mathcal{H}_{mag} \approx \mu_B\, g_F\, \vec{F} \cdot \vec{H} \qquad \text{II. (59)}$$

only for very low external magnetic fields. Here

$$\vec{F} = \vec{I} + \vec{J} \qquad \text{II. (60)}$$

Now we shall examine the various cases, i.e., the effects of weak, strong and intermediate external magnetic fields on the atomic system.

i) <u>Weak External Magnetic Field.</u>

In this case, the energy eigenvalues of the Equation II. (58)

are determined by $|F\ m_F>$ representation, since $\vec{I}$ and $\vec{J}$ form a definite total atomic angular momentum $\vec{F}$ which precess about the direction of the external magnetic field. The coupling of the nuclear angular momentum $\vec{I}$ and orbital angular momentum $\vec{J}$ in the weak magnetic field is shown in Fig.II.3a. The energy for the state specified by the quantum numbers F and m_F is given by

$$W\left(F,\ m_F\right) = \langle F,\ m_F | \mathcal{H}_{per} | F,\ m_F \rangle \quad . \qquad \text{II. (61)}$$

It can be re-written as

$$\mathcal{H}_{per} = ha\ \vec{I} \cdot \vec{J} - \mu_B g_J \vec{J} \cdot \frac{\vec{F}}{|\vec{F}|} \frac{\vec{F}}{|\vec{F}|} \cdot \vec{H}$$

$$- \mu_B g_I\ \vec{I} \cdot \frac{\vec{F}}{|\vec{F}|} \frac{\vec{F}}{|\vec{F}|} \cdot \vec{H} \qquad \text{II. (62)}$$

where $\vec{J} \cdot \frac{\vec{F}}{|\vec{F}|}$ represents the projection of $\vec{J}$ in the direction of $\vec{F}$, $\vec{I} \cdot \frac{\vec{F}}{|\vec{F}|}$ represents the projection of $\vec{I}$ in the direction of $\vec{F}$. The components of $\vec{I}$ and $\vec{J}$ perpendicular to $\vec{F}$ average to zero. By using the Equation II. (60) in various forms we obtain

$$\vec{I} \cdot \vec{J} = \frac{1}{2}\left[\vec{F}^2 - \vec{I}^2 - \vec{J}^2\right] \qquad \text{II. (63a)}$$

$$\vec{J} \cdot \vec{F} = \frac{1}{2}\left[\vec{F}^2 + \vec{J}^2 - \vec{I}^2\right] \qquad \text{II. (63b)}$$

$$\vec{I} \cdot \vec{F} = \frac{1}{2}\left[\vec{F}^2 + \vec{I}^2 - \vec{J}^2\right] \qquad \text{II. (63c)}$$

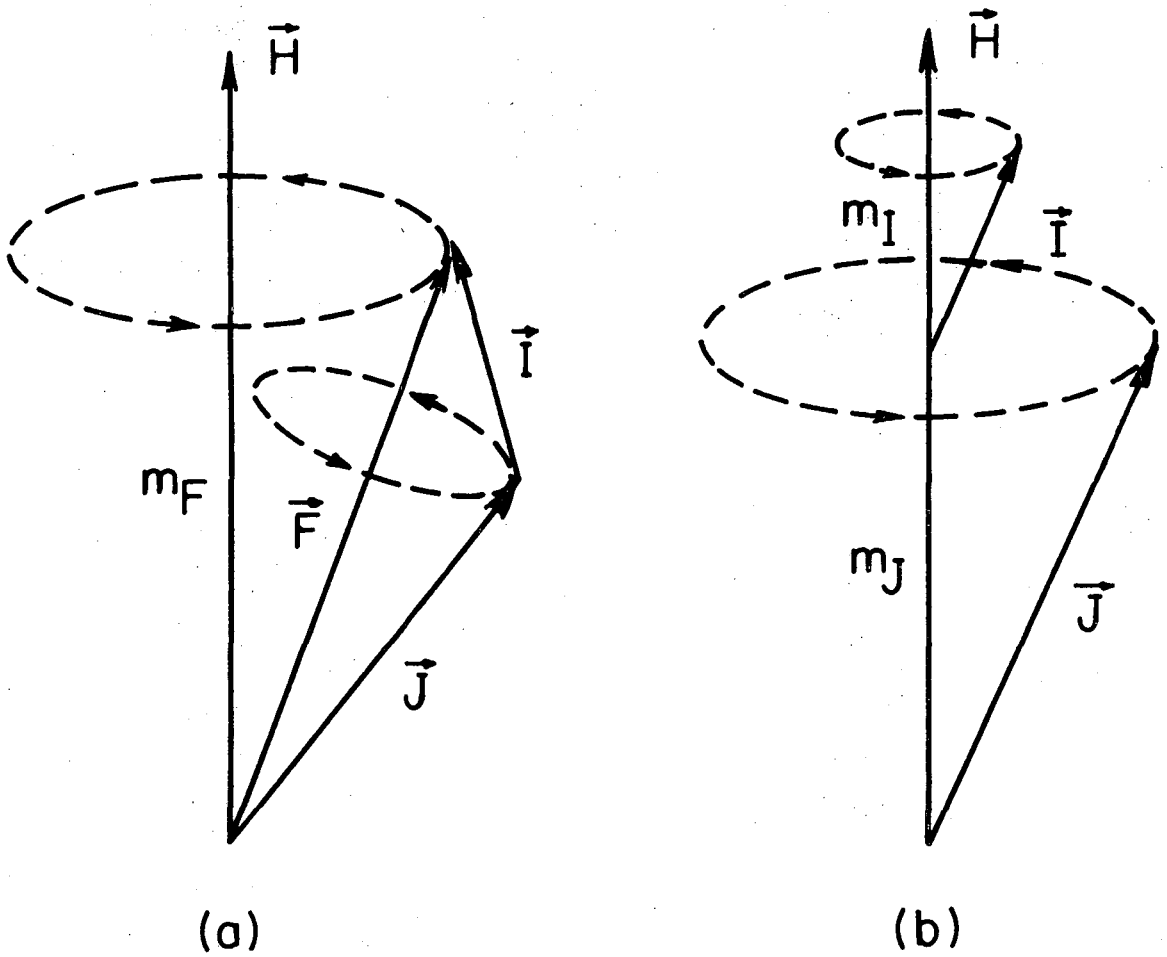

XBL748-3945

Fig. II. 3. Vector diagrams of the precession of $\vec{I}$, $\vec{J}$ and $\vec{F}$ about a) a weak and b) a strong external magnetic field $\vec{H}$.

Therefore, the energy corresponding to the Hamiltonian given in Equation II. (62) is

$$W\ (F,\ m_F) = \frac{ha}{2}\left[F(F+1)\ -\ I(I+1)\ -\ J(J+1)\right]\ -\ \mu_B g_F m_F H \qquad \text{II. (64)}$$

where

$$g_F = g_J \frac{F(F+1)\ +\ J(J+1)\ -\ I(I+1)}{2F(F+1)} + g_I \frac{F(F+1)\ +\ (I+1)\ -\ J(J+1)}{2F(F+1)} \qquad \text{II. (65)}$$

and m_F is the magnetic quantum number for $\vec{F}$.

ii) <u>Strong External Magnetic Field.</u>

In the strong external magnetic field, $\vec{I}$ and $\vec{J}$ separately precess about the direction of the magnetic field. (See Fig. II.3b) Hence, they can not define a constant $\vec{F}$. However, if $\vec{H}$ is in the z direction, $F_z = I_z + J_z$. Therefore, F is not a good quantum number. Instead, now the magnetic quantum numbers m_I and m_J of $\vec{I}$ and $\vec{J}$ are good quantum numbers. Therefore, in $|m_I\ m_J\rangle$ representation

$$W\ (m_I, m_J) = \langle m_I\ m_J | \mathcal{H}_{per} | m_I\ m_J \rangle \qquad \text{II. (66)}$$

$$W\ (m_I, m_J) = ha \langle m_J m_J | \vec{I}_x \vec{J}_x + \vec{I}_y \vec{J}_y + \vec{I}_z \vec{J}_z | m_I, m_J \rangle\ -$$

$$\mu_B g_J H m_J\ -\ \mu_B g_I H m_I \qquad \text{II. (67)}$$

and finally

$$W\left(m_I, m_J\right) = ha\ m_I m_J - \mu_B g_J\ H\ m_J - \mu_B g_I\ H\ m_I \qquad \text{II. (68)}$$

because the diagonal elements of I_x and I_y are zero.

iii) Intermediate External Magnetic Field.

When a selection of proper representation in which the largest matrix elements are diagonal is possible, the standard perturbation calculation can be used in order to make corrections for the effect of small non-diagonal elements. However, often the non-diagonal elements are comparable to the diagonal matrix elements. Then the energy levels of the system are obtained by a solution of the secular equation. The result is the well-known Breit-Rabi equation[34, 35] for J = 1/2 but arbitrary I.

$$W\left(F, m_F\right) = -\frac{\Delta W}{2(2I+1)} - g_I\ m_F\ \mu_B\ H \pm \frac{\Delta W}{2}\left(1 + \frac{4m_F}{2I+1}X + X^2\right)^{1/2} \qquad \text{II. (69)}$$

where

$$\Delta W = h\ \Delta\nu = \frac{ha}{2}\ (2I + 1) \qquad \text{II. (70)}$$

and

$$X = (g_I - g_J)\ \frac{\mu_B}{h}\ \frac{H}{\Delta\nu} \qquad \text{II. (71)}$$

The plus sign (+) is for $F = I + 1/2$ and the minus sign (-) is for $F = I - 1/2$.

The general references for the theory of atomic interactions are the books Molecular Beams[46] and Nuclear Moments[30] by Ramsey, The Theory of Atomic Spectra[29] by Condon and Shortley, Nuclear Moments[37] by Kopfermann, Quantum Mechanics[38] by Schiff. Chan[39] also gives a very systematic discussion of the theory involved in the molecular beam measurements.

Theory Pertinent to the Experiment. Since our main isotope O^{16} and calibration isotope He^4 have no nuclear magnetic moment, the equations which apply in our experiment are considerably simplified. For example, the Equation II. (58) for $I = 0$ now reduces to

$$\mathcal{H}_{per} = - \mu_B \, g_J \, \vec{J} \cdot \vec{H} \qquad \text{II. (72)}$$

It is clear from Equation II. (65) that $g_F = g_J$ and if we substitute $L = 0$ into the Equation II. (54) we have $g_J \approx -2$. For this case any one of the two representations would yield the energy

$$W = - \mu_B \, g_J \, H \, m_J \qquad \text{II. (73)}$$

or the energy difference between the levels

$$\Delta W = - \mu_B \, g_J \, H \, \Delta m_J \qquad \text{II. (74)}$$

The applied r.f. provides the energy for the transition with $\Delta m_J = \pm 1$.

$$\Delta W = h\nu \qquad \text{II. (75)}$$

Therefore

$$g_J = -\frac{h\nu}{\mu_B H} \qquad \text{II. (76)}$$

The frequency ν and magnetic field H are measured to determine the electronic g_J factor. However, if one uses a calibration isotope with a known g_J factor of good precision, a comparison of the resonance "transition" frequencies yields the unknown g_J factor of the isotope in question. In our experiment the resonance frequency of $(3p^3\ 3s)\ {}^5S_2$, metastable state of oxygen was compared with the resonance frequency of (1s 2s), ${}^3S_1$ metastable state of helium to obtain the g_J factor of the former.

$$g_J({}^5S_2,\ O^{16}) = g_J({}^3S_1,\ He^4)\ \frac{\nu(O^{16})}{\nu(He^4)} \qquad \text{II. (77)}$$

The schematic Breit-Rabi diagrams of both of the isotopes are shown in Fig. II. 4.

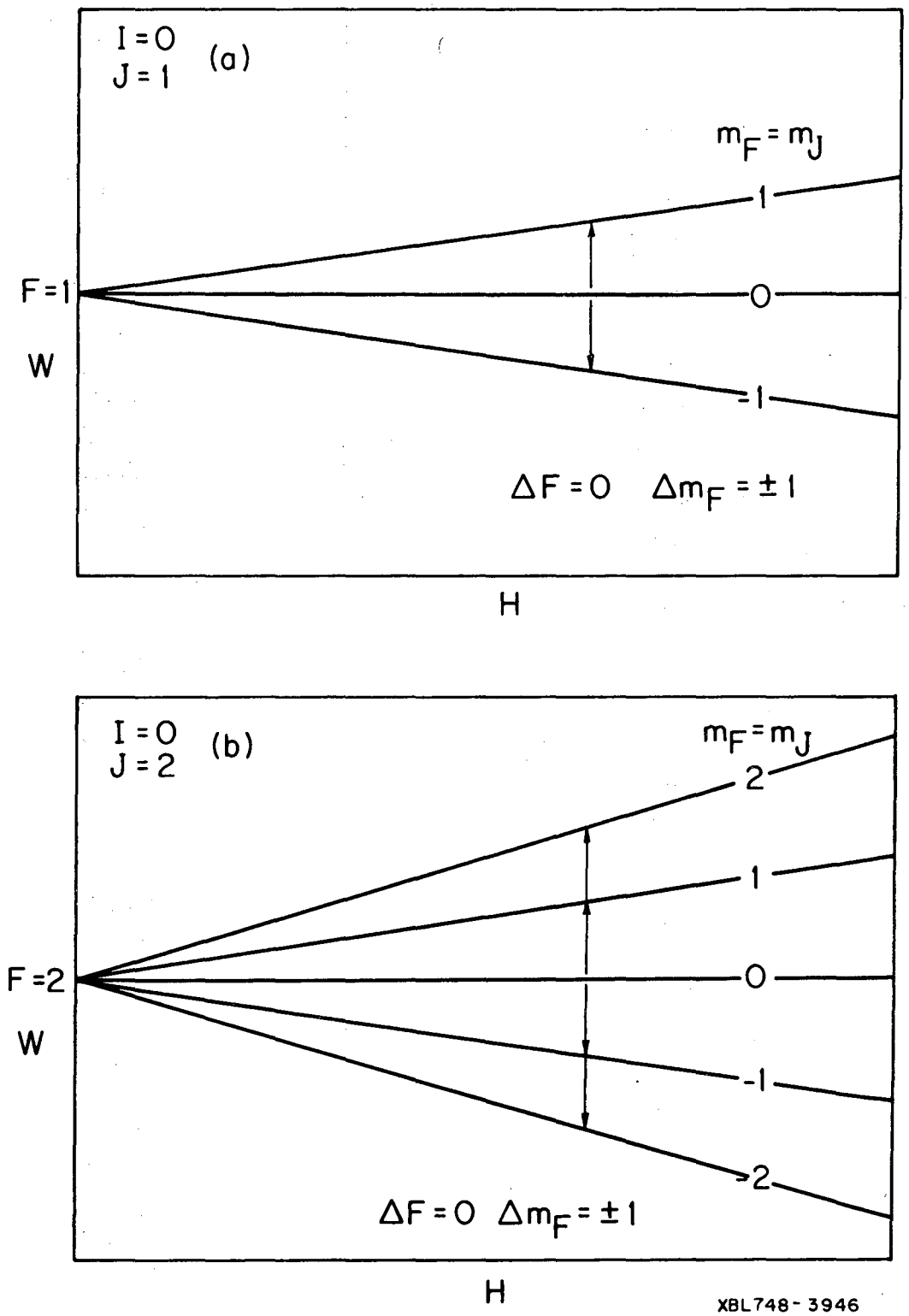

Fig. II. 4. The Breit-Rabi diagram of a) $^3S_1$ metastable state of helium and b) $^5S_2$ metastable state of atomic oxygen. The transitions are indicated by arrows.

B. Apparatus and Experiment

The flop-in technique was first employed by Zacharias.[40] The main elements of the flop-in type atomic beam machine have been explained in the literature. In addition to the monograph written by Ramsey,[36] the review article by Kusch and Hughes[41] gives a full description of the apparatus. Nierenberg,[42] Marrus and Nierenberg,[43] and Şaplakoğlu[44] also outline the flop-in experimental technique that has been used in the measurement of various atomic and nuclear quantities.

The beam machine used in this experiment is the same one which served as the Stern-Gerlach time-of-flight analyzer in our previous work on atomic nitrogen. However, except for the magnets, the detector and the gas feeding system, we have made several modifications and the method and experimental procedures were completely new and different. Therefore, here we aim to explain the design modifications, apparatus, and experimental methods which are not already discussed in the first chapter.

The Gas Feed System. The schematic diagram of the gas feed system was given in Fig. I. 5. All plastic tubing in the system was replaced by the clean copper tubing during the last phases of the previous experiment. Therefore, we kept the main body of the gas feeding system as it was. However, a high purity oxygen tank was

connected in place of nitrogen, and a helium tank provided the He gas which was used as the comparison isotope. We found it unnecessary to clean the gas by feeding through a getter and to cool the gas with liquid nitrogen before it entered into the discharge source.

Source. The source was a U-shaped Pyrex tube (Fig. II. 5) powered by a 500 w, $\approx$ 50 MHz radio-frequency power supply. A tank circuit with a one-inch diameter, 5-turn coil of 1/8" copper wire and a parallel connected adjustable condenser was attached between the two electrodes of the discharge tube in order to draw the optimum power for the discharge to be maximum. The slit from which the beam emerges was 5 mils wide and 160 mils high. The whole assembly of the discharge tube could slide sideways, back and forth, to align the beam perfectly. The line or source pressures were about 0.4 torr for oxygen and 0.2 torr for helium. Actually, the oxygen discharge in the tube at low pressure did not give enough of the $^5S_2$ metastable states, until we increased the line pressure to the mentioned value. Then a unique discharge was developed between the source slit and the buffer slit of the machine, producing the states with very high efficiency. Yet, the production rate varied in time, perhaps due to the instabilities of the r.f. power sources and oxidation of the electrodes of the discharge tube. But we were able to control the signal level by rearranging the frequency, power and gas pressure.

The procedure of obtaining the r.f. discharge and optimizing the yield was the following: First, the line was pumped down to about

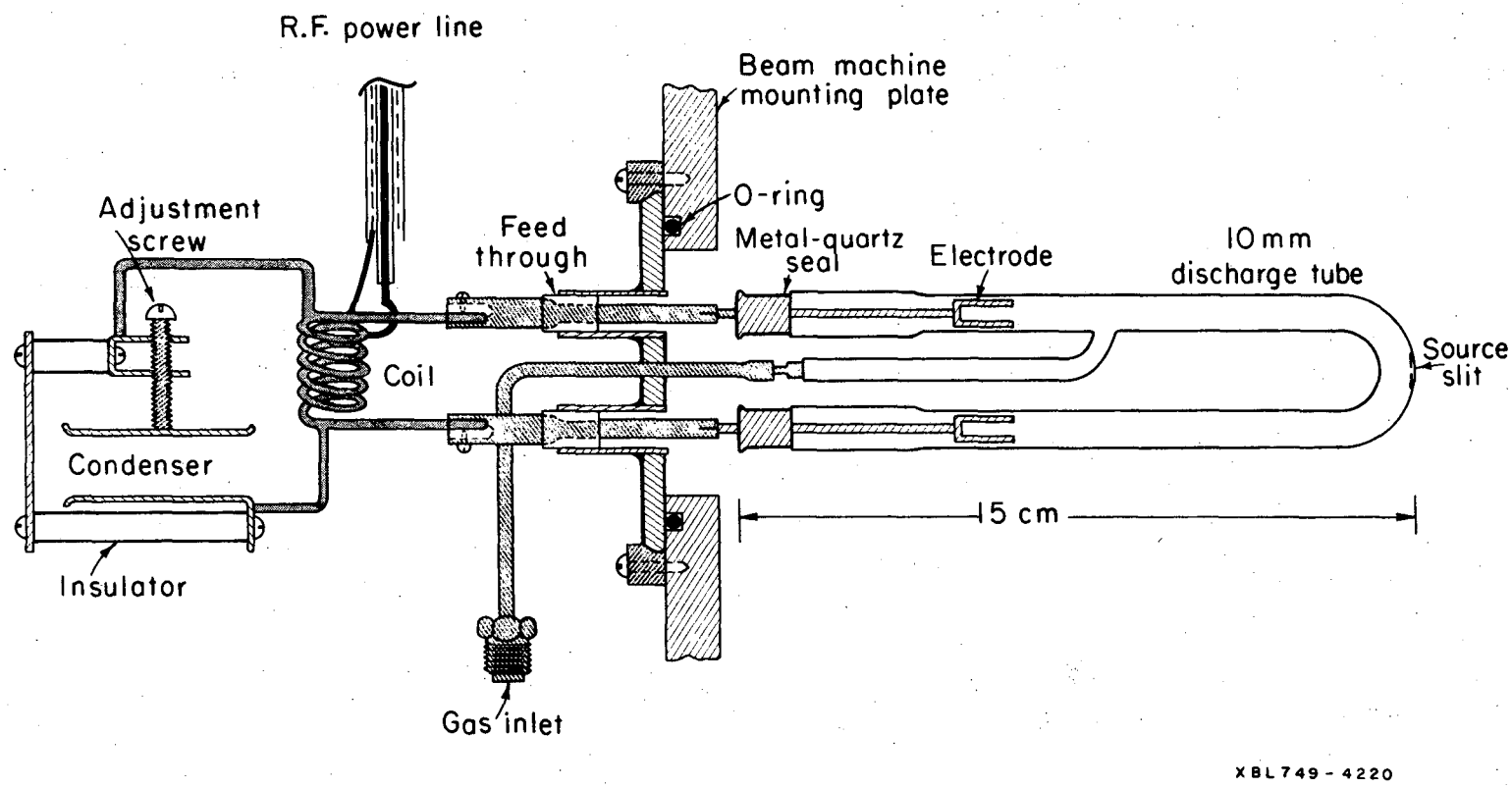

Fig. II. 5. The r.f. discharge source.

10 microns Hg. After the r.f. power was supplied to the tube, the oxygen pressure was increased slowly by turning the variable leak valve while the source valve was kept wide open. Usually a very faint bluish discharge developed at low pressure and got stronger with increasing pressure. When the variable leak valve read about 155, the discharge jumped out of the tube and expanded into the whole source chamber. Sometimes we had to close the valve of the diffusion pump connected to the source chamber to accomplish this situation. Later the pressure was reduced by the variable leak valve to about 152, at which the discharge was localized as a glow between the source slit of the tube and the fore slit which is about 1 inch from the former. Then the frequency and power of r.f. was adjusted very carefully to give the brightest so-called frontal discharge. The counts in the matastable ^5S region thus reached its maximum value. However, helium discharge with the same setting of r.f. source was straight forward, at lower pressure, and completely in the quartz tube.

With these optimum settings, all the magnets operating, and detector at the center with a 25 mils stop on the beam line, the total oxygen count was 4000-6000 per second and increased at most by about 400 per second during the resonance. Total helium counts were 1600-2300 per second, increased by a maximum of 1000 counts per second during the resonance. The superiority of the discharge source over the electron bombardment source is very remarkable here because oxygen would corrode the filament of the electron gun, causing frequent interruptions of the experiment to replace the filament. We

do not have direct measurements of the efficiency of the discharge source in producing the $^5S_2$ states of oxygen and the $^3S_1$ state of helium. Being satisfied with a very good signal-to-background ratio of about 7/1 in both of the isotopes during the resonance, we did not measure the direct efficiency since it required a detector which is sensitive to all kinds of particles present in the beam including ground states of the atomic oxygen and oxygen molecules.

However, another discharge source -- the electrodeless Brink discharge source[45] -- was tried during the preparation period of this experiment. The ratio of the counts in the $^5S_2$ region of the spectrum to the total counts in the 64 channels, each channel corresponding to 13.3 μsec, was about 0.001. Certainly, this ratio depends on several variables, such as pressure, r.f. power, frequency, purity of the gas, design of the source. Bell and Kwong[46] investigated the dissociation of oxygen in a radio frequency discharge and obtained experimental curves for the yield of atomic oxygen as functions of power, pressure and gas flow rate. But, unfortunately, the ratio of the ^5S states in the atomic oxygen was not known.

The source in our experiment was operated in the pulsed mode. The r.f. power was applied for 40 μsec, followed by a 6.4 msec interval with no r.f. and again r.f. for 40 μsec. Therefore, the discharge products were released in packets or bursts from the source, but, due to their masses, kinetic energies, and velocity distributions, they arrived at the detector in different times. It was calculated

and observed that practically nothing was left over beyond the 6.4 msec interval, so that the particles from successive bursts were isolated to avoid any misleading results.

The r.f. was provided by a master oscillator which is fed by a 2.5 kV, 500 ma power supply (Fig. II. 6). A modulator was connected to the master oscillator, but it was operated in the continuous wave mode. The duration of the r.f. pulses and the interval between them was controlled by a remote 5v power supply which used 1 MHz standard signal as the time reference. When + 5v was applied, the r.f. power was on, but 0v turned the r.f. power to zero by means of a simple electronic switch. The duration and the interval could be adjusted by means of 24 switches on the binary control panel of the dividers. We will mention again about the r.f. pulsing when we explain the data-collection system as a whole.

Detector and Geometry. The detector was a cold tungsten surface film of about 0.6 x 0.8 inches followed by a continuous semi-conductor dynode faced by another dynode surface with a length of about 1.5 inches. The spacing between the two dynodes is about 200 mils. A mesh of very fine wire is attached to the second dynode and it is in front of the detector surface. Small permanent bar magnets provide the deflecting magnetic field to the knocked-off electrons. At the end of the dynode surfaces, electrons are collected by an electrode and this signal is amplified in two "high-rate, linear amplifiers" before it reaches the counter and the computer. The detector is a compact unit with the dynodes and permenent magnets,

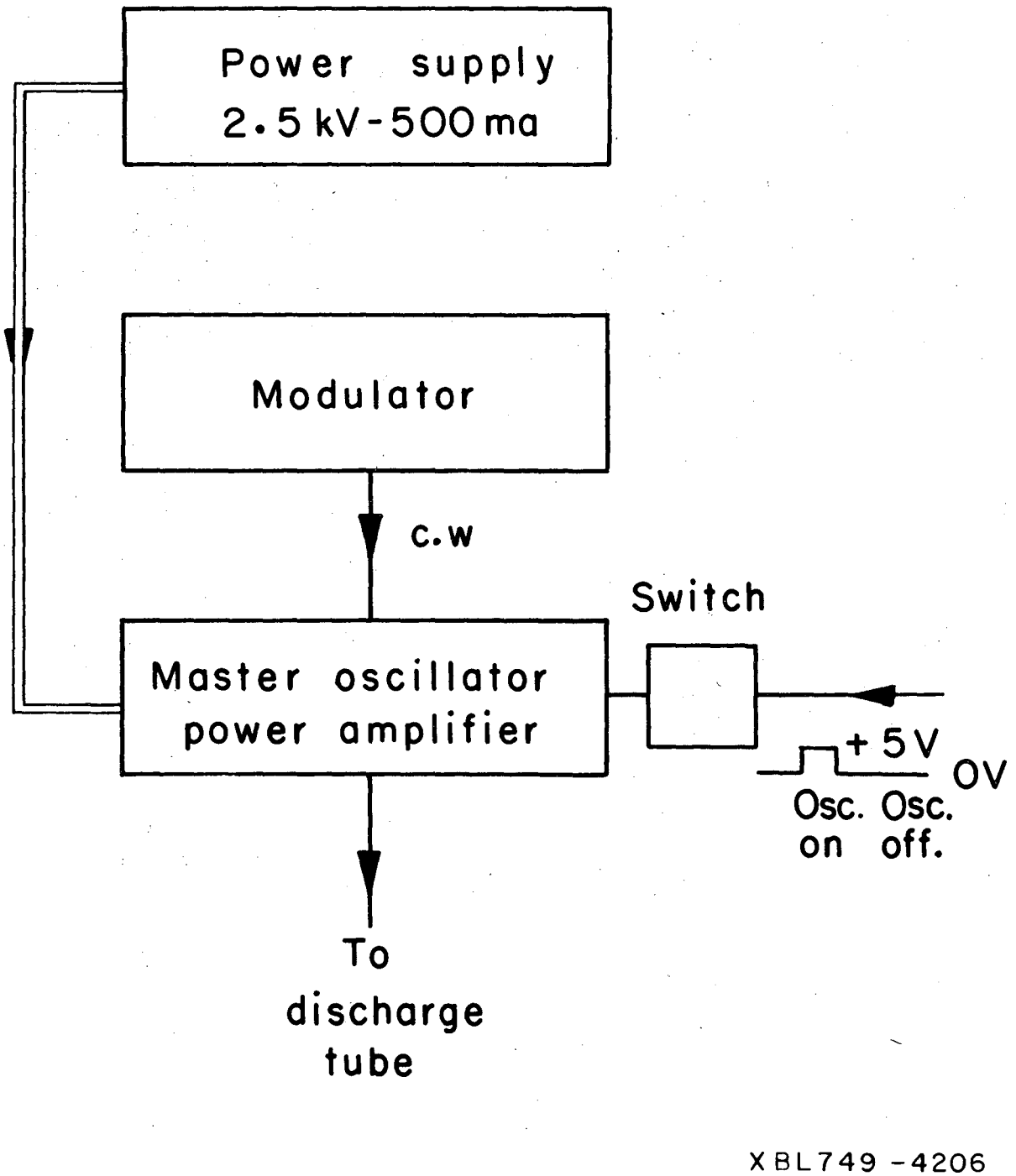

Fig. II. 6. R. F. power system for the source.

and called "magnetic electron multiplier" or simply MEM. We placed a 25 mil diameter wire vertically in front of the detector surface right in the middle and about 0.5 inches from the mesh. This wire served as a stop for the undeflected elements of the beam. The whole detector and multiplier assembly could be moved in the vacuum perpendicular to the beam direction. Since we used another metastable state -- $^3S_1$ of He -- for the field calibration, we utilized only one detector. Therefore, the size of the stop wire was optimized for both of the states involved. A schematic drawing of the detector assembly is given in Fig. II. 7 . It shows the top view of the system, the south poles of the magnets are inside the page.

One of the unique features of this experiment is the beam geometry. In the conventional flop-in technique the atoms, which are undergoing a certain transition, are deflected into the detector through a narrow slit placed in front of the detector at the center. As it is seen from the Fig. II 4, $^3S_1$ metastable state of helium has three Zeeman levels with $m_J = \pm 1, 0$ and $^5S_2$ metastable of atomic oxygen has five Zeeman levels with $m_J = \pm 2, \pm 1, 0$. Both have $I = 0$. This similarity of the Zeeman diagrams of the two species allowed us to use the same geometry for both of them. Besides being able to use the same detector and the counting system for both of the species, this geometry is advantageous in avoiding some systematic errors because of the similar trajectories in the machine. Thus some of the experimental conditions which affect the measurement are the same for the states $^3S_1$ of He and $^5S_2$ of oxygen.

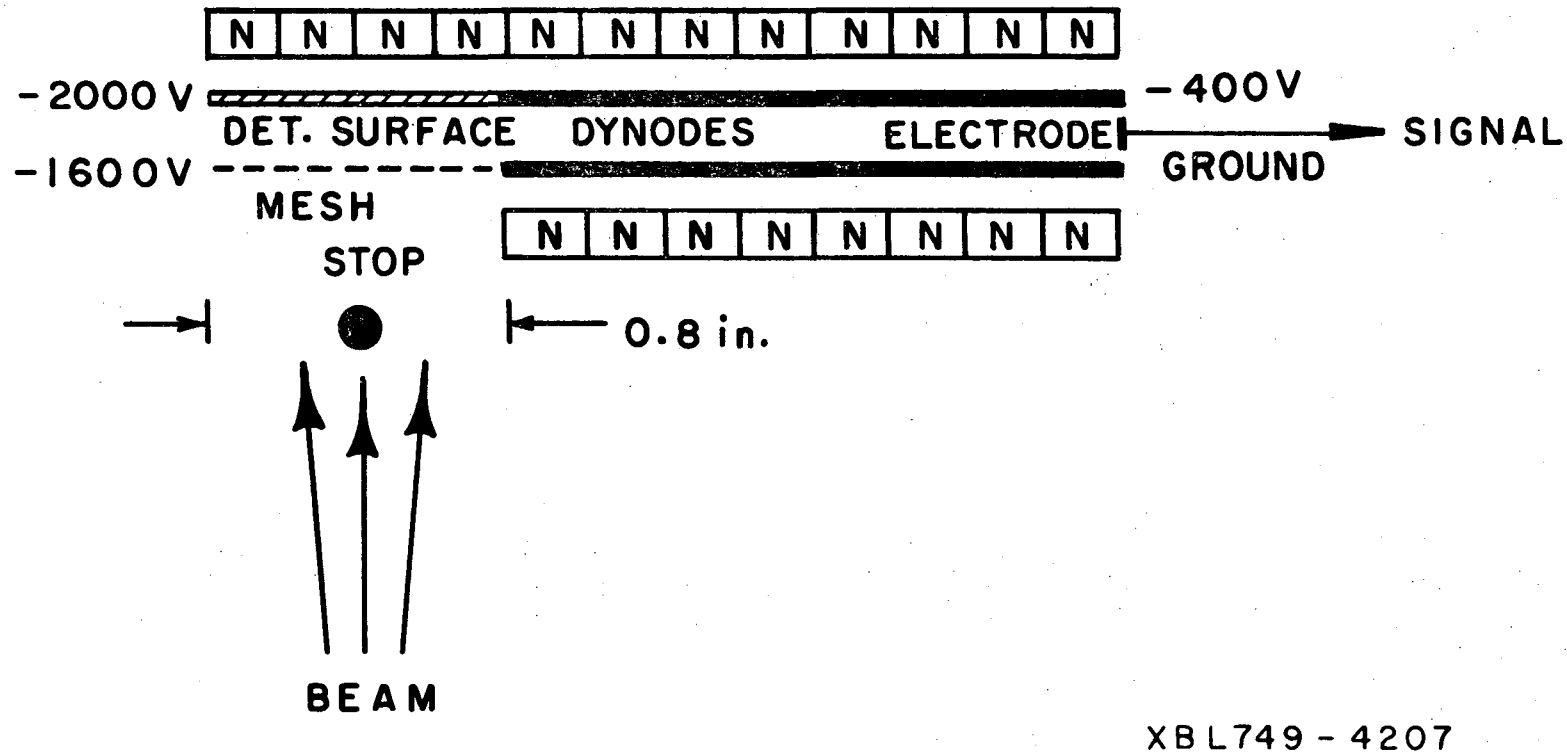

Fig. II. 7. Detector and electron multiplier assembly.

The beam emerging from the source enters into the A chamber through a 0.020 inch wide fore-slit. The A magnet has been operated at its maximum deflecting power (I_A = 5.0 amps). Considering the $^5S_2$ state of oxygen for now, the beam splits into five different trajectories according to the atomic magnetic quantum number m_J. While the collimator slit, placed at the center of A magnet, collimates the part of the beam with $m_J = 0$ to the second collimator, the rest of the beam with $m_J = \pm 2, \pm 1$ is deflected toward the sides of the magnets and pumped away from the machine. The second collimator, directly in front of B magnet, allows only the species with $m_J = 0$ originally to pass through. The beam consists of atoms with $m_J' = 0$, ± 1 and ± 2. The atoms with $m_J' = 0$ remain from the original beam. The atoms with $m_J' = \pm 1$ and fewer with $m_J' = \pm 2$ are due to the transitions that take place in the hairpin. (See Fig. II. 4b). Between the pole pieces of the B magnet, this beam splits into specific trajectories, defined by the velocity, mass, magnetic quantum number m_J' of the species and the gradient of the magnetic field. The diameter of the stop wire allows almost all of the atoms which have a non-zero m_J' to hit the detector surface. But the direct beam is very efficiently stopped by this obstacle. Thus a transition is indicated by an increase in the counts. The trajectories which are shown in Fig. II. 8 represent the $^5S_2$ state of oxygen. However, the trajectories of the calibration isotope ($^3S_1$, He) would be schematically similar except the parts of the beam with $m_J = m_J' = \pm 2$. (See Fig. II. 4a)

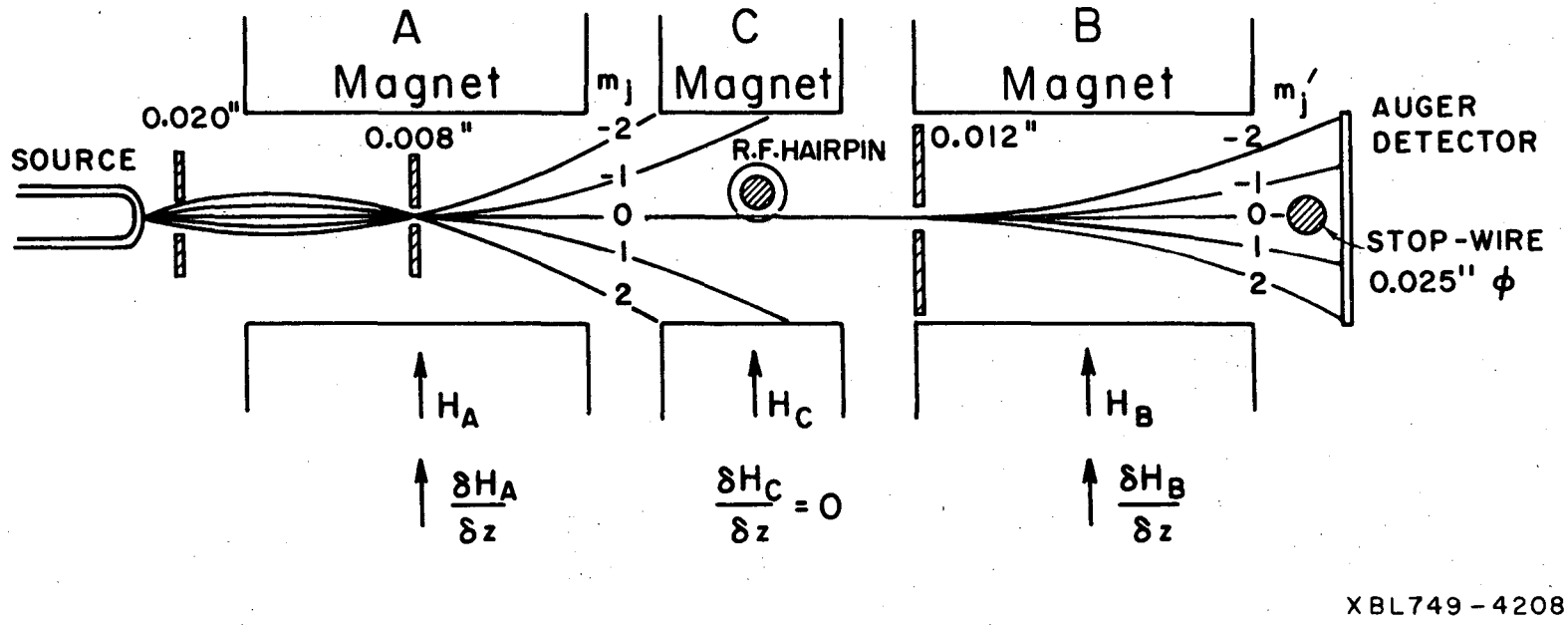

Fig. II. 8. Magnetic field configuration and the geometry of the oxygen experiment.

The features of this new flop-in geometry can be summarized as: a) Both species have the same trajectories through the radio-frequency transition region. b) One can observe the flop-in resonance with low background. c) The single quantum resonances are observed in integral J states. d) It allows the detection of the species with greatly differing deflection properties.

Metastable States of Oxygen and Helium. Usually when an atom is excited to a higher energy level, a dipole transition takes place if there is a lower state that can be reached without violating the selection rules. Since the change of state is allowed by the selection rules, the transition probability is quite large, so the lifetime of an excited state is about 10^{-8} seconds or even less.[47] But, in the case where no lower state can be reached by an allowed dipole transition, the de-excitation will occur after a longer time by some higher order transitions or collisions. A state of an atom which has a lifetime considerably longer than 10^{-8} sec. is called a metastable state. As a matter of fact, this concept was first introduced for the ^1S and ^3S states of helium.[48] Another example is the ^5S state of oxygen.

The ground configuration of the oxygen atom is $1s^2 2s^2 2p^4$. This configuration gives the $^3P_2$ ground state and $^1D_2$, $^1S_0$ metastable states with the lifetimes of about 150 and 15 seconds, respectively.[49] The energies of these two states are, respectively, 1.97 ev and 4.18 ev above the ground state. Because of their relatively low energies, even if they exist in the beam and are able to reach the detector, these metastable states cannot initiate the Auger process. The next

excited state with the configuration $2s^2\ 2p^3\ 3s$ is the $^5S_2^o$ state.[7] The superscript "o" indicates that this state has an odd number of p electrons. Usually we do not carry this superscript in the state notation. $^5S_2$ state is known to be metastable, and it lies 9.14 ev above the ground state. It is the lowest quintet state of atomic oxygen. Principally it could decay to the ground state through the spin-orbit interaction with the slightly lower $2p^3\ 3s$, $^3P_2$, ^1P and D states. But, theoretically, the main contribution to the lifetime comes from the transition through 3s, $^3P_2$ state. The lifetime of the $^5S_2$ state, calculated by Garstand was about 700 μsec.[50] The measurements were carried out by Wells and Zipf[10] and independently by Johnson[51] in 1972. Although their experimental results (189 ± 50 μsec, and 185 ± 10 μsec, respectively) are almost 1/3 of the previously calculated lifetime, they agree very well with the results of a recent many-electron calculation, reported as 192 μsec, by Nicolaides.[10] Another more careful measurement by Wells and Zipf[52] determined the lifetime of the $^5S_2$ metastable state of oxygen as 170 ± 25 μsec. In all of the experiments the time-of-flight technique was employed.

This quite short lifetime is a limitation for the experimenter when measuring the g_J factor by the atomic beam magnetic resonance method. Taking the Equation I. (1) into consideration, the deflection of an atom in an inhomogeneous field is proportional to the square of the time it spends in the field. In other words, in order to have larger deflections the atoms must travel slower in the machine. But, slower metastable atoms would decay more before they reach the

detector. In our experiment, the metastable $^5S_2$ oxygen atoms traverse the machine in about 350 μsec. Therefore, only those atoms which live longer than the transit time are observed. This would be approximately 13% of the metastable $^5S_2$ atoms that started from the source toward the detector if there were no deflection and obstacle in the machine. Considering the geometry, this percentage is reduced to about 0.8% and further reduced by the transition probability which is certainly less than 100%. However, as we shall give the actual figures later, the number of metastable atoms in our resonance peaks were very satisfactory. It is quite true that in such an experiment, the efficiency of the source plays an important role, since a high signal-to-background ratio is necessary in order to determine the g_J factor with precision. The other precaution is to reduce the background.

The process in which the $^5S_2$ states are produced can be formulated as

$$e + O_2 \rightarrow O(^5S_2) + O + e \qquad \text{II. (78)}$$

The ground state oxygen molecule can be excited into a higher molecular level by electron bombardment during the discharge. The new level may be any of the levels shown in the Fig. II. 9. If it is in the proper level it dissociates directly into one $^5S_2$ metastable atom and one ^3P ground state atom. But, $^5S_2$ atoms may also

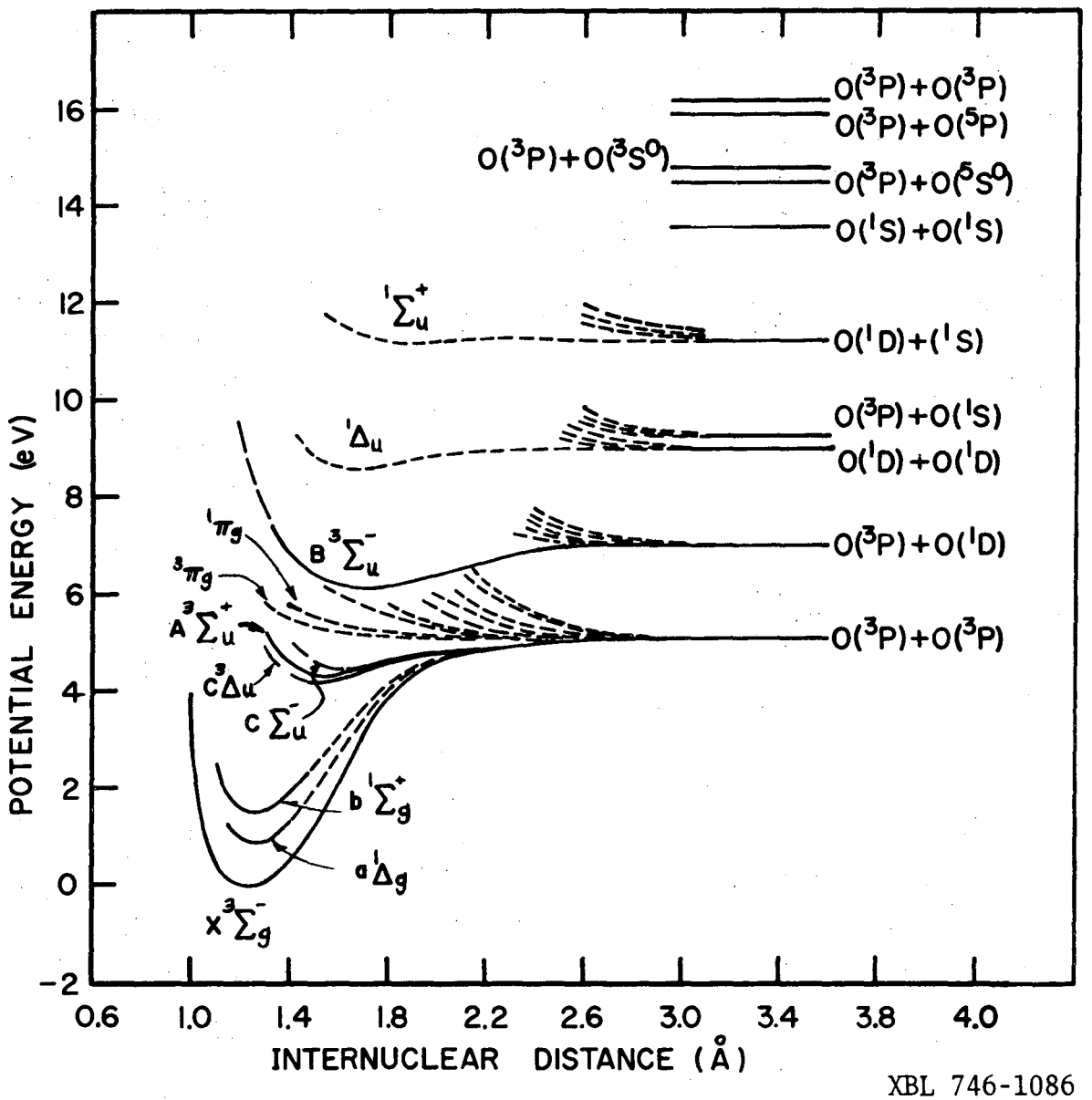

Fig. II. 9. Potential energy curves for an oxygen molecule. Dissociation fragments are shown on the right side of the diagram.

be produced by cascade from higher lying atomic quintet states which result in the dissociation of the high molecular levels[53] in the beam obtained by an r.f. discharge. Along with the $^5S_2$ states, ground state atoms, low energy metastable atoms, metastable molecules, ground state molecules, electrons and photons may be present. The Auger detector is not sensitive to the ground state atoms, molecules and low-energy metastable atoms. Ions and electrons would be trapped in the magnetic fields throughout the machine. Metastable molecules move very slowly compared with the $^5S_2$ atoms so they can be spread out easily in the time-of-flight spectrum. We believe most of the photons hit the stop-wire and, therefore, cannot reach the detector. The photons which are scattered into the detector, however, are synchronous with the discharge excitation pulse, so that they only occupy the first few channels of the time-of-flight distribution.

Since the metastable states of our calibration isotope -- helium -- are mentioned elsewhere,[54] we shall not discuss it here in detail. The two electron spins s = 1/2 of helium can combine in four different ways. One of these combinations yields singlet spin states (para-helium) and three yield triplet spin states (ortho-helium). The lowest metastable singlet state is 2^1S which is 20.6 ev above the ground state 1^1S. The lifetime of this state was measured by Van Dyck, Johnson and Shugart as 19.7 ± 1.0 milliseconds.[55] The lowest state of ortho-helium is 2 ^3S state which is 19.8 ev above the ground state. This state decays to 1 ^1S ground state with a decay rate of 1.27×10^{-4} sec^{-1}.[56] The reciprocal of the decay rate gives the lifetime as about

8000 seconds. The experimental determinations yielded about half of the theoretical value.[57] But the uncertainty was as large as the factor of 3. However, this sufficiently long lifetime together with the similarity between the Zeeman levels of $^3S_1$ state of helium (see Fig. II. 4) with that of $^5S_2$ of oxygen and the good precision of the recent measurement[25] of its g_J factor were considered favorable when selecting it as the calibration state.

Data Collection System. The source and the detector units of the data collection system were explained in the previous sections. A general discription of the pulsed beam counting scheme was also given in Chapter I while we discussed the time-of-flight method for the nitrogen experiment. Basically, the same method of counting was utilized in addition to the atomic beam magnetic resonance technique throughout the oxygen experiment. This data collection scheme, we believe, has not been applied in any resonance study previous to this experiment. By using this highly sophisticated system, we could isolate ^5S and ^3S atoms from the other discharge products. Therefore, it deserves a detailed discussion. Although it is not explicitly shown in the Fig. II. 10, a PDP-11 computer was the center of the data collection system. Simultaneously it controlled the frequency synthesizer to sweep the r.f. frequency within the given limits and steps.

A 1 MHz sine-signal taken from the standard frequency oscillator was converted into square wave pulses by a saturated amplifier. Divider I allows only one pulse to pass through in every 40 pulses.

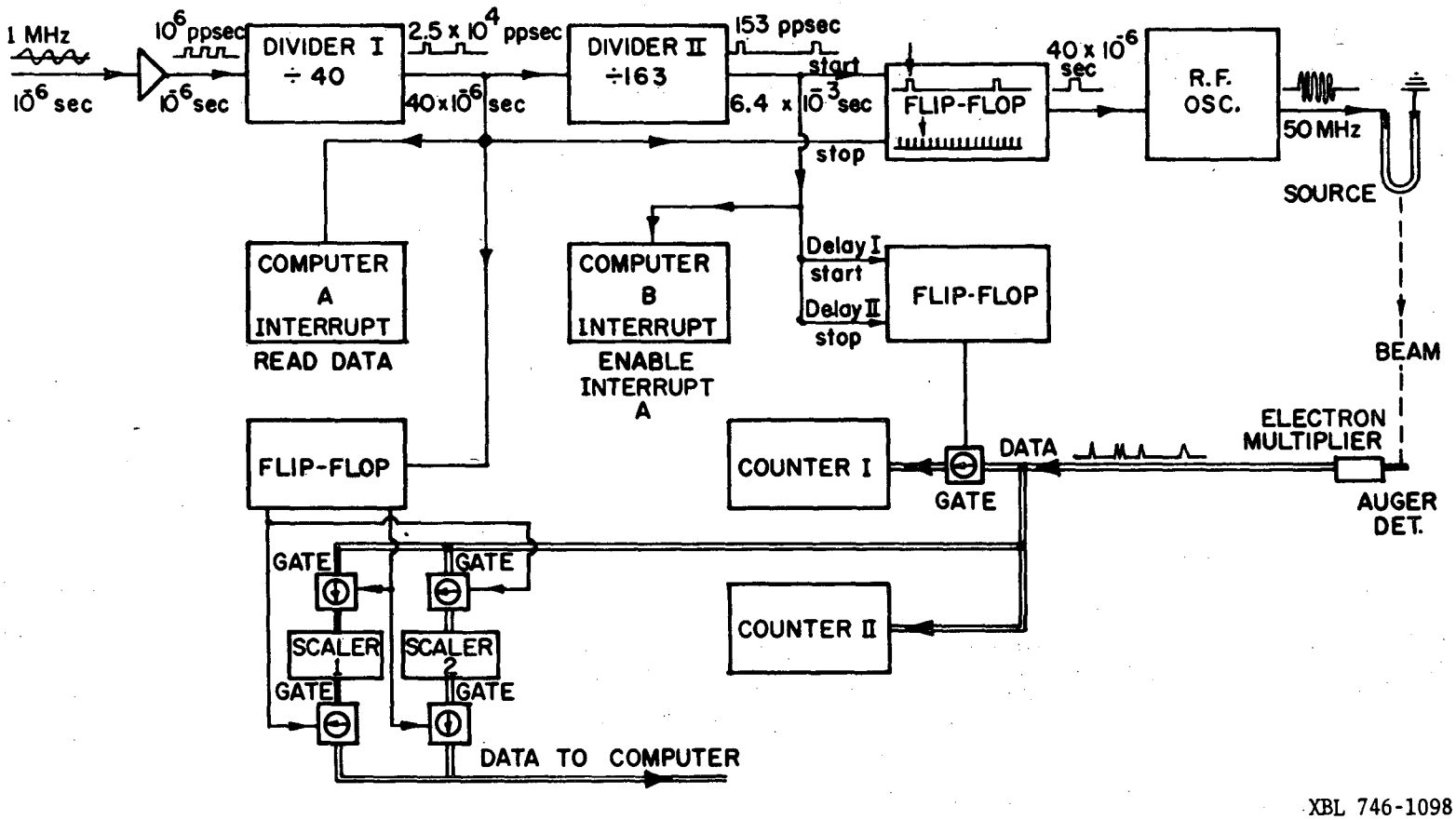

XBL 746-1098

Fig. II. 10. Data collection system.

Thus the time duration between two successive pulses is now 40 μseconds. This determines the duration of the discharge pulse and the time per channel. The numbers given here are the numbers used in the oxygen experiment and can be changed by a series of switches on the Divider I and II to any desired value. Divider II allows one of the 163 pulses which are delivered by Divider I to pass through. The output of Divider II then has 153 pulses per second which is the repetition rate of the discharge pulses. The flip-flop governed by the pulses from the Divider I and Divider II sends one of the 40 μsec pulses in every 6.4 millisecond to the r.f. oscillator and switches the r.f. power on and off. The rest of the circuit is for channeling, storing and displaying the data which is received after each discharge pulse. This is done in the following way.

The magnetic electron multiplier is connected into two counters. One of them (Counter II) counts the output of the multiplier all the time. But, Counter I can be set to an interval of time-of-flight spectrum by adjusting the Delay I and Delay II variable resistances. Delay I determines the opening time of the electronic gate between the multiplier and the Counter I by a flip-flop circuit, with respect to the appearance of a pulse in the output of Divider II. Similarly, Delay II determines the closing time of the gate with respect to the same pulse. Only during this interval the data can be registered in Counter I. For the experiment, Counter I was set to the interval between 420 μsec and 2100 μsec after the discharge pulse. As it is seen in the Fig. II. 10, the data is also fed to the computer through

two pairs of gates and two scalers. The start-command pulse for the discharge from the Divider II simultaneously actuates the Computer B-Interrupt which in turn enables Computer A-Interrupt. However, the A-Interrupt waits to order the computer to take data until the second pulse from the Divider I is received, i.e., the 40 μsec separated pulses from Divider I. At one instant, only one of the upper gates is open, for example, the gate above the Scaler 1. While the data is being stored in the Scaler 1, the lower gate is kept closed. After 40 μsec, the next pulse causes the flip-flop to close the upper gate and to open the lower one. Thus, now the data stored in Scaler 1 is transferred to the computer and stored, let us say, in Channel 1. Meanwhile, the gate above the Scaler 2 being open now allows the data to be stored in Scaler 2, and 40 μsec later, the lower gate allows all the stored data into the computer. This data is stored in Channel 2. The data stored in the memory of the computer is momentarily displayed on an oscilloscope. The process of data storing goes on for 64 channels. The number of channels, the duration of each discharge pulse and channel, are given to the computer in the content of machine language programs. In the oxygen experiment, at the end of 64 channels, the computer goes into a waiting period until a new discharge pulse arrives into the computer B-Interrupt. Then, the process is repeated up to the moment, the experimenter stops data collection by the control button on the panel of the PDP 11. The data collected in this way obviously gives us the time-of-flight spectrum of the discharge products, and can be printed automatically

by a teletype connected to the computer by switching one of the control buttons of the PDP 11 on. The other duty of the teletype is to read the program which is punched on a paper tape.

For the resonance, the time-of-flight distribution can be divided into six groups by depositing the first and last number of channels of each group in the designated addresses. The r.f. frequency is set on the Hewlett-Packard Frequency Synthesizer in the MHz digits. The three digits in the KHz order are fed to the computer manually. The frequency step for the sweeping should also be given. With the program which we have used in the experiment, the synthesizer frequency was made to oscillate from the initial value to the largest value in twenty steps. Thus one sweeping cycle was completed in forty steps. Each step was 2 KHz. While the frequency was shifting back and forth, the behaviours of the species in six different time-of-flight distribution groups could be seen simultaneously on the screen of the oscilloscope. The particles which we were interested in for measurement and calibration were both in the group between the channels 11 and 35. Since the two adjacent groups contained some faster and slower ^5S and ^3S atoms we could also observe a small resonance effect in these groups.

The oscilloscope display could be shifted to resonance or to time-of-flight distribution by two control buttons on PDP 11. Similarly, the teletype would print either the resonance data of any selected group or time-of-flight data by storing certain numbers in a certain address in PDP 11 and switching the data print button on.

In the second half of the experiment, the IBM data cards were punched automatically by a keypunch machine interfaced into the PDP 11. In order to keep it clear, we have not included the computer, the frequency synthesizer, display oscilloscope teletype and IBM keypunch machine in Fig. II. 10. The high-rate linear amplifier and the single-channel annalyzer, which were between the MEM detector and counters, are also not shown.

Field Locking and Homogenizing. The Berkeley (Room 86) Atomic Beam Apparatus has a 12 inch diameter, circular pole pieces, commercial Varian V4012A electromagnet in its C field region, and is driven by a regulated NMR controlled V1200 Varian Magnet Power supply. Although the magnetic field between the pole pieces is homogeneous to about 60 ppm over a distance of 3 inches, three sets of shim coils were placed on the outside of the walls of the C can. By means of these shim coils, the homogeneity could be improved by a factor of 60 or even better for the precision work over slightly narrower regions.

Field stability was achieved by using the Klein-Phelps[58] type nuclear magnetic resonance (NMR) system. Prior to the experiment, we replaced the mercury cell internal voltage reference source of the V1200 magnet power supply. The new, highly stable Zener diode has improved the current regulation further. The Berkeley Klein-Phelps NMR system is explained in detail in the Reference 54. Another NMR system with a movable probe in the C field was used in order to measure the field at various points between the pole pieces. This second system was essentially similar to the first one except it was

frequency modulated. Here we shall discuss briefly the NMR field locking system. (See Fig. II. 11). The whole system operates around the hybrid tee. The 18 MHz NMR frequency is directed into D and C terminals. By adjusting C_1 and C_2, one can provide an impedance match between the cable connected to C and the NMR coil at a certain frequency. In this case, there is no r.f. reflection from the coil. But, if somehow the balance conditions changes as a result of a slight shift in the magnetic field, the NMR r.f. power is reflected back to the hybrid tee. It is amplified and then phase compared with the output of oscillator at the mixer. The modulation oscillator output, fed to the NMR probe field coils, continuously sweeps through the NMR resonance field. Thus a phase comparison of the reflected and amplified signal may cause the lock-in amplifier to provide a correction voltage to the C magnet power supply proportional to the magnitude of the difference from a specific relation between the phases. Fig. II. 12 represents a typical dispersion curve obtained by using the frequency modulated, magnetic-field-measuring NMR system. The modulation frequency is Δf = 800 Hz. Since the magnetic field sweeping was not linear, the units in the frequency axis is arbitrary. But, the larger symmetric dispersion curve corresponds to a frequency difference of 800 Hz around the resonance frequency.

After the magnetic field was locked by NMR system, the chart recorder was set running, until the end of that particular run. Thus, any variation in the magnetic field could be observed momentarily and the data taken with the unlocked field would be eliminated right away.

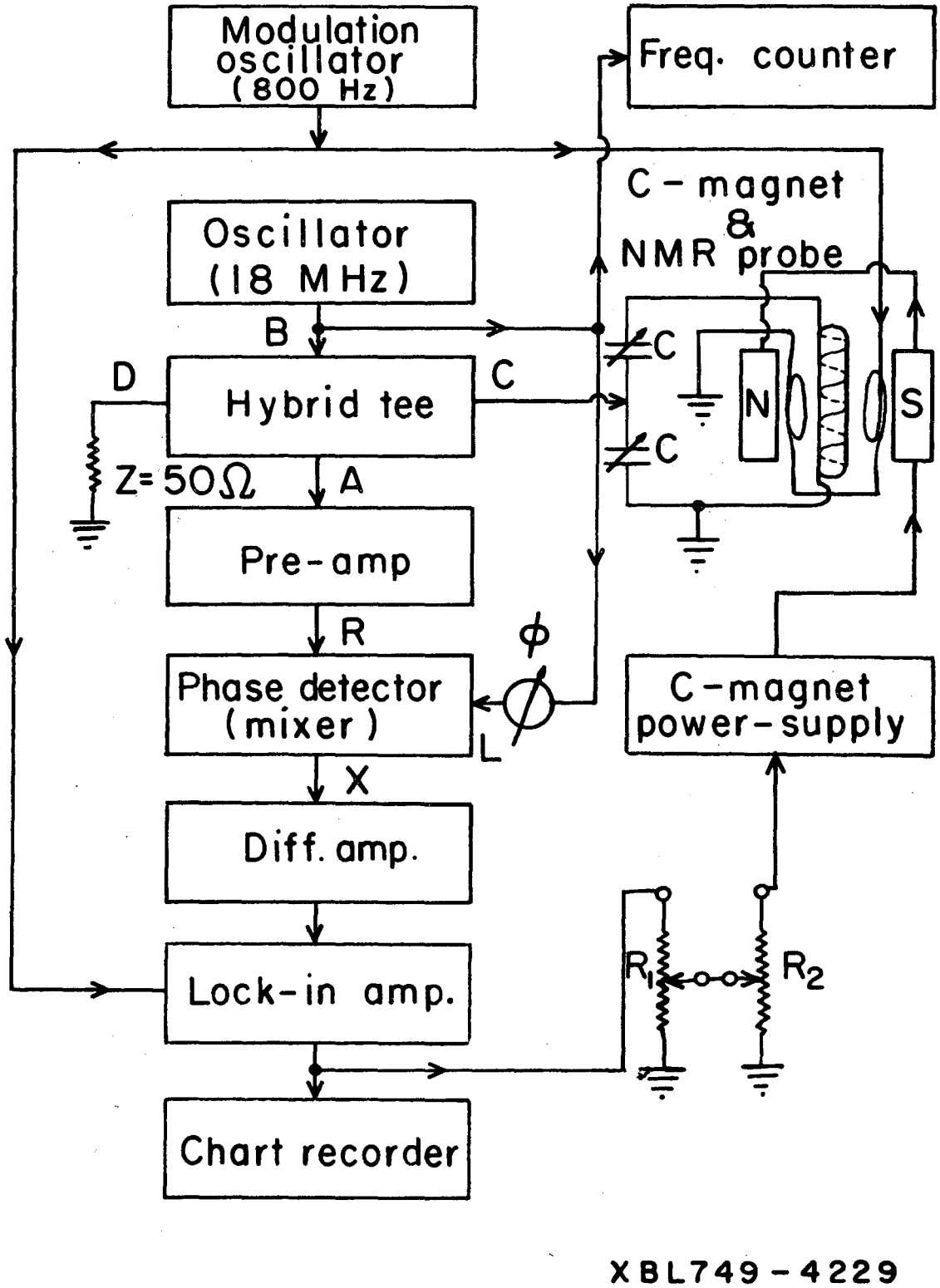

XBL749-4229

Fig. II. 11. N.M.R. field locking system.

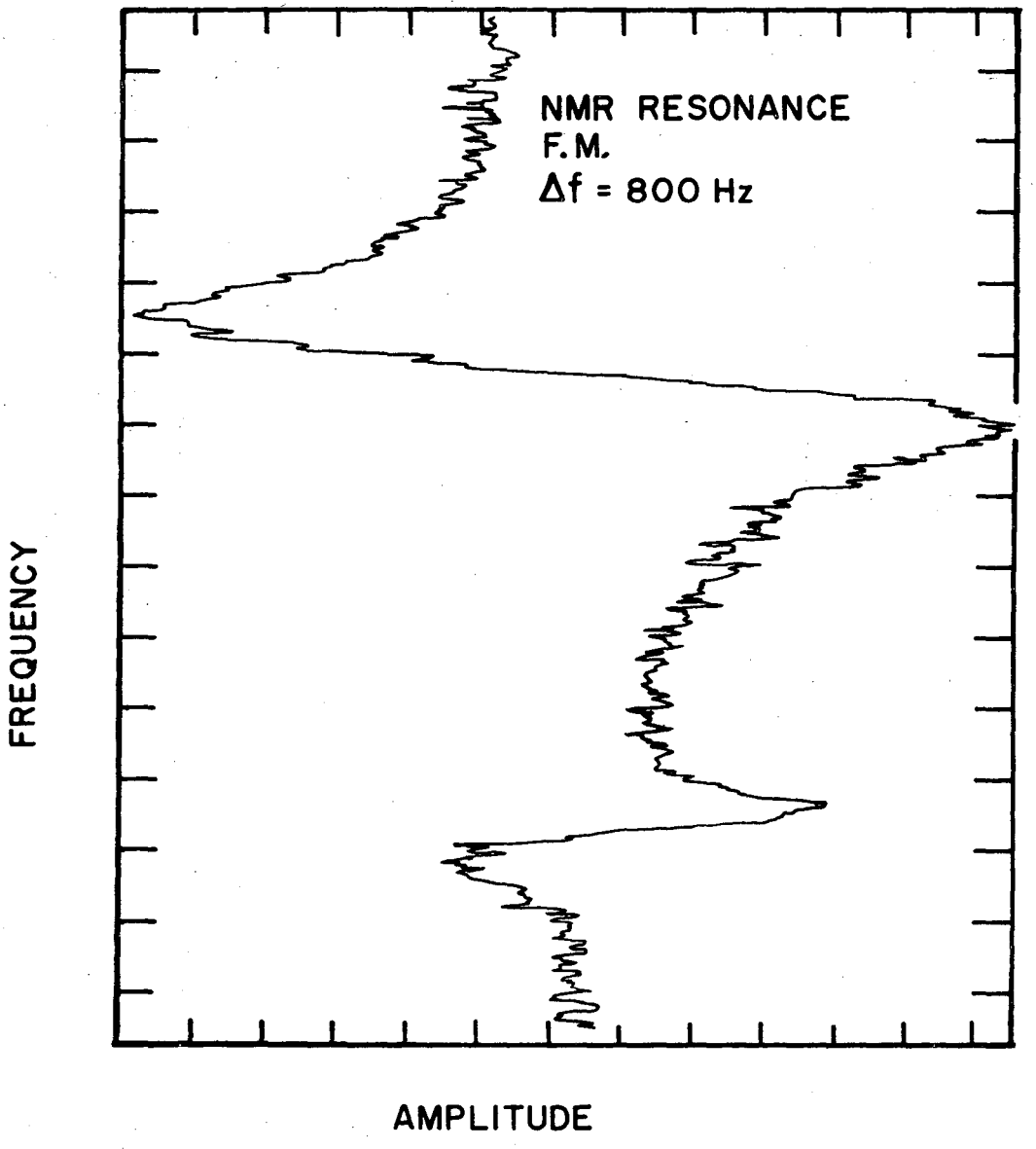

XBL 746-1101

Fig. II. 12. A typical dispersion curve of a proton nuclear magnetic resonance. (Gaussmeter system)

Actually, out of 160 pairs of resonances, only very few were discarded for this reason. Generally, the field remained constant during most of the runs, each lasting about 6 hours.

Other important factors affecting the precision of an atomic beam magnetic resonance experiment is the homogeneity of the field. We found that the homogeneity of the field depends largely on the history of hysteresis effects on the magnet pole pieces. However, the homogeneity can be improved by just degaussing the magnet and bringing it back to the set point. Further, adjustments now can be carried on by making use of the shim coils. For controlling horizontal, vertical, and circular gradients of the field, five sets of shim coils are placed in the C field. In our experiment, we have used the set as $x_3 + x_4$ for horizontal $y_1 + y_2$ for vertical and A_1 and A_2 for the circular homogeneities. The sets were derived by three D.C. constant current supplies. They can deliver the currents regulated down to 1 μ.a. Therefore, very fine adjustments on the field are possible. Fig. II. 13 shows the plan of installation of the shim coil sets. Coils on both sides of C can are wound so that the positive current travels clockwise as one looks toward the coils. Each coil consists of 10 turns of insulated 8 mil diameter copper wire. The design of the shim coils is explained by Anderson.[59] Fig. II. 14 is an example of the process of field homogenizing. The NMR probe for measuring the field was attached to the bottom part of the hairpin. In order to map the field in the region where the beam passes and r.f. transition takes place, we lifted the hairpin, i.e., the NMR probe,

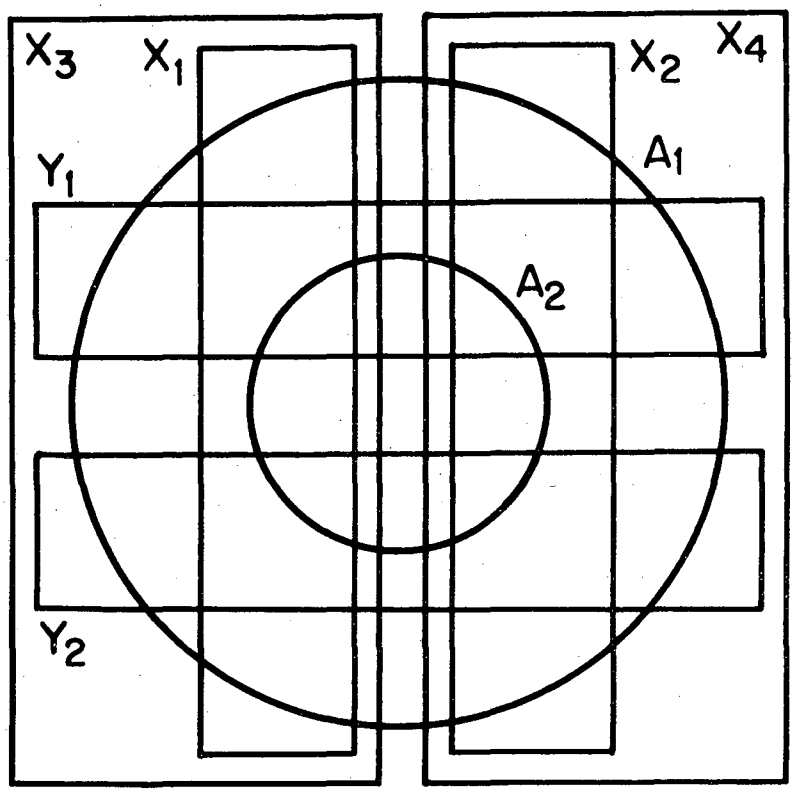

Resistances of coils:

Horizontal: $X_1 + X_2 = 2.7\,\Omega$

$X_3 + X_4 = 3.2\,\Omega$

Vertical: $Y_1 + Y_2 = 3.3\,\Omega$

Circular: $A_1 = 3.4\,\Omega$

$A_2 = 1.9\,\Omega$

XBL 749-4295

Fig. II. 13. Plan of the shim coil installation.

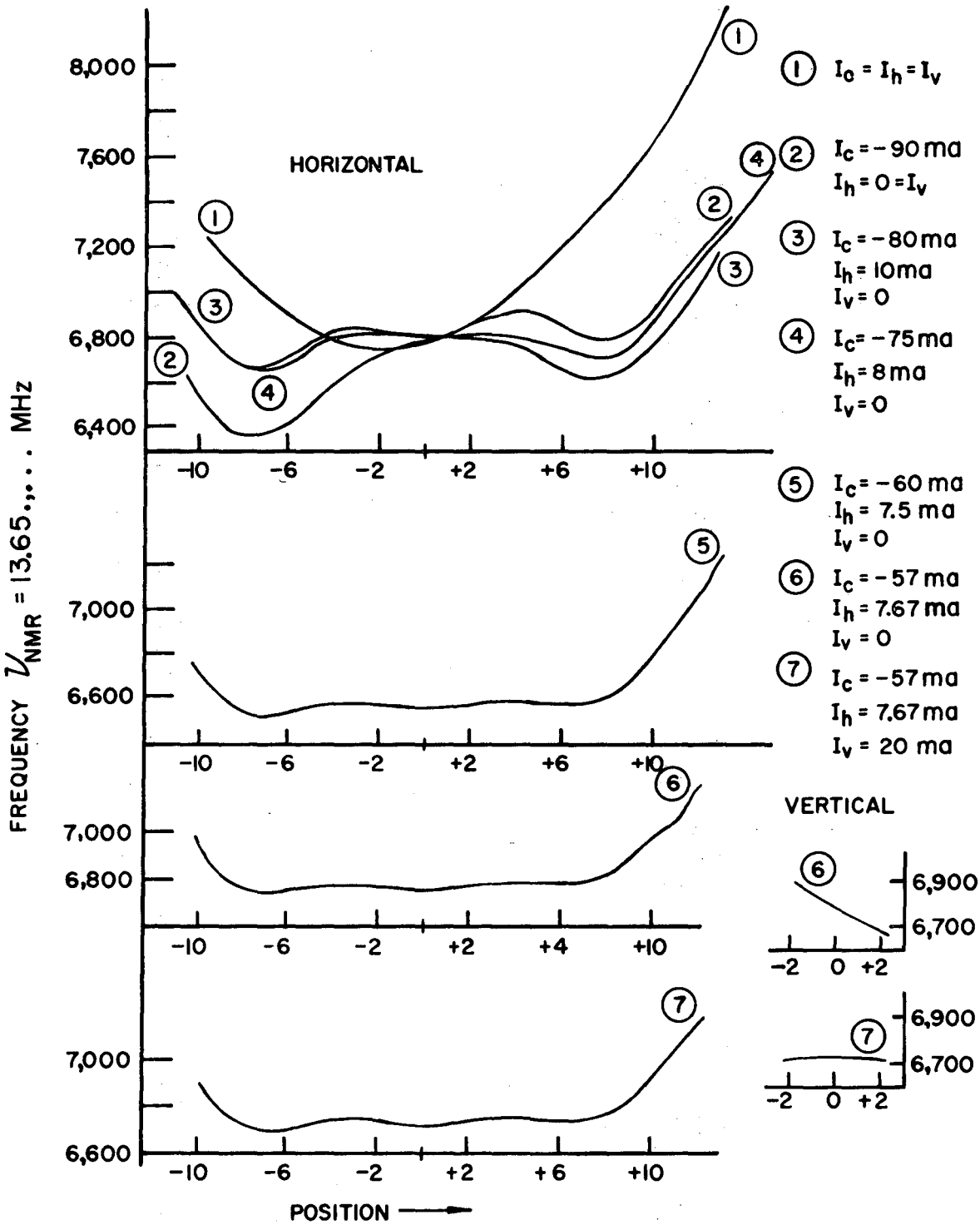

XBL 746-1100

Fig. II. 14. Field homogenizing in the horizontal and vertical directions.

by a distance of 1 1/8". Then the hairpin was moved in the horizontal direction toward the right side and the left side in 1/8" steps. The field was measured at each step. The total distance covered in the horizontal direction was about 3 inches. After a complete mapping, the current in the appropriate set of coils were adjusted to yield a better homogeneity. Then, the process was repeated many times until a satisfactory field homogeneity was obtained. By moving the hairpin up or down at 1/8" steps, one can also map the field in the vertical directions. The rest of the process of homogenizing is the same as the horizontal. When the vertical homogeneity was achieved, the field should be mapped again in the horizontal direction, since the current in the coils y_1 and y_2 would affect the field to some extent also in the horizontal direction. This way, going back and forth to horizontal and vertical directions, the final adjustments can be completed to have a field uniform to about 1 ppm in 2 inches distance horizontally, 0.5 ppm in 0.5 inch distance vertically. Naturally, the homogeneity in the actual r.f. region was better since the size of the r.f. region is smaller. After the field mapping was finished, the hairpin was brought to the center in the horizontal direction and lowered to a level such that the beam could pass through the hairpin slit.

Radio Frequency System. Equation II. (77) is the basic relation on which our atomic beam magnetic resonance comparison measurement was built. It clearly dictates that a precise and stable radio frequency is most desirable in a resonance experiment.

In fact, the technology of radio frequency sources, electronics and circuitry has been improved tremendously in the past few decades that a precision of 0.01 ppm can be achieved without much difficulty.

The Varian X-13 reflex klystron[60] oscillator is the main element of our radio frequency system. It can be set to any frequency from 8.2 to 12.4 GHz by changing the cavity dimensions with the micrometer mounted on it and adjusting the repeller voltage on the klystron power supply. We have worked at two different C field magnitudes, corresponding to four different frequencies for helium and oxygen. However, at a certain field the helium and oxygen frequencies were close enough to be alternated by the repeller voltage. The helium and oxygen frequencies at 4228 gauss were, respectively,11845.56 and 11844.71 MHz. The difference between the actual resonance frequencies of this field was about 860 KHz. At 3209 gauss, the frequencies were about 8990.33 and 8989.67 MHz, and the difference was 655 KHz.

Klystron frequency was locked on the smallest possible harmonic frequency of the reference oscillator, Hewlett-Packard Model 5105A frequency synthesizer. Since the frequency range of this device is 0-500 MHz, we set it to 493 MHz and used the 24th harmonic at 4228 gauss. At the lower field the frequency of the synthesizer was 498. MHz and the 18th harmonic was used. Having an analog and digital remote frequency control, the synthesizer could be ordered by the PDP 11 computer to sweep the frequency around the resonance frequency. As we mentioned in the data collection section, the part of the

synthesizer frequency in KHz order and the sweep steps were fed from the computer.

Fig. II. 15 is the block diagram of the radio frequency generation and the locking equipment. The synthesizer frequency is multiplied and amplified in two traveling wave tube amplifiers. The second harmonic of this frequency is compared with the klystron frequency in the mixer. The difference frequency of about 10 MHz is fed to FD 3 Schomandl syncriminator. Throughout the experiment, we have set the synthesizer frequency such that a certain harmonic of it was $\approx$ 10 MHz lower than the klystron frequency. The output of the harmonic mixer is phase compared with the 10 MHz standard frequency in FD 3 syncriminator. If a phase difference is detected, the FD 3 puts a positive or negative correction voltage on the reflector voltage of the klystron. Thus, the klystron frequency is always controlled to keep the phase difference zero. When the phase difference is kept zero, the klystron frequency is called "locked" on the output of the reference oscillator. The internal crystal reference of the synthesizer is checked with the local general radio 100 KHz standard frequency oscillator. As it is seen in Fig. II. 15, this standard in turn is compared with the WWVB 60 KHz signal received by the Gertsch phase comparison receiver. The 60 KHz signal is obtained from a Cs^{133} atomic clock by the National Bureau of Standards at Fort Collins, Colorado. The origin of the 10 MHz standard frequency going into the FD3 syncriminator was also the standard frequency oscillator. The 100 KHz output was first amplified, then

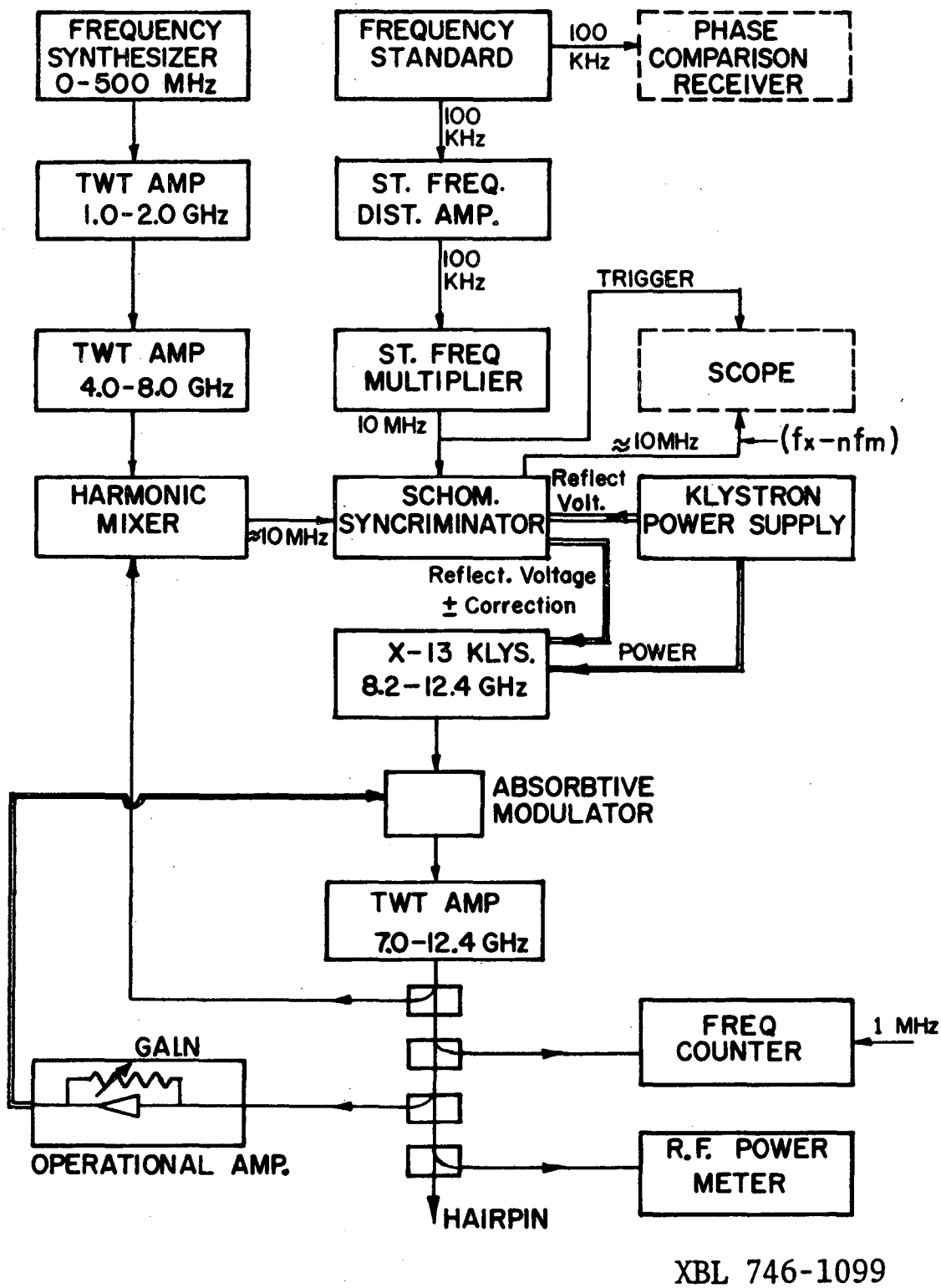

Fig. II. 15. Block diagram of the radio frequency system.

multiplied by 10^2 in the multiplier to get 10 MHz. The loop shown on the left lower part of the diagram was to level the r.f. power as the frequency varied due to scanning. The klystron frequency was measured by the Hewlett-Packard 5267M frequency counter by making use of the plug-in type 3-12.4 GHz frequency converter. The radio frequency power was measured first before the hairpin by the r.f. power meter. A directional coupler and an attenuater were used to reduce the power by 30 db to protect the power meter equipment. The r.f. power going into the hairpin was from 60 to 100 mw.

The r.f. hairpin which we have used in this experiment is shown in the Fig. II. 16. It consists of a 50 Ω coaxial line with off-centered entrance and exit slits for the beam and a 50 Ω termination pressed to the inner conductor by screwing a copper cap on the outer conductor. In this terminated hairpin, due to its low r.f. reflection property, ideally the standing waves are eliminated. So the particles of the beam were exposed to a uniform amplitude r.f. at various slit heights.

Experiment. The peak corresponding to $^5S_2$ state of oxygen atoms falls between the 5th and 30th channels of the time-of-flight distribution when the time per channel is 40 μsec. In the preparation studies, we tried to obtain an r.f. resonance of 4228 gauss on the ^5S metastable oxygen atoms. The time-of-flight distribution was divided into six groups. Fig. II. 17a is the photograph of the oscilloscope display at the end of the first ^5S oxygen resonance. Data collection time was 30 minutes. Table II. 1 gives the number of

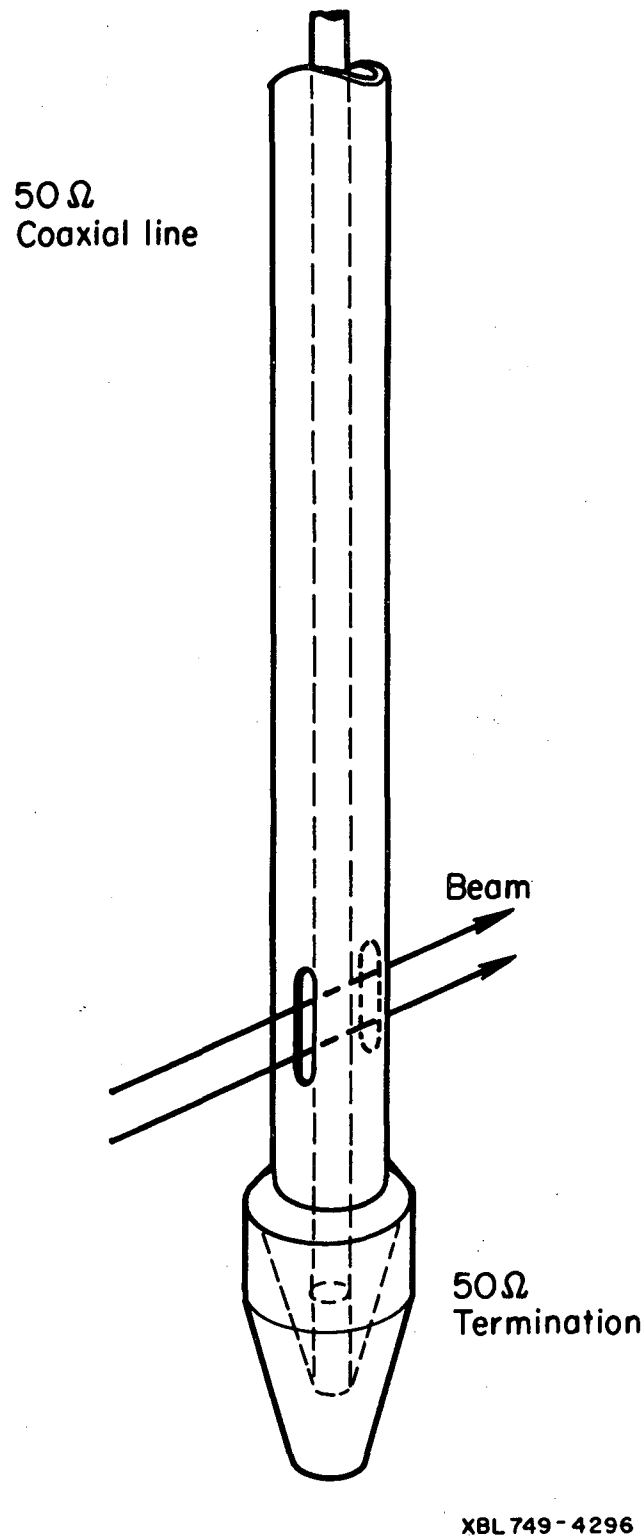

Fig. II. 16. 50 Ω terminated, low reflection hairpin.

(a)

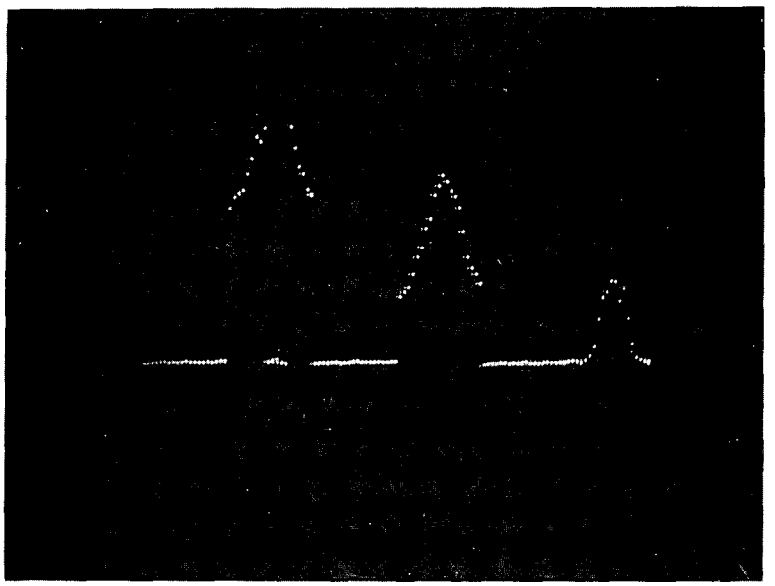

(b)

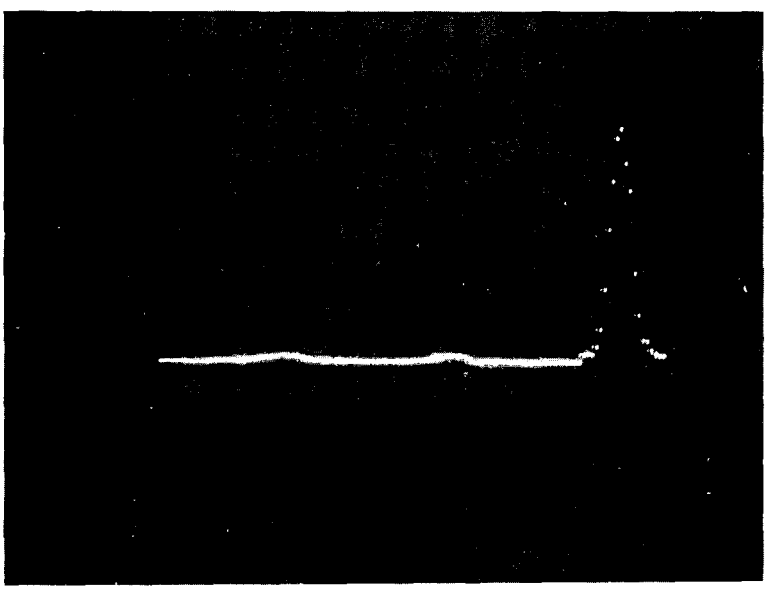

XBB 749-6598

Fig. II. 17. The first observed resonances in a) oxygen and b) helium.

channels included in different groups. The tail of the time-of-flight

Table II. 1. Time-of-flight distribution groups on the first $^5S_2$ oxygen and $^3S_1$ helium resonances.

Groups	Intervals of TOF Channels (decimal numbers)
1 st	46 - 64
2 nd	5 - 15
3 rd	46 - 64
4 th	8 - 16
5 th	46 - 64
6 th	16 - 40

distribution is in the 1st, 3rd, and 5th groups. The purpose of putting these particles in-between the resonating particles was to be able to separate clearly the resonance curve from the three different groups of ^5S atoms. It is obvious that the channels from 5 to 8 increased the background considerably. Therefore, in the actual measurements we have not included these fast particles. Runs between Ox 002 and Ox 103 were done with the $^5S_2$ atoms belonging to the time-of-flight

interval between the 10th and the 30th channels. On the right side of the photograph of Fig. II. 17b is shown a helium resonance curve, taken at the same field with the same conditions except the frequency was a bit higher. Helium $^3S_1$ atoms start to appear at channel 10, reach a peak at 20 and disappear at 45 in the time-of-flight distribution. This can be also seen in the resonance curve. While the second and the fourth groups have a small resonance effect, the sixth group displays by far the best resonance curve. Naturally, first, third and fifth groups, covering the same channels (46-64) contain very few $^3S_1$ atoms, would not be affected by r.f.

During the helium runs from He 001 to He 104, the channels on helium resonances were in the interval of channels 14 to 35. These decimal channel numbers were converted into octal numbers for depositing into the PDP 11 computer. Later we enlarged the interval of channels to cover both oxygen ^5S atoms and helium ^3S states. The time-of-flight interval for the runs from He 105 and Ox 106 to He 372 and Ox 371 were between the channels 10 to 35. This change has not decreased the signal background ratios, but the switching from one isotope to the other was much simplified.

The procedure that we have followed in the actual measurement was the following. After the C field was locked to the desired value, it was mapped and shimmed until we obtained a homogeneity of 1 ppm over 2 inches distance. This process normally takes about 5 to 8 hours. A magnet was operated at I_A = 5.0 amp. I_B was much lower (1.6 amps) since, otherwise, helium ^3S atoms would be deflected too much and miss

the detector. Meanwhile, the frequency system and the PDP 11 computer were turned on. Then, frequency was locked to a value which corresponds roughly to helium resonance frequency at that magnetic field. Knowing the NMR lock frequency, the magnetic field could be determined to a precision of 4 ppm by making use of the NMR field tables. Power level of the r.f. is adjusted to the optimum value and controlled by the servo-loop. In order to find the optimum r.f. power for the resonance, we have done several runs with both helium and oxygen at various r.f. powers. Helium power-study runs were the runs from He 024 to He 034. Oxygen runs from Ox 047 to Ox 051, when combined with the results of the helium runs, showed us that r.f. power in the interval of 70 - 100 mw give the best signal-to-background ratio and the line shape for both oxygen and helium.

Since the screw controlled, vacuum-tight sliding plate system covered a limited distance, most of the time we isolated the C can from the rest of the machine by closing the two values on the sides, and opened to atmospheric pressure by letting air into it. This enabled us to slide the hairpin which carried the field measuring NMR probe over a larger range for better field shimming and homogenizing. After it was accomplished, we had to pump on the C can by mechanical pumps and then, by opening the valves on the sides, we connected it to the rest of the apparatus. From this time, with all of the mechanical pumps and diffusion pumps running, it took about two hours to reach a vacuum of 5×10^{-7} torr all over the apparatus. During the runs however, the pressure in the B chamber was lower than the above value. The

A chamber had higher pressure since it was closer to the gas inlet, i.e., the discharge source.

When the homogeneity, vacuum and the r.f. lock were in good shape, the MEM detector supply and counters were turned on. The time per channel and the repetition rate of the discharge pulse was checked. The source r.f. supply was turned on. A few minutes later, allowing for warm-up time, the power was increased to a certain setting. The valve between the mechanical pump and the gas feed line was closed. (See Fig. I. 5). The first valves on the gas cylinders were always wide open. The second ones were adjusted to a low value such as 10 or 20. The last valve before the source was opened. Then, gradually the variable leak II would be unscrewed until a strong helium discharge starts. Usually this happens at the setting 140. An oscilloscope was hooked to the r.f. cable to monitor the condition of the discharge during the runs. Sometimes the source position should be re-arranged in the z-direction to get the maximum reading at the counter. The next step was to observe a helium resonance on the Counter I by monitoring the r.f. manually on the frequency synthesizer. This led us to the finer determination of the helium resonance frequency. The oxygen resonance frequency was also determined the same way. However, we needed to determine the oxygen frequency only at the beginning of a series of runs at a certain field. Afterwards, knowing the difference between the resonance frequencies of helium and oxygen, the information for the helium resonance already establishes the oxygen frequency

approximately.

The frequency 20 KHz lower than the helium resonance frequency was entered to PDP 11 as the initial scan frequency. The frequency step was fixed as 2 KHz. The frequency was locked again by varying the repeller voltage on klystron power supply. The C field lock was checked and the monitoring chart recorder was started to operate. Vacuum, discharge, and other systems were checked again, and data collection was started. Extreme caution was given to keep the r.f. locked during frequency scanning. An oscilloscope (see Fig. II. 14) was connected to FD 3 syncriminator to watch the frequency locking on its bigger screen. The resonance data was collected and displayed at 20 data points each representing a frequency step. If the curve was not symmetric, the initial frequency was re-adjusted to center the curve. Adequate data was collected in two or three minutes for helium runs. Previous to and during the first runs, the experimental conditions were recorded on a mimeographed form. A sample is given in Table II. 2. It contains also information on several runs. Data collection was stopped after 2 or 3 minutes and data was printed by teletype and punched on IBM cards by the keypunch machine. Then the frequency was switched and locked to oxygen frequency, oxygen discharge was started, and data collection was initiated. These processes between the two consecutive helium and oxygen runs took about 4 to 8 minutes if nothing went wrong and no more adjustments were necessary. Oxygen data was collected in either 10 or 15 minutes. Usually, six oxygen and seven helium resonances were taken successively under

Table II. 2. A sample of the experimental conditions page.

$g_J(O,{}^5S_2)/g_J(He,{}^3S_1)$ MEASUREMENT

EXPERIMENTAL CONDITIONS: DATE: June 6, 1974

Pressures (torr): A cham. 5×10^{-7} (He) B. cham. 4×10^{-7} (He) Mag. Currents: I_A=5.0 I_B=1.6 (amps)

1.7×10^{-6} (O) 4×10^{-7} (O) I_C= 30-10-99 (setting)

Gaussmeter Reading: 3700 gauss

NMR Lock. Freq: 13.662 320 sec^{-1} Shim Currents: $I_{hor.}$ -12.4 $I_{ver.}$ -14.5 $I_{cur.}$ 55 (ma)

Estimate of Field Stability 1 ppm/hr Field Homogeneity: Hor. 1×10^{-6} Ver. 1×10^{-6}

Disch. RF Power 74 (set.) Source Pres.: He tank 1200 He Pres. 17 He Set. 140.

Total Count Rates: Oxygen 7000 sec^{-1} O tank 1000 O Pres. 9 O Set. 151.5

Helium 2600 sec^{-1}

Syn. In. Freq. 498.889 MHz (1st He.) # of Pnts. 20 Incr. 2KHz Harm. 18 Freq. Dif. +10 MHz

Initial Klystron Freq. 8990. MHz (1st He). Klystron Power 80 mw

TOF/Ch: 40 μ sec Rep. Rate: 6.5 msec Hrp.Pos.: Hor. 0 Ver. 0 (unit $\frac{1}{8}$ in.)

TOF Chans. on resonance: He 10-35 (dec.) 13-43 (oct.) Other information: Field lowered

O 10-35 (dec.) 13-43 (oct.) Hairpin normal orientation

Field normal orientation

To be filled at the end of the measurement:

Is the C-Field still locked? yes X no

TIME	RUN NUMBER	SYN. IN. FREQ.	DURATION OF SCAN.	OTHER INFO
16.33	He 211	498.889 MHz	2 minutes	Hrp. Pos. Hor. 0 Ver. 0
16.40	Ox 212	498.853	10 minutes	
16.53	He 213	498.889	2 minutes	
17.00	Ox 214	498.853	10 minutes	
17.13	He 215	498.889	2 minutes	
17.18	Ox 216	498.853	10 minutes	
17.29	He 217	498.889	2 minutes	
17.31	Ox 218	498.853	10 minutes	
17.43	He 219	498.889	2 minutes	
17.46	Ox 220	498.853	10 minutes	
17.58	He 221	498.889	2 minutes	
18.03	Ox 222	498.853	10 minutes	
18.14	He 223	498.889	2 minutes	
18.24	He 224	498.889	2 minutes	Hrp. Pos. Hor +1 Ver 0
18.29	Ox 225	498.853	10 minutes	
18.35	He 226	498.889	3 minutes	
18.39	Ox 227	498.853	10 minutes	

XBL 7410-1783

the same conditions. Once started, three such sets were completed varying hairpin position or r.f. power each time, if nothing goes unexpectedly. At the end, all the data was inserted into the data book. Punched IBM data cards were cross-checked with the teletype printout, the punch format, or information errors were corrected and run numbers were punched on the cards manually.

C. Data, Analysis and Results

In this experiment we have collected the data for 372 individual resonances. Five oxygen resonance and 11 helium resonance runs were made to investigate the r.f. power dependance. They were not included in the g_J determination. Only five oxygen resonances were eliminated from the data because of random effects.

Data Handling. The IBM cards punched automatically by the keypunch machine contain only the counts at 20 frequency points of resonance. Later the run numbers are punched on these cards. The information about the synthesizer frequency, frequency steps, the harmonic and the frequency difference taken from the mixer was given on a separate card for each resonance. A third card was put to be used in the case to give some explanatory information about the individual run. Therefore, each run was represented by four cards. The first card had frequency, the second information, the third and fourth carried the data of resonance counts.

The data deck combined with the LFIT program deck was evaluated in the Lawrence Berkeley Laboratory computer (CDC 7600). The program LFIT fitted the experimental resonance curves into the Lorentzian line shape using the least squares technique. It plotted the experimental and fitted resonance curves, printed the χ^2 which is a test of the reliability of the fit. It also listed the amplitude, background,

resonance frequency, resonance width and the errors on these quantities. Fig. II. 18 and II. 19 are the redrawn resonance curves using the information plotted by the computer. This information was also punched on the IBM cards with the run numbers for further processing. The output of LFIT program was inspected for extraordinarily big χ^2 and strange-looking resonance curves. If there were mistakes in the data given to the computer, they were corrected and re-processed in the computer with the following run data. If the data was bad due to the random errors, they were discarded. Such cases, however, were very few. The cards punched by the CDC 7600 were used together with the program AVERAGE in order to calculate the g_J factor. This program could be handled by the IBM 1620 which is located in the basement of the physics building, Birge Hall. It calculated the ratio of g_J factors of oxygen ^5S, and helium ^3S atoms, by comparing the average frequency of two helium resonances, one previous -- the other following with the oxygen resonance frequency. Then, using the value of helium g_J, it calculated the g_J value of ^5S oxygen atoms for each individual run. It could also print the average g_J value of the desired group of runs. The errors were printed for every calculated quantity as well. We analyzed the data by checking the results. If we suspected a value, we went back to the data book for this run and followed the routine until we cleared out the problem. Next we prepared the histograms, decided on the average g_J value and the errors to be quoted. Both of the programs we have used LFIT and AVERAGE were developed by Professor Howard A. Shugart.

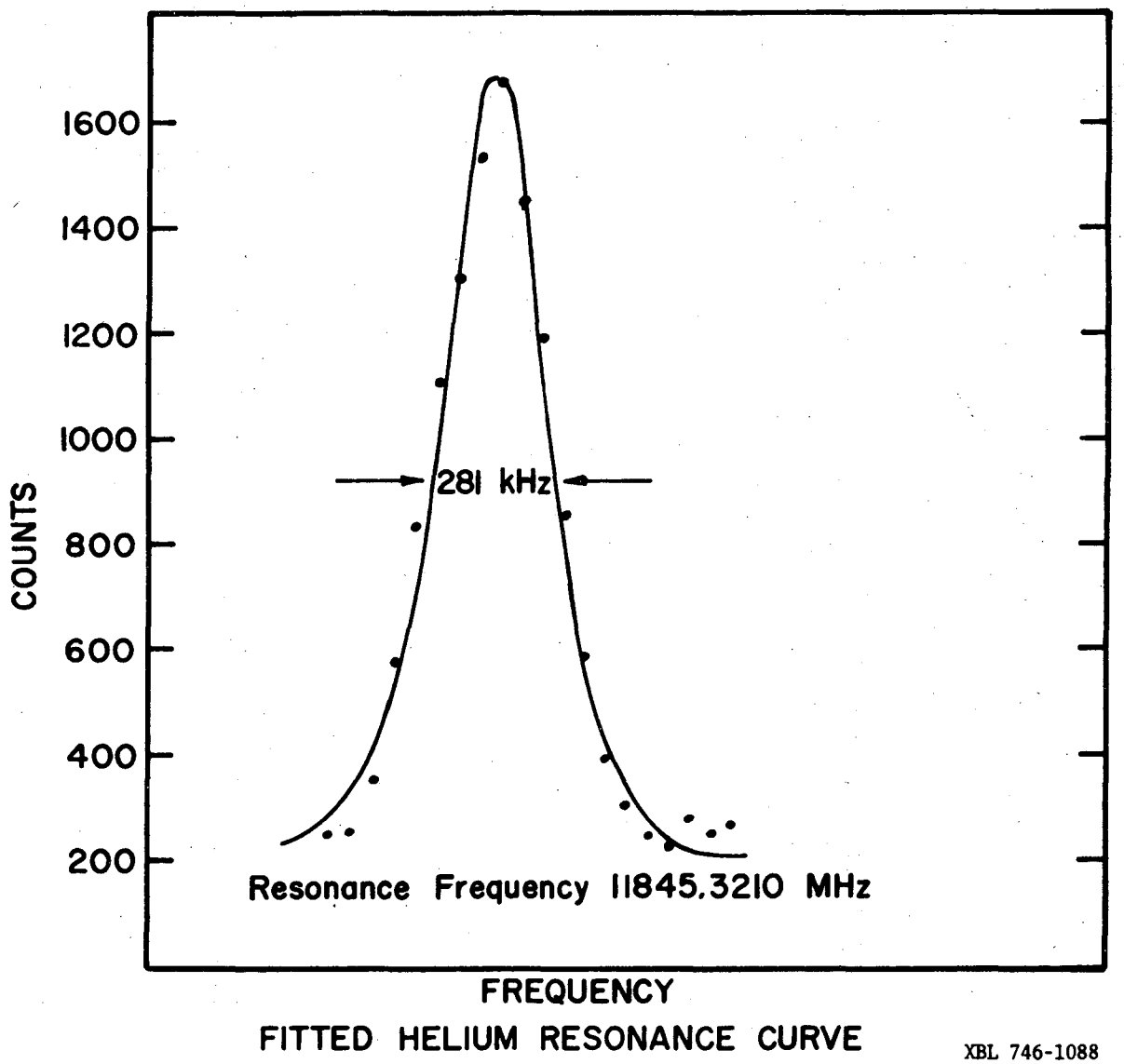

Fig. II. 18. Line shape fitted to the He 033 resonance curve. The dots represent the experimental data.

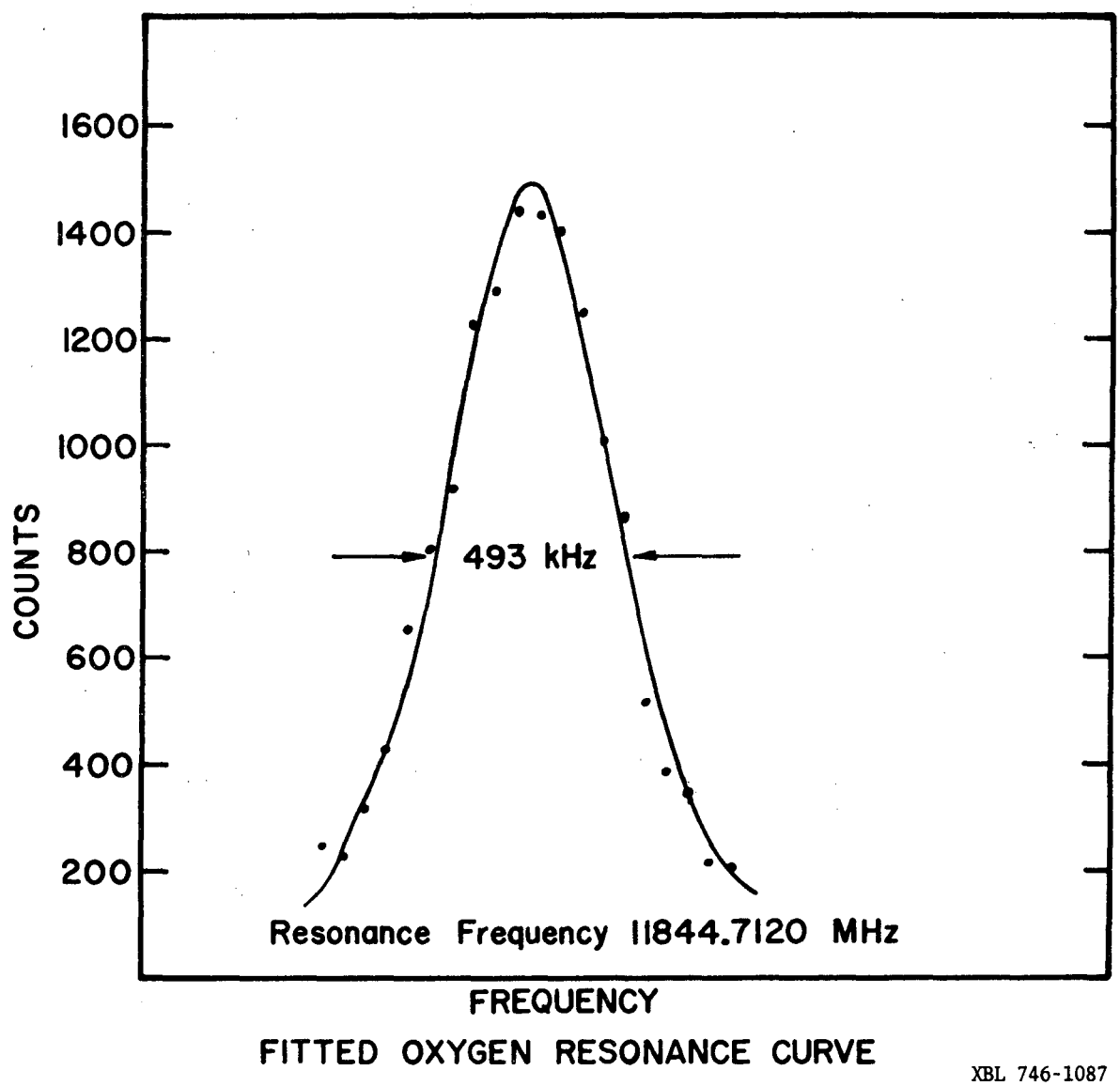

Fig. II. 19. Line shape fitted to the Ox 048 resonance curve. Dots are the experimental points.

Analysis. The data of the runs can be considered in two major groups. One group of runs was made at a C field of 4228 gauss and the other group corresponds to a C field of 3209 gauss. These groups can be split into subgroups according to various C field and hairpin orientations. And finally, each of these subgroups can be divided into three smaller groups, each having a different hairpin position. Table II. 3 summarizes the various groups, eight subgroups and gives the run numbers included in them. Since we always start and end a series of runs with helium runs, the run numbers which are shown on Table II. 3 belong to all helium runs. Oxygen runs naturally are in between. The normal direction for the field is the direction when the

Table II. 3. The groups of experimental data.

Mag. Field	Run Numbers	C-field Orientation	Hairpin Orientation
4228 gauss	He 001 - He 068	Reverse	Normal
	He 069 - He 130	Reverse	Reverse
	He 131 - He 169	Normal	Reverse
	He 170 - He 210	Normal	Normal
3209 gauss	He 211 - He 249	Normal	Normal
	He 250 - He 288	Normal	Reverse
	He 289 - He 329	Reverse	Reverse
	He 330 - He 372	Reverse	Normal

current supply is operated in normal direction mode. The normal direction in the hairpin orientation was taken arbitrarily, but it is all consistent.

The data were processed three times with three slightly different LFIT programs, namely four parameter, three parameter and four parameter gradient programs. The output of the LFIT program was evaluated with the program AVERAGE. For all three types of LFIT programs, we have three g_J listings and averages. A fourth g_J listing and average, which we called best fit calculation and averages, was obtained by using the selected output cards of different LFIT programs for every individual resonance. The criteria for selecting the calculation LFIT of a resonance was smallest χ^2 among the three existing outputs. However, most of the calculations were taken from the four parameter fit program outputs. A flow diagram of the four parameter LFIT program and basic information about the subroutines are given in Appendix C. Appendix D is the program AVERAGE.

The transition probability from one atomic level to another is given[36] as

$$P = \frac{(2b)^2}{(2b)^2 + (w_o - w)^2} \sin^2 \left\{ \frac{1}{2} \left[(2b)^2 + (w_o - w)^2 \right]^{1/2} t \right\} \quad \text{II.} \quad (78)$$

where the w_o is the resonance center frequency and w is any frequency. b is related with the full half width, i.e., $\Delta w = 4b$. Because of the distribution of t, the time that the atoms spends in the transition region, the $\sin^2$ term on the right side averages to a fixed value. Then, the experimental resonance curve would be represented[61] by a Lorentzian distribution

$$y(P_1, P_2, P_3, P_4) = \frac{P_1}{1 + P_2(w_i - P_3)^2} + P_4 \qquad \text{II. (79)}$$

P_1 is the amplitude, P_2 is the parameter related to the line width, w_i is the channel number with $i = 1, 2 \ldots 20$, P_3 is the channel number of the resonance center and P_4 is the background.

The best fitting Lorentzian curve can be obtained if

$$\left(\frac{d\chi^2}{dP_j}\right) = 0 \qquad \text{II.(80)}$$

where j runs from 1 to the number of parameters, and χ^2 is defined by[61]

$$\chi^2 = \sum_{i=1}^{20} \left[y_i(\text{obs}) - y_i(P_j) \right]^2 x_i \qquad \text{II. (81)}$$

Observed resonance points and Lorentzian distribution points are, respectively, represented by $y_i(\text{obs})$ and $y_i(P_j)$. x_i is the weight factor. Obviously, when χ^2 approaches a minimum, the condition in Equation II. 80 will be fulfilled. Inserting the Equation II. (81) into the Equation II. (80), we obtain j simultaneous equations. Then, the solutions of these equations would yield the proper parameters for the best fitting Lorentzian curve. From here on the calculations for the resonance frequency, half-full width and errors are quite straight forward.

Errors. The most important problem in a precision atomic beam measurement is to determine whether the experimental peak corresponds to the exact energy difference between the levels concerned or there is a

certain shift due to the distortions of the resonance. The cause of the distortions may vary, such as Millman effect,[63] Doppler effect,[36] field inhomogeneity and instability, high or low r.f. power, instability in frequency and scan. However, the improved equipment, experimental techniques reduce the sources and the effect of errors on the measurement.

The accuracy of the result of our measurement might be influenced by some, all or even additional effects to the ones listed above. Although the number of potential error sources seems to be big, we believe that we have a good control on them. The information about the apparatus run conditions, experimental procedure and precautions were explained under the "apparatus and experiment" headline. Here we will give a brief account only on those efforts which are directly involved in the accuracy of the experiment.

The temperature of the laboratory and equipment were kept constant by thermostat controlled air condition. This especially improved the long term stability of the C magnet power supply. The systematic errors due to field and hairpin were reduced by running at various hairpin positions, hairpin orientations and field orientations. The Millman effect which arises from the variation of the direction of r.f. field in the transition region was cancelled by changing the orientation of the field and hairpin. The atom having a velocity v in the r.f. region would cause a Doppler shift[64]

$$\Delta\nu \approx \nu \frac{v}{c} \cos \Theta \qquad \text{II. (82)}$$

where ν is the resonance frequency and c is the velocity of light and Θ is the angle between the propagation vectors.

Since the radio frequency power in our hairpin travels practically perpendicular to the beam, the Doppler effect is expected to be low. The shift, due to a small tilting of the hairpin, should be reversed when the hairpin is rotated 180°. If there are standing waves in the hairpin, the atom would see the two waves travelling in opposite directions. Consequently, the positive and negative Doppler shifts broaden the resonance curve, assuming equal amplitudes of the incoming and outgoing waves. However, a shift would accompany a smaller broadening if the amplitudes differ. Because of its highly reduced reflected r.f. power and small transition region, the 50 Ω-terminated hairpin, we have used, is by far the best when compared with shortened hairpins in obtaining consistent results.

The r.f. power studies helped us minimize the resonance distortions due to saturation, and avoid low signal-to-background ratio due to weak radio frequency.

The factors causing the random errors were corrected as soon as we noticed them during the experiment. These were mainly, an increase in the pressure in the apparatus, a change of mode or weakening of the discharge, magnetic field instability due to the lack of lock and external effects, and radio frequency shifting out of lock during the scanning. Since we displayed the resonance curve on the oscilloscope during the data collection, any distortion in its shape warned us to check the experimental conditions thoroughly. Most of the time, the

distortions were associated with an unlocked radio frequency which could also be detected easily on the screen of another oscilloscope. Field instability was very infrequent. Field stability was monitored on a chart recorder and seemed to be pretty unchanged under external electrical effects. We were cautious not to distort it by moving magnetic materials close to the C field region. Immediately upon observing a situation that stands to be a reason for a poor resonance, the data collection was stopped, the data that were collected so far werecleared and the conditions were corrected. Very few resonance data were rejected after they were processed in the computer, since they did not seem to be apparently unsatisfactory during the experiment.

Certainly, the error quoted in the final result also includes the effect of the uncertainty in the g_J factor of $^3S_1$ helium, our comparison isotope.

Results. The list of g_J values are shown in Table II. 4, at each of the magnetic field values used, with four relative normal and reverse directions of the field and hairpin. As we pointed out previously in other words, the C field was called in normal orientation when it was in the same sense as the fields in the A and B magnet. The g_J value of ^3S state of helium was taken from Referance 25 and 54 as

$$g_J(^3S_1, He^4) = -\ 2.00223735(60). \qquad \text{II. (83)}$$

As it is seen on the Table II. 4, various fit programs yield remarkably consistent results. Besides, the agreement between the different groups

Table II. 4. A list of intermediate g_J values and averages. N and R refer to the normal and reverse directions. 160 pairs of resonances are represented in the first three fits.

C-FIELD	ORIENTATIONS		FOUR PARAMETER FIT		THREE PARAMETER FIT		GRADIENT FIT		BEST (X^2 MIN) RESULT OF THE THREE METHODS	
	Field	Hrp.	g_J	No.of Obsv.	g_J	No. of Obsv.	g_J	No.of Obsv.	g_J	No.of Obsv.
4228 gauss	R	N	-2.0020909(1)	21	-2.0020907(1)	21	-2.0020908(1)	21	-2.0020908(1)	21
	R	R	-2.0020921(1)	28	-2.0020920(1)	28	-2.0020921(1)	28	-2.0020921(1)	28*
	N	R	-2.0020909(0)	18	-2.0020904(1)	18	-2.0020909(0)	18	-2.0020909(0)	18
	N	N	-2.0020906(1)	19	-2.0020907(2)	19	-2.0020907(2)	19	-2.0020906(1)	19
	$\bar{g}_J$		-2.0020912(1)	86	-2.0020911(1)	86	-2.0020912(1)	86	-2.0020912(1)	86
3209 gauss	N	N	-2.0020908(2)	18	-2.0020908(1)	18	-2.0020906(2)	18	-2.0020908(2)	18
	N	R	-2.0020908(1)	18	-2.0020909(1)	18	-2.0020907(0)	18	-2.0020910(1)	18
	R	R	-2.0020909(1)	19	-2.0020909(2)	19	-2.0020907(1)	19	-2.0020909(1)	19
	R	N	-2.0020905(1)	19	-2.0020903(1)	19	-2.0020904(1)	19	-2.0020906(1)	18**
	$\bar{g}_J$		-2.0020907(1)	74	-2.0020907(0)	74	-2.0020906(1)	74	-2.0020908(0)	73

XBL 7410-1782

* Ox 110 data with g_J = -2.0020949 is included here. However, it is not included in the histogram -- Fig. II. 20.

** Ox 339 and Ox 361 are rejected.

of runs, with the exception of higher field R R relative orientation results, is very clear. The last column in Table II. 4 represents the results obtained by using the best fitted calculations out of all the information furnished by the three slightly different LFIT programs.

The average ratio of the g_J's out of the calculations based on the best fitted resonance lines is

$$\frac{g_J(^5S_2,\ O^{16})}{g_J(^3S_1,\ He^4)} = 0.9999269(4). \qquad \text{II. (84)}$$

when this value is combined with the g_J value of $^3S_1$ helium given in Equation II. (83), the final g_J value of $^5S_2$ metastable state of atomic oxygen turns out to be

$$g_J(^5S_2,\ O^{16}) = -\ 2.0020910(10). \qquad \text{II. (85)}$$

The indicated error of 0.5 ppm covers about 82% of the individual measurements in the case of best fit calculations. The calculations built upon the other fitting programs yield coverages between 74 and 80 percent. A histogram of the results is shown in the Fig. II. 20. It represents the results obtained by using the best fitted line calculations.

Conclusion. The measurement which has been described in this report happens to be the first precision determination of the g_J factor of $^5S_2$ metastable state of atomic oxygen. The earlier of the two previous

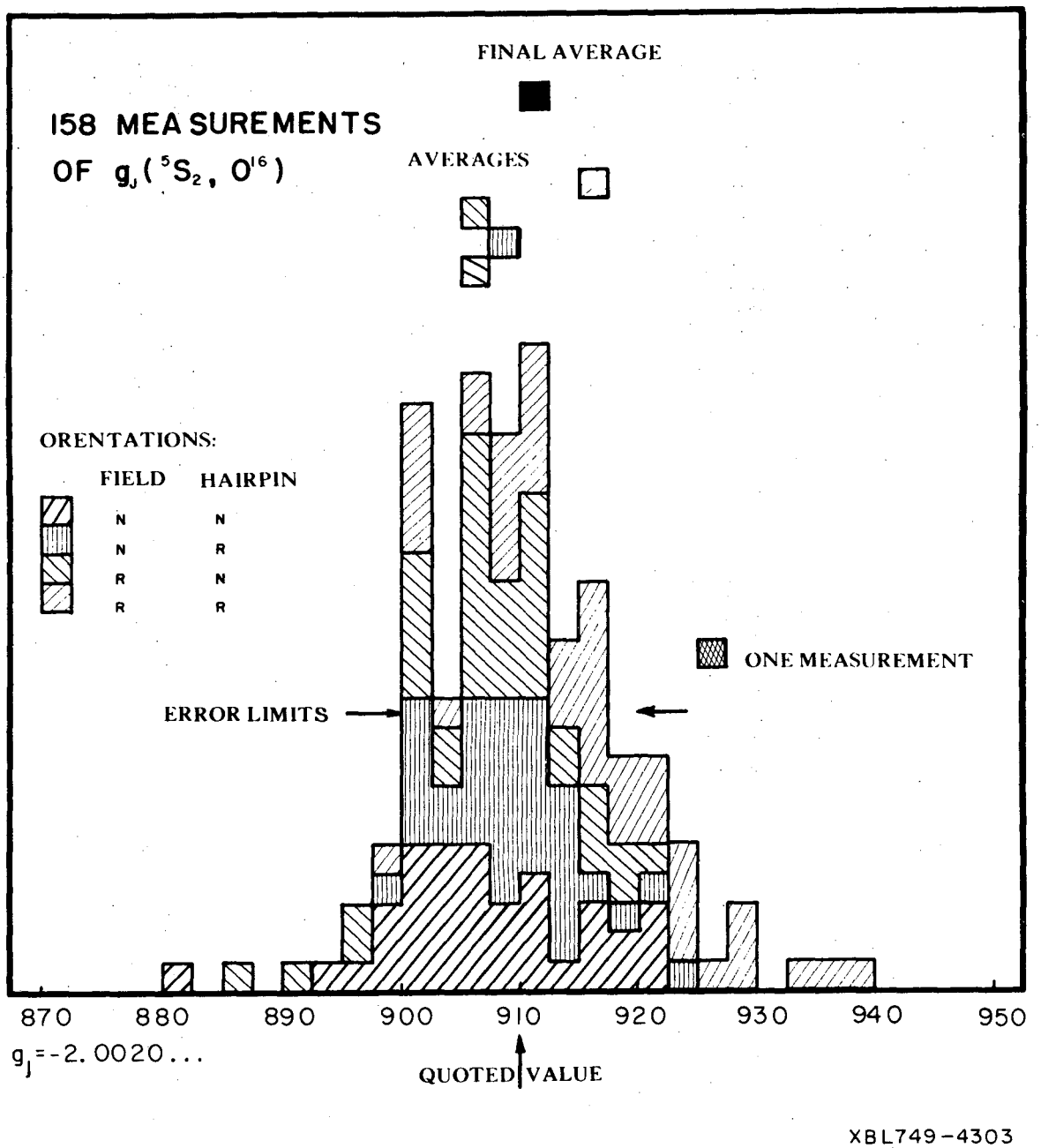

Fig. II. 20. Histogram of the best fit results.

measurements (Ref.8) was carried out by Kiess and Shortly in 1949. They made use of the optical spectrum of red light of atomic oxygen, with wave lengths at 7771 to 7775 Å emitted from $3p^3\ 3s\ ^5S - 3p\ ^5p$ in arcs in air between metallic electrodes. Comparing the spectrums taken at no field and at 34600 and 85400 gauss, they derived the g_J splitting factor of ^5S quintet state of oxygen as $g_J = -1.999(2)$. This value, even with its upper error limit, is smaller than our results.

"In the course of molecular beam magnetic resonance investigation of the products produced by a microwave discharge in O_2" Brink[9] observed "a strong resonance with a g factor of 2." Although the technique was similar to that we used, geometry, detection method and comparison isotope were completely different. After attributing this resonance to ^5S state of atomic oxygen he gave the result as $g_J = -1.97(5)$. The sign is a matter of convention.

In the survey of literature, we have met precision calculations[65] and measurement[66] of g_J factors of $2p^4\ ^3P_1$ and $2p^4\ ^3P_2$ states of atomic oxygen. But, due to the absence of a theoretical calculation on the g_J factor of ^5S atomic oxygen, during the progress of the experiment, we were not able to evaluate our results in comparison to the previous calculations. However, after our preliminary results were presented by Professor Howard A. Shugart in the Fourth International Conference on Atomic Physics in Heidelberg, we had an immediate response[67] from Roger A. Hegstrom who states:

"As I believe I mentioned to you in Heidelberg, I have formulated a very approximate, but simple scheme for

calculating g_J factors, which works very well for the He 2 ^3S and Li. I was pleasantly surprised to find that this scheme predicts your experimental value for g_J of ^5S oxygen to within 10 ppm; furthermore it says that three unpaired 2p electrons contribute all but about 2 ppm to the bound state correction, this being primarily due to the greater speed andconsequently by greater increase in relativistic mass of the 2p electron. After testing this method more thoroughly, I may eventually write it up for publication and will gladly send you a reprint."

It is possible that the theoretical calculations will soon approach the same accuracy of our results and, therefore, provide the impetus for further measurements with better precision than ours.

APPENDIX A

TIME-OF-FLIGHT SPECTRUM DATA OF THE DISSOCIATION FRAGMENTS OF NITROGEN

13.3 μsec/channel

18482	205547	67690	999	4843
39638	43586	33038	26321	18851
10235	4430	1717	738	472
388	344	331	297	267
263	266	251	283	283
309	292	298	292	269
225	201	220	192	196
187	191	145	169	164
157	155	143	154	156
159	182	167	165	166
172	172	170	181	190
204	230	210	204	217
195	250	258	247	

APPENDIX B

Computer program to search for atomic magnetic moments in all L, S coupling cases. $3.75\ \mu_B \leqslant \mu \leqslant 4.25\ \mu_B$ for $L = 0$ to 30 and $S = \frac{1}{2}, \frac{3}{2}, \frac{5}{2}$.

```
      PROGRAM SEARCH(INPUT,OUTPUT)
**FORX54
*LISTPRINTER
      AL=-1.
      DO 100 I=1,30
      AL=AL+1.
      S=-.5
      DO 50 J=1,3
      S=S+1.
      AJ=AL+S
      AJMIN=ABSF(AL-S)
   15 ATEST=AJ
      AMJ=AJ
      GJ=-1.5+(AL*(AL+1.)-S*(S+1.))/(2.*AJ*(AJ+1.))
   20 AMU=AMJ*GJ
      IF(AMU-4.25)25,40,40
   25 IF(AMU-3.75)40,40,30
   30 PRINT 35,AL,S,AJ,AMJ,GJ,AMU
   35 FORMAT(1H ,4F10.1,2F10.3)
   40 AMJ=AMJ-1.
      IF(AMJ+ATEST)45,20,20
   45 AJ=AJ-1.
      IF(AJ-AJMIN)50,15,15
   50 CONTINUE
  100 CONTINUE
      END
```

APPENDIX C

The flow diagram of the program LFIT. Information on the operations are given in the blocks.

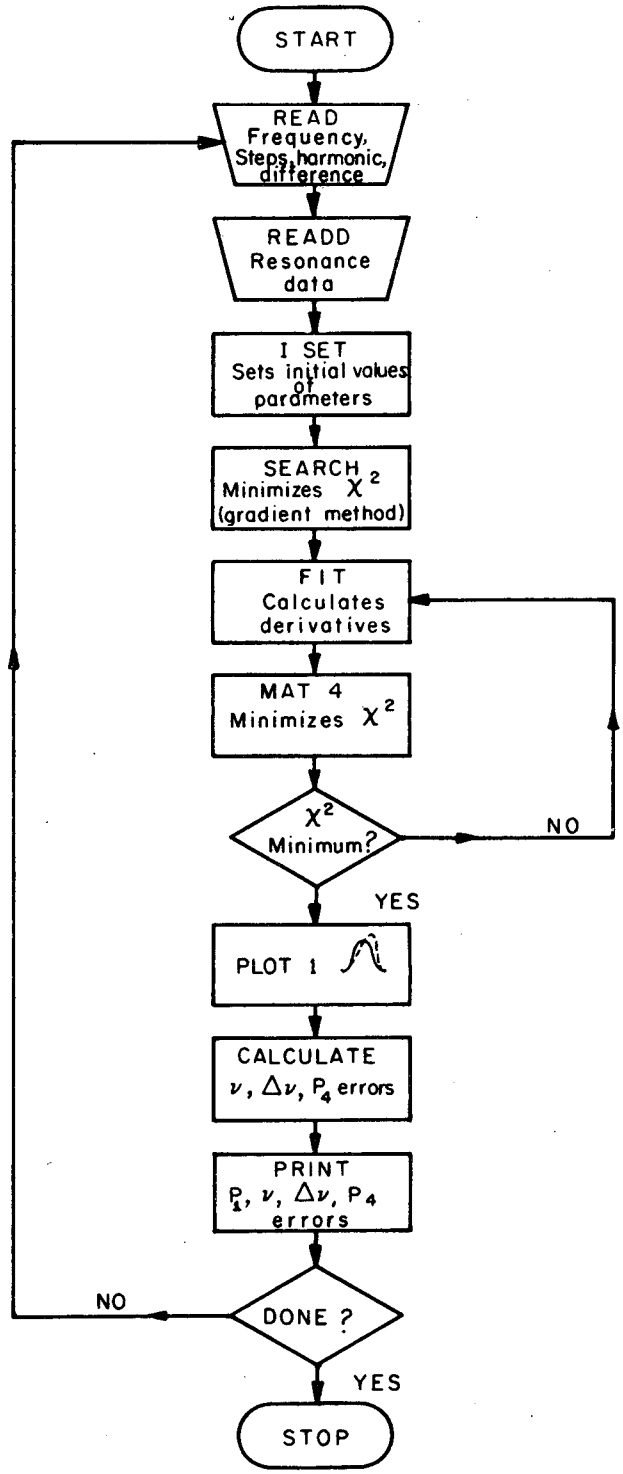

XBL 7410-4388

APPENDIX D

The program AVERAGE calculates the g_J values and their averages.

```
      PROGRAM AVERAGE(INPUT,OUTPUT)
**FORX53
*FANDK2004
*LISTPRINTER
      DIMENSION F(3),FE(3),N1(3),N2(3),N3(3),R(180),ER(180)
    2 DO 5 I=1,3
      F(I)=0.
    5 FE(I)=0.
    1 K=0
   10 F(3)=F(2)
      F(2)=F(1)
      FE(3)=FE(2)
      FE(2)=FE(1)
      N1(3)=N1(2)
      N1(2)=N1(1)
      N2(3)=N2(2)
      N2(2)=N2(1)
      N3(3)=N3(2)
      N3(2)=N3(1)
      READ 11,G1,G2,N4,N5,N6
   11 FORMAT(36X,F10.0,F8.0,18X,3A2)
      IF(N4    -7979)15,20,15
   15 F(1)=G1
      FE(1)=G2
      N1(1)=N4
      N2(1)=N5
      N3(1)=N6
      IF(N1(2)-5667)10,12,10
   12 FAVE=(F(1)+F(3))*.5
      FAE=SQRTF(FE(1)**2+FE(3)**2)
      RATIO=F(2)/FAVE
      RE=RATIO*SQRTF((FAE/FAVE)**2+(FE(2)/F(2))**2)
      GJ=-2.00223735*RATIO
      GJE=2.00223735*RE
      PRINT 50,N1(3),N2(3),N3(3),F(3),FE(3)
   50 FORMAT(1H ,3A2, 5X,F11.4,1H(,F6.4,1H))
      PRINT 51,N1(2),N2(2),N3(2),FAVE,FAE,F(2),FE(2),RATIO,RE,GJ,GJE
   51 FORMAT(1H ,3A2,1X,4HAVE=,  F11.4,1H(,F6.4,1H),1X,F11.4,1H(,F6.4,1H
     1),2X,13HGJ(0)/GJ(HE)=,F11.8,1H(,F10.8,1H),2X,6HGJ(0)=,F11.7,1H(,
     2F9.7,1H))
      PRINT 50,N1(1),N2(1),N3(1),F(1),FE(1)
      PRINT 50
      K=K+1
      R(K)=RATIO
      ER(K)=RE
      GO TO 10
   20 S=0.
      DO 30 I=1,K
   30 S=S+R(I)
      AK=K
      S=S/AK
      T=0.
      Q=0.
      U=0.
      DO 40 I=1,K
      V=1./ER(I)**2
      T=T+R(I)*V
      Q=Q+((R(I)-S)**2)*V
   40 U=U+V
      SIG=T/U
      ESIG=SQRTF(Q/(U*(AK-1.)))
      GJ=-2.00223735*SIG
      GJE=2.00223735*ESIG
      PRINT 54,SIG,ESIG,GJ,GJE
   54 FORMAT(1H ,52X,13HGJ(0)/GJ(HE)=,F11.8,1H(,F10.8,1H),3X,6HGJ(0)=,
     1F10.7,1H(,F9.7,1H))
      GO TO 1
      END
```

REFERENCES

1. M. A. Morren, Ann. Chem. Phys. 4, 293 (1865).
2. A. N. Wright and C. A. Winkler, Active Nitrogen (Academic Press, New York, 1968).
3. S. K. Mitra, Active Nitrogen - A New Theory (Indian Press Ltd., Calcutta, 1945).
4. F. R. Innes and O. Oldenberg, J. Chem. Phys. 37, 2427 (1962).
5. P. Feldman and R. Novick, Bull. Am. Phys. Soc. [2], 10, 455, (1965).
6. C. E. Fairchild and H. P. Garg, C. E. Johnson, Phys. Rev. A 8, 796 (1973).
7. C. E. Moore, Atomic Energy Levels, Vol. 1 (Natl. Bur. Std. Circ. No. 467, 1949).
8. C. C. Kiess and G. Shortley, J. Res. Natl. Bur. Std. 42, 183, (1949).
9. G. O. Brink, J. Chem. Phys. 46, 4531, (1967).
10. i) W. C. Wells and E. C. Zipf, Trans. Am. Geophys. Union 53, 459 (1972).
    ii) C. E. Johnson, Phys. Rev. A 5, 2688 (1972).
    iii) C. A. Nicolaides, Chem. Phys. Lett. 17, 436, (1972).
    iv) R. H. Garstang, Proc. Cambridge Philos. Soc. 57, 115, (1961).

11. L. Dunoyer, Compt. Rend. Acad. Sci. Paris 152, 594 (1911).

12. R. G. J. Fraser, Molecular Beams, (Methuen and Co., Ltd., London, 1937).

13. I. I. Rabi, J. R. Zacharias, S. Millman and P. Kusch, Phys. Rev. 53, 318 (1938).

14. G. Herzberg, Molecular Spectra and Molecular Structure (Prentice-Hall, Inc., New York, 1939).

15. R. N. Dixon, Spectroscopy and Structure (John Wiley, Inc., New York, 1965).

16. A. Lofthus, The Molecular Spectrum of Nitrogen (Spectroscopic Report No. 2, University of Oslo, 1960).

17. G. E. Beale, Jr., and H. P. Broida, J. Chem. Phys. 31, 1030 (1959).

18. A. B. Prag and K. C. Clark, J. Chem. Phys. 38, 2305 (1963).

19. F. R. Innes and O. Oldenberg, J. Chem. Phys. 38, 2306 (1963).

20. H. A. Bethe and E. E. Salpeter, Quantum Mechanics of One- and Two- Electron Atoms (Springer, Berlin, 1957).

21. C. E. Johnson, Phys. Rev. A 7, 872 (1973).

22. S. Dushman, Scientific Foundations of Vacuum Techniques, 2nd Ed., ed. J. M. Lofferty, (Wiley, New York, 1962).

23. W. Gerlach and O. Stern, Ann. Physik, 74, 673 (1924).

24. B. Zak and H. Shugart, Phys. Rev. A 6, 1715 (1972).

25. E. Aygün, B. Zak, and H. Shugart, Phys. Rev. Letters 31, 803 (1973).

26. P. A. Vanden Bout, E. Aygün, V. J. Ehlers, T. İncesu, A. Şaplakoğlu and H. A. Shugart, Phys. Rev. 165, 88, (1968).

27. R. S. Freund, T. A. Miller, D. DeSantis and A. Lurio, J. Chem. Phys. 53, 2290 (1970).

28. R. S. Barton and R. P. Govier, J. Vac. Sci. Technol. 2, 113, (1965).

29. E. U. Condon and G. H. Shortley, The Theory of Atomic Spectra (Cambridge Univ. Press, Cambridge, England, 1957).

30. N. F. Ramsey, Nuclear Moments (John Wiley Inc., New York, 1953).

31. C. Schwartz, Phys. Rev. 97, 380 (1955).

32. G. Racah, Phys. Rev. 62, 438 (1942).

33. P. A. M. Dirac, Proc. Roy. Soc. 117, 610 and 118, 351 (1928).

34. G. Breit, I. I. Rabi, Phys. Rev. 38, 2082 (1931).

35. S. Millman, I. I. Rabi and R. J. Zacharias, Phys. Rev. 53, 384 (1938).

36. N. F. Ramsey, Molecular Beams (Oxford University Press, London 1963).

37. H. Kopfermann, Nuclear Moments (Academic Press Inc, New York, 1958).

38. L. I. Schiff, Quantum Mechanics (McGraw-Hill Inc., New York, 1955).

39. Y. W. Chan, The Nuclear Spins and Magnetic Moments of Ag^{112}, Ag^{113}, Au^{194}, Au^{195}, Au^{196}, and Au^{196m}, Ph. D. Thesis. Lawrence Radiation Laboratory Report 10334 (1962).

40. J. R. Zacharias, Phys. Rev, 61, 270 (1942).

41. P. Kusch and V. W. Hughes, Handbuch der Physik, Vol. XXXVII

42. W. A. Nierenberg, Ann. Rev. Nucl. Science 7, 349 (1957).

43. R. A. Marrus and W. A. Nierenberg, Topics in Radio Frequency Spectroscopy (Academic Press, New York, 1962).

44. E. Condon and O. Sinanoğlu, New Directions in Atomic Physics, (Yale University Press, New Haven, 1972) Vol. II. Experiments, Article 5.

45. B. D. Zak, A Precision Measurement of the g_J Factor of the $^4S_{3/2}$ Ground State of Nitrogen: A Sensitive Universal Molecular-Beam Detector, Ph.D. thesis, Lawrence Berkeley Laboratory, Report 8 (1971).

46. A. T. Bell and K. Kwong, AIChE. J. 18, 990 (1972).

47. H. A. Enge, M. R. Wehr, J. A. Richards, Introduction to Atomic Physics (Addison-Wesley, Inc., Menlo Park, Calif. 1972).

48. H. G. Kuhn, Atomic Spectra (Longmans, London, 1962).

49. W. L. Wiese, M. W. Smith and B. M. Glennon, Atomic Transition Probabilities, Vol. 1 (Natl. Bur. Std. U.S. NSRDS-NBS4, 1966).

50. R. H. Garstang, Proc. Cambridge Phil. Soc. 57, 115 (1961).

51. C. E. Johnson, Phys. Rev. A 5, 2688 (1972).

52. W. C. Wells and E. C. Zipf, Phys. Rev. A 9, 568 (1974).

53. R. S. Freund, J. Chem. Phys. 54, 3125, (1971).

54. E. Aygün, Precision Measurement of the g_J Factor of He^4 in the 2^3S_1 Metastable State, Ph.D. thesis, Lawrence Berkeley Laboratory, Report 2080 (1973).

55. R. S. Van Dyck Jr., C. E. Johnson, and H. A. Shugart, Phys. Rev. Letters 25, 1403 (1970), Phys. Rev. A 3, 908 (1971).

56. G. W. F. Drake, Phys. Rev. A 3, 908 (1971).

57. H. W. Moos and J. R. Woodworth, Phys. Rev. Letters 30, 775 (1973).

58. M. P. Klein and D. E. Phelps, Rev. Scien, Instr. 38, 1545 (1967).

59. W. A. Anderson, Rev. Scien. Instr. 32, 241 (1961).

60. C. L. Hemenway, R. W. Henry, M. Caulton, Physical Electronics (John Wiley Inc., New York, 1962.)

61. P. R. Bevington, Data Reduction and Error Analysis for the Physical Sciences (McGraw-Hill Co., New York, 1969.).

62. H. D. Young, Statistical Treatment of Experimental Data (McGraw-Hill Co., New York, 1962).

63. S. Millman, Phys. Rev. 55, 628 (1939).

64. J. D. Jackson, Classical Electrodynamics (John Wiley and Sons, Inc., New York, 1965).

65. V. Beltrán - López, E. Bleisten, N. Segovia, and E. Ley Koo, Phys. Rev. 177, 432 (1969).

66. H. E. Radford and V. W. Hughes, Phys. Rev. 114, 1274 (1959).

67. R. A. Hegstrom, private communication, 1974.

LEGAL NOTICE

This report was prepared as an account of work sponsored by the United States Government. Neither the United States nor the United States Atomic Energy Commission, nor any of their employees, nor any of their contractors, subcontractors, or their employees, makes any warranty, express or implied, or assumes any legal liability or responsibility for the accuracy, completeness or usefulness of any information, apparatus, product or process disclosed, or represents that its use would not infringe privately owned rights.

TECHNICAL INFORMATION DIVISION
LAWRENCE BERKELEY LABORATORY
UNIVERSITY OF CALIFORNIA
BERKELEY, CALIFORNIA 94720